
# Università degli studi di Padova

Dipartimento di Fisica e Astronomia "Galileo Galilei"

Laboratoire Pierre Agrain, Ecole Normale de Paris

Corso di Laurea Magistrale in Fisica


Tesi di Laurea Magistrale

# Towards Single Spin Manipulation in a cQED architecture


**Relatore:**
Prof. Davide De Salvador
**Supervisore Esterno:**
Prof. Takis Kontos
**Co-Supervisore Esterno:**
Dott. Matthieu Dartialih

**Laureando:** Filippo Vicentini
**Matricola:** 1102616



**Anno Accademico 2015/2016**

*Al Pinco* •

**Abstract**

In this thesis we present a spin based QuBit Architecture that implements single-QuBit gates in the QuBit itself and is predicted to have a long coherence time. This architecture has been physically realized in a Ferromagnetic Double Quantum Dot hosted in a Single Wall Carbon Nanotube, and studied through a coupled Microwave cavity. We present a Linear Response Theory model that ties the transmitted amplitude and phase of the microwave signal through the cavity to the microscopic charge susceptibility of the Double Quantum Dot. We fit those two channels of experimental data to a simple 4 level master equation model that allows us to extract the inter-dot tunneling rate, the charge-photons coupling rate and the charge dephasing rate. We also present a numerical algorithm that allows to evolve in time the quantum state of the device also considering the effect of charge noise. This algorithm is used to study the effect of fast Landau-Zener style pulses on the QuBit, giving the ideal shape of the control pulses.

# Contents

# List of Figures

# Table of Acronyms, Abbreviations and Symbols

| Acronym | Description |
|---|---|
| **DQD** | Double Quantum Dot |
| **CNT** | Carbon Nanotube |
| **SW-CNT** | Single Wall Carbon Nanotube |
| **QD** | Quantum Dot |
| **QuBit** | Quantum Bit |
| **LZ** | Landau Zener Transition |
| **JC** | Jaynes Cummings Hamiltonian (or System) |
| **QND** | Quantum Non Destructive Measurement |
| **QED** | Quantum Electro Dynamics |
| **cQED** | circuit Quantum Electro Dynamics |
| **CQED** | Cavity Quantum Electro Dynamics |
| **EOM** | Equations of Motion |
| **SNR** | Signal to Noise Ratio |
| **DC** | Direct Current |
| **AC** | Alternate Current |
| **RF** | Radio Frequency |
| **MW** | Microwaves. Since we work only with Microwaves, often we refer to Microwaves and Radio Frequencies interchangeably |
| **PCB** | Printed Circuit Board |
| **SEM** | Scanning Electron Microscope |

# Introduction

In 1982 Richard Feynman proposed to exploit the quantum properties of the microscopic world to perform faster and more accurate computations of physical laws [1]. An interesting property of those computers based on the laws of quantum mechanics, called Quantum Computers, is that they enable computations through a new class of algorithms, *quantum algorithms*, essentially different from traditional ones. Depending on the problem, quantum algorithms may perform worse compared to classical algorithms, but they may also perform orders of magnitude better than the classical counterpart.

At first that idea remained primarily of theoretical interest, but it became more and more prominent after Peter Shor discovered a *quantum algorithm* that could factor arbitrarily large numbers in polynomial time. Nevertheless, a lot of experimental and theoretical problems had, and have to be solved before the construction of such a machine can became a reality.

To build such a machine notable issues have to be overcome, and the academic community worldwide started to tackle those in a bottom-up approach.

The problems that the Quantum information community is facing can be very easily explained by observing the foundation upon which we have built traditional calculators: classical computers are built atop the notion of an Universal Touring Machine[1], which is essentially a machine able to perform any possible chain of boolean operations on any kind of boolean data. In 1881 Charles Sanders Peirce [2] showed that to reproduce an Universal Touring Machine (and therefore to perform any boolean operation on any type of boolean data) it is not necessary to work with arbitrarily long strings of bits and with arbitrarily complex gates, as those more complex types can be reproduced starting only from single bits, boolean data of length 1, and with the NAND[2] 2-bit gate. His paper set the roadmap for the very early research: to physically build a calculator of this sort it was needed to engineer a way to reliably read and write single bits and to make those bits *interact* 2 at a time according to the truth table of the NAND gate. Those issues have been solved in the past century with the invention of the transistor, which can be tuned to implement a 2-bit gate or to read/store data.

Evidently the ability of a quantum computer to perform some calculations much faster comes from its ability to exploit some quantum properties of nature, as coher-

[1] A reader with a taste in Complexity Theory will notice that this is not entirely true, as computers are not Touring-Complete because, having a limited memory, they can only be in a finite set of states.

[2] In a later paper, Peirce pointed out that the NAND gate can be swapped for the NOR gate and the result will stay the same.

ence and entanglement. But this ability comes with a price: engineering a device that is able to reliably store a quantum information (QuBit), and perform *quantum logic operations* through gates on this information has been proven to be extremely challenging.

Much in the same way as Peirce showed what should be the elemental building blocks of a classical computers, at the end of the previous century the theoretical quantum information community showed that a Universal[3] Quantum Computer can be built starting from a quantum two level system (the QuBit, often represented as a vector in the Bloch sphere), a 1-QuBit gate and a 2-QuBit gate.

Several architectures have been proposed in the years for the implementation of a QuBit, following the famous paper by Loss and DiVincenzo where they first proposed to use an electron spin embedded in a quantum dot as the element carrying the Quantum Information [3], and nowadays technology has progressed to the point where we can reliably perform write and read operations on QuBits. Unfortunately, implementing gates for a single or 2 QuBits is more challenging than expected, especially if we consider that one day these gates should be scaled up from the 2-3 QuBits toy systems studied today to tens, hundred or thousands QuBits that would make those computers actually useful.

In this thesis I studied the properties of one such implementation of a Spin-based QuBit, which has the desiderable property of implementing one QuBit gates in itself, and would allow easy 2-QuBit gate operations.

During this thesis I worked on characterizing the properties of this QuBit, trying to improve the design and studied it's feasibility. In particular I focused on the spectrum and coherence time of this system. The architecture studied in this thesis, first proposed by Kontos, Cottet [4], consists in embedding the quantum information in two spin eigenstates of a double quantum dot embedded in a carbon nanotube. Since $^{12}C$ graphene has 0-Nuclear Spin, this architecture is expected to have extremely long coherence times. Moreover, this architecture already implements one QuBit gates in the QuBit itself, theoretically allowing simpler designs when scaled up to the numbers needed to build a true quantum processor.

### cQED

Traditionally research on those devices focused on their transport properties in DC and, more recently, at higher frequencies, and our knowledge of their internal structure is the result of complex models fitting the data.

Since the '90s, a plethora of techniques for manipulating and measuring properties of atoms and ions by coupling them with photons has been developed into a framework called Cavity Quantum Electro-Dynamics (CQED), which led physicist to speculate wether it would be possible to couple photons not only to real atoms, but also to "artificial atoms" such as quantum dots. Artificial atoms are very simple condensed-matter systems that have a spectrum similar to that of an atom, and they can be finely controlled by varying voltage and current knobs, but their readout is often a destructive operation, and the internal structure of the system cannot be easily probed[4]. Coupling of a mesoscopic circuit device resembling an artificial atom

[3] But, as with classical computers, not complete

[4] Quantum Non Destructive (QND) measurements had not yet been performed on a solid state

with a Superconducting Coplanar Microwave Cavity was pioneered at Yale in 2004 by Schoelkopf [5]. The interested that followed in this new field, dubbed *circuit QED* was motivated by the relatively small sizes of the resonators (in the order of 1 cm) and the possibility of easily scaling up the size of the system to many artificial atoms.

This new technique enabled physicists worldwide to start probing directly the internal energy structure of those mesoscopic circuits, and has been used extensively in this thesis work.

### Carbon Nanotubes

The host material for the Double Quantum Dot studied in this thesis is a Single Wall Carbon Nanotube (SWCNT). A SWCNT is simply a graphene sheet folded to create a tube. SWCNT are particularly flexible, as they can be tuned to reach all three transport regimes typical of Quantum Dots: Fabry-Perot, Coulomb Blockade and Kondo Regime. Moreover, even if our study was limited to a coupling with ferromagnetic electrodes to inject a spin-polarized current in the device, it is possible to use different type of electrodes to create a wide range of devices; an interesting example beeing a cooper-pair splitter created by using a superconducting electrode [6].

### Summary

The work done as part of this thesis is presented as follows: after that brief introduction to the field of Quantum Information, in chapter 1 we will present the physics of the mesoscopic systems we have worked with during this thesis, focusing in particular on Quantum Dots, Double Quantum Dots, Qubits. In this chapter we also introduce the notion of Charge-Noise, the main source of noise that we find in our experiment. Lastly, we present the QuBit architecture that is the main focus of our work: the Ferromagnetic Spin-Qubit (section 1.5).

In chapter 2 we present the theoretical framework needed to describe the coupling between the Mesoscopic systems presented in the first chapter and the electromagnetic field. In particular, in section 2.3 we present a simple model that was used to fit experimental data presented in chapter 4, concluding the theoretical introduction to the field.

With chapter 3 we give a brief outline of the fabrication steps necessary to produce our samples, the design of the samples and a particular coupling capacitor that was designed as part of this thesis. We also present the Measurement apparatus and the Cryogenic setup.

In chapter 4 we present low-bias transport and cavity measurements performed on two samples, obtaining a good fit to the model previously described. We also present some failed attempts at performing spectroscopy on the system, commenting on why we think we were not able to observe a signature of the processes we were looking for.

Partially uncorrelated from the experimental investigation, chapter 5 presents a numerical study of the dynamics our device exhibits when subject to fast control

device in 2004.

pulses. A numerical algorithm that considers charge noise is considered, and we extracted some informations to asses wether our setup can achieve fast manipulation of the device.

Lastly, chapter 6 concludes the manuscript with a summary of what has been achieved and presenting our perspectives, and in particular, some projects that have already been started to continue on this line of research.

Detailed fabrication steps with precise timing and procedures used are reported in appendix A.

# Chapter 1

# Phenomenology of Quantum Systems

In this chapter we are going to give a brief overview of the various "ingredients" that are used to describe the system of interest in this Thesis: a Double Quantum Dot coupled to Ferromagnetic Leads and a Microwave Cavity. We will begin by giving a general definition of mesoscopic systems (section 1.1), we will then provide a brief overview of Quantum Dots (section 1.2) and later (section 1.3) Iwewill review the main features of interests of Double Quantum Dots (DQD) and explain how those can be used to address a single electronic charge. Lastly, we will build on the previous section to present a novel type of DQD which allows for coherent single spin control, which is the objective of the research presented in this thesis (section 1.5).

## 1.1 Mesoscopic Systems

If we assume that the Macroscopic scale is governed by classical physics and the Microscopic scale is governed by Quantum mechanics, the Mesoscopic scale is the scale defined somewhere between the two, where objects are still macroscopic, as they are formed by more than thousands of atoms, but some quantum properties begin to emerge. Dimensionality plays an important role at this scale, as mesoscopic systems often show different behaviors depending on their dimensions.

An important dimension when treating the transport of electrons in mesoscopic systems is the coherence length $l_\phi$: for sizes $l < l_\phi$ the phase of an electron propagating in the system is well defined, while for $l > l_\phi$ the phase can no longer be defined, and therefore is treated as a random variable.

To start observing effects that cannot be explained by classical physics one can go down to sizes $\mathcal{L}_\mathcal{M}$, smaller than the coherence length $l_\phi$. That way, the system will be coherent and to describe it correctly a wave-function or non diagonal density matrix is needed. An intuitive idea of the scale $\mathcal{L}_\mathcal{M}$ of a mesoscopic device can be given with a simple inequality, where $a_0$ is the Bohr radius, $\lambda_F$ the electronic fermi wavelength and $l_{in}$ the mean free path between inelastic scattering events (also known as the energy relaxation length).

$$a_0 \ll \lambda_F < \mathcal{L}_\mathcal{M} < l_\phi < l_{in} \tag{1.1}$$

There is no rigid definition for *Mesoscopic Systems*, but the devices typically studied sit in the range between 100-1000 nm.

A further classification is made for those samples that are smaller than the elastic scattering mean free path $l_{el}$. Those are samples where electrons can travel without ever experiencing a scattering event, and therefore the resistivity in those devices is a consequence of purely quantum effects.

$$a_0 \ll \lambda_F < \mathcal{L}_{\mathcal{M}} < l_{el} < l_\phi < l_{in} \tag{1.2}$$

Devices of this size are called *ballistic*, referencing to the fact that the motion of electrons in those devices is unperturbed, as the ballistic motion of a projectile.

### 1.1.1 The Conductance Quantum

The first class of experiments performed on Mesoscopic System were transport measurements, which are measurements of the conductance $G \propto \frac{1}{R}$ of a mesoscopic sample. The electrical conductance is a measure of how easy it is for a charge carrier to pass through the structure, and is defined as:

$$G = \frac{\mathrm{d}I}{\mathrm{d}V} \tag{1.3}$$

and measured in $\Omega^{-1}$.

In macroscopic samples the *Drude model*, which ties resistivity to inelastic scatterings, describes quite well the behavior of many solids. The model is clearly not applicable in the ballistic regime, as the mean free path is much bigger than the sample size. In this regime electrons do not experience inelastic scattering while traveling through the sample, but experiments still measure a resistivity: this phenomena is called Quantum Resistance and can be observed in Quantum Point Contacts (QPC). A QPC is a narrow region that connects two electronic reservoirs, and whose section surface can be tuned. In the extreme quantum limit we can imagine that only one electron can transport from one reservoir to the other in an infinitesimal time $\Delta t$, therefore the current flowing through the QPC can be expressed as $\Delta I = {}^{e}/_{\Delta t}$. The potential difference between the two reservoirs can be expressed as $\Delta V = {}^{\Delta E}/_{e}$, where $\Delta E$ is the difference in the chemical potential of the two reservoirs. By combining the two expressions we can write the conductance of the QPC as:

$$G = \frac{\Delta I}{\Delta V} = \frac{{}^{e}/_{\Delta t}}{{}^{\Delta E}/_{e}} = \frac{e^2}{\Delta E \Delta t} \tag{1.4}$$

Recalling the Heisenberg Uncertainty principle $\Delta t \Delta E \geq h$, and considering the minimum entropy state where the as an equality, we obtain:

$$G = \frac{e^2}{h} \tag{1.5}$$

Since our system is spin-degenerate, we should account for two transport channels (one for each spin), and therefore we will obtain:

$$G_Q = \frac{2e^2}{h} \approx 12.9\Omega^{-1} \tag{1.6}$$

This means that in a ballistic conductor, even if there are no inelastic scatterings, we will still measure a resistance due to the quantum nature of the electrons transporting the current. As the Heisenberg principle is an inequality, $G \leq G_Q$ and therefore if the wire has not a 100% chance of transmitting an electron, the conductivity will diminish and the resistance will increase.

This not very formal derivation for the conductance quantum is useful to show the underlying meaning of $G_Q$: a transparent transport channel will have a minimum conductance of $G_Q$, but if it is not transparent, this value will drop. This fact will be used extensively in defining the various regimes at which our devices can be operated.

### 1.1.2 Mesoscopic Carbon Nanotubes

The host material for our experiments will be Carbon Nanotubes (CNT). Carbon Nanotubes are folded sheets of Graphene (an hexagonal lattice of Carbon atoms). A carbon Nanotube can either be Single Walled or Multi Walled. A single walled CNT is analogous to a small pipe, while a MultiWalled CNT is made of multiple concentric CNTs. Single Walled Carbon Nanotubes (SW-CNT), being folded sheets of graphene are quasi-1D Conductors. Fortunately, their diameter is approximately 1 nm, and since the fermi wavelength of an electron in a SWCNT is $\lambda_F \approx 0.76\,nm$ we can assume that they effectively behave like 1D wires with 4 conduction channels, 2 given by the spin and 2 given by the Dirac points of graphene. Quantum effects can be observed by cooling down the samples to $T \approx 10$mK as the coherence length of electrons in a SWCNT is $l_\phi \approx \mu$m. SWCNT can also be tuned to be ballistic conductors, as the mean free path of electron is also on the $\mu$m scale [7].

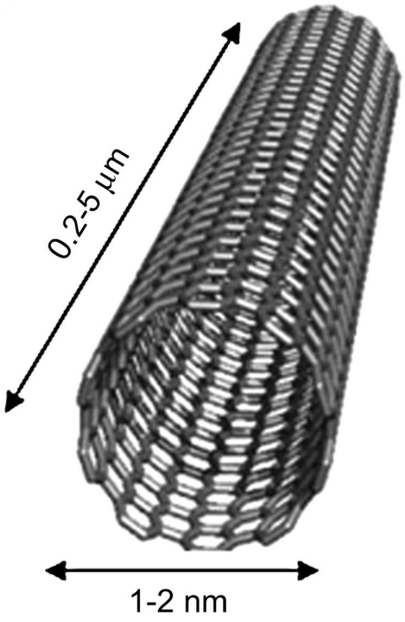


Figure 1.1: Example of a Single-Wall, Carbon Nanotubes with it's characteristic dimensions. (a)

## 1.2 Quantum Dots

Quantum Dots are Mesoscopic devices that tightly confine electrons in a quasi 0 Dimensional structure, giving rise to a *visibly* quantized energy spectrum. A wide variety of physical systems can be engineered to create Quantum Dots, and their realization is not limited to solid state devices but can extend also to photonic systems [8]. The quantum computing community is mainly interested in solid state systems, because of the vast technology and know-how that can be exported with little effort from the semiconductor industry. The vast majority of solid state quantum dots are obtained by confining electrons in a 2D or 1D host material with electrostatic gates:

2D: A 2D Electron Gas (2DEG) is located at the interface of an heterostructure

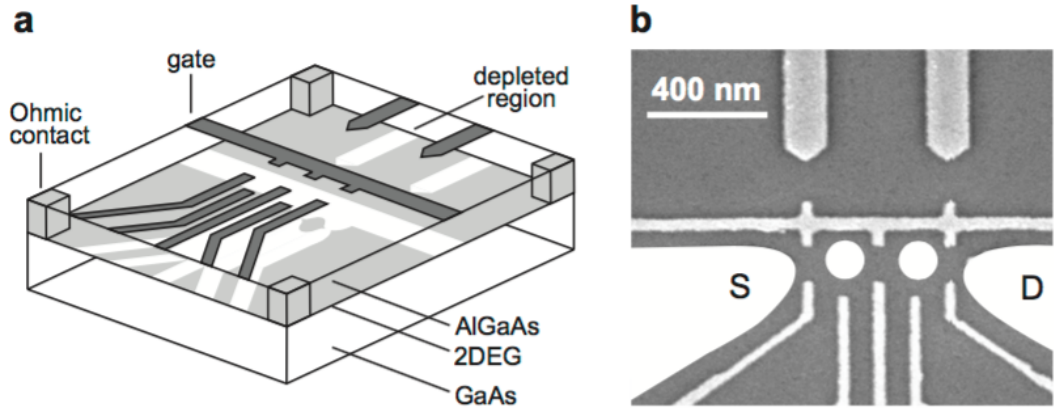


Figure 1.2: Lateral quantum dot device defined by metal surface electrodes. (a) Schematic view of a device. Negative voltages applied to metal gate electrodes (dark gray) lead to depleted regions (white) in the 2DEG (light gray). Ohmic contacts (light gray columns) enable bonding wires (not shown) to make electrical contact to the 2DEG reservoirs. (b) Scanning electron microscope image of an actual device, showing the gate electrodes (light gray) on top of the surface (dark gray). The two white dots indicate two quantum dots, connected via tunable tunnel barriers to a source (S) and drain (D) reservoir, indicated in white. The two upper gates can be used to create two quantum point contacts, in order to detect changes in the number of electrons on the dot

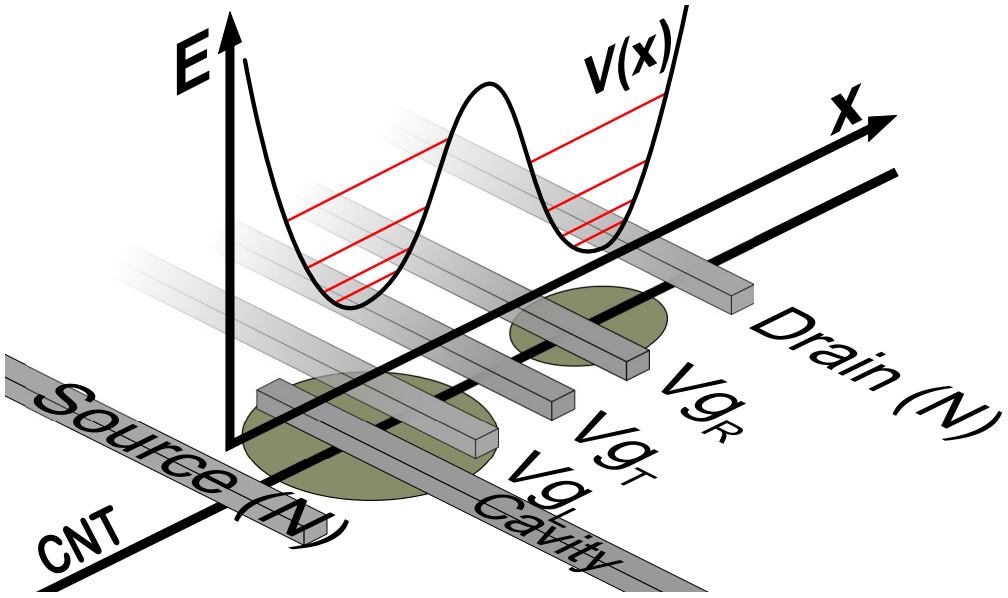


Figure 1.3: Lateral quantum dot device defined by metal surface electrodes deposited on a Carbon Nanotube. Electronic reservoirs are provided by the Source and Drain metallic contact. Between the gates and the nanotube we evaporate a thin layer of Al Oxide to ensure that the coupling is only capacitive. The gates $Vg_L$ and $Vg_R$ set the chemical potential of the L/R dots independently, while $Vg_T$ sets the height of the tunnel barrier between the two dots. The combined potentials of the 3 gates yields the double well potential $V(x)$.

(such as AlGaS/GaAs or ZnO/ZnMgO) (fig. 1.2). Metallic gates are lithografed on top of the Heterostructure. Biasing the gates at a negative voltage will deplete of electrons the area of the 2DEG located under them.

1D: The host structure is a 1D System such as a Nanotube (NT) or Nanowire, which alredy confines the electrons down to 1 Spatial Dimension. Confining along the last dimension is provided by lithographically defined gates evaporated on top, under or in the vicinity of the host structure. An example is provided in fig. 1.3.

The two implementations embody the same physics, but present different challenges and allow probing different ranges in the experimentally-tunable parameters. For example, while fabrication techniques for 2DEG produce very clean samples with few defects that rarely couple to the experimental knobs, the coupling strength between capacitive AC gates and the 2DEG cannot reach high values. On the contrary, CNT devices have a much more complicated fabrication that routinely introduce defects in the structure, but it is possible to achieve a strong coupling with less effort.

For this thesis we focused on CNTs as we were looking to achieve strong coupling with a MW cavity capacitively coupled to the dots.

A desiderable property in a mesoscopic system is the possibility to resolve single electronic levels, which was first achieved through transport measurements. In those experiments a quantum dot is described as a quasi 0-D metallic island coupled through two tunnel junctions to two leads, the source and the drain, that provide the elctronic reservoirs. The chemical potential of the dot can be modified through a potential set by a nearby capacitive gate, which will set the energy of all electronic levels of the dot.

Imagine now to initialize the system so that the island is not coupled to the leads, and then modify the chemical potential of the dot. The number of elementary charge particles (electrons or holes) in the island must be an integer $N$, therefore the charge in the island will be given by $Q = Ne$. Since the dot is metallic, the charge will be concentrated on the surface, producing a field $\mathbf{E}$ which accumulates electrostatic energy. This energy can be expressed as a function of the geometrical capacitance $C$ of the island.

$$E = \frac{Q^2}{2C} = \frac{e^2}{2C}N^2 = E_c N^2 \tag{1.7}$$

If we now allow tunneling, the charge in the dot will change in order to minimize the energy of the whole circuit, and the electrostatic energy stored in the island will vary by the amount $\Delta E = E_c(N_i^2 - N_f^2)$. This energy gives a dominant contribution only when bigger than thermal fluctuations: when $e^2/2C > k_b T$. A second requirement for the number of electrons in the dot to be well defined is for the tunnel barrier to be sufficiently opaque. Sufficiently means that fluctuations $\delta N_e$ in the number of electrons in the dot $N_e$ because of tunneling events are lower than one over the timescale of the measurement (which is roughly $e/\Delta t$, as shown in section 1.1.1). This requirement sets a lower limit for the tunnel resistance $R_t$ of the barrier, $R_t \gg G_Q^{-1}$.

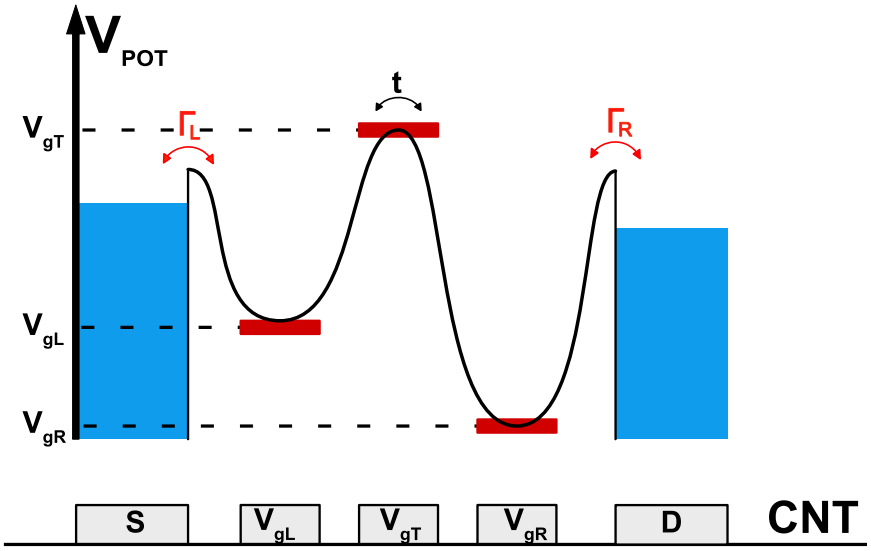


Figure 1.4: Electrostatic potential $V(x)$ induced by the 3 electrodes on top of the nanotube. This is the potential that is felt by the charges in the Double Quantum Dot, and that confines the electrons. $\Gamma_{L/R}$ are the tunneling rates between the L/R dots and the Source/Drain Reservoirs, while $t$ is the tunneling rate between the two dots; those rates are inversely proportional to the height of the tunnel barrier. This potential is the same as the one depicted in fig. 1.3.

---

To summarize, observing effects related to the quantization of the charge in a metallic dot needs two conditions to be satisfied:

$$R_t \gg G_Q^{-1} \tag{1.8}$$

$$\frac{e^2}{2C} \gg k_B T \tag{1.9}$$

The first condition, eq. (1.8), can be achieved by engineering sufficiently weak contacts between the Source/Drain leads and the dot, while the second condition, eq. (1.9), can be achieved by building a system small enough and operating it at low temparature.

## 1.3 Double Quantum Dots

The system of main interest in this thesis is a Double Quantum Dot (DQD) hosted on a SWCNT. A DQD is a device composed of two quantum dots coupled through a tunnel junction. Each quantum dot is also coupled through another tunnel contact to a reservoir (the leads). It is possible to set the chemical potential on each quantum dot through an electrostatic gate, and (up to a certain extent) modify the tunneling rate of the junction between the two dots. A representation of the electrostatic potential induced by the gates on the nanotube is presented in figs. 1.3 and 1.4; the two potential wells correspond to the Left and Right Quantum dots of

the DQD, while the height of the potential barrier between the two dots sets the electron tunneling rate between the two.

### 1.3.1 Energy Scales of the DQD

In the field of circuit Quantum Electro Dynamics (cQED) it is conventional to write formulas by considering $\hbar = 1$, giving energies ($eV$) and rates ($Hz$) the same dimension. This fact will be used extensively in this thesis, and we will often confront energies and rates. When plugging the numbers in the equations we will usually consider everything as energies, multiplying rates by $\hbar$ when needed to give dimensional consistency to the formula.

Our DQD is defined by two leads, the source and the drain, which are weakly coupled to the CNT through tunnel junctions with tunnel rates $\Gamma_{S/D}$[1]. The two dots are separated by a tunnel junctions with tunneling rate $t$ between the L/R dots. Those tunnel rates are in the order of $10 - 100\mu eV$, corresponding to a few $Ghz$ and satisfying the requirement eq. (1.8). If compared to the temperature of our fridge $T = 30mK$ ($\approx 2.6\mu eV$) we verify that eq. (1.9) is respected. Therefore we satisfy physical requirements for resolving single electron levels.

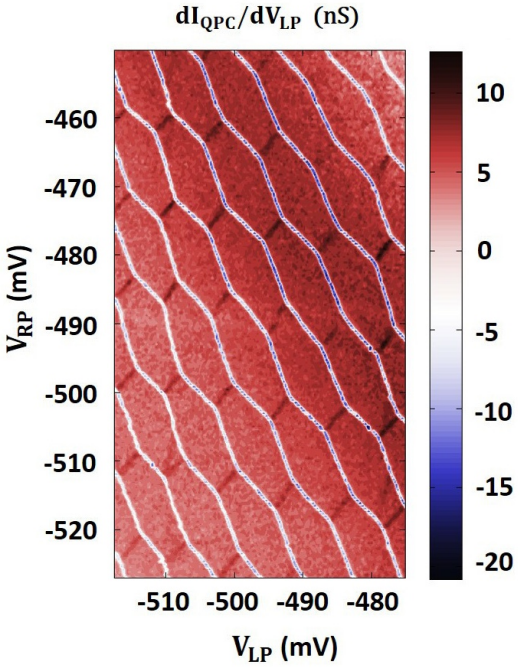


Figure 1.5: Sample measurement showing the stability diagram of a DQD structure, obtained though a differential conductance measurement (a more sophisticated technique than the standard conductance measurement that we described). Note the pattern identical to the one shown in fig. 1.6(b), where $V_{LP}$ and $V_{RP}$ play the role of $V_{gL/R}$. (Source: [9])

Each dot is characterized by a charging energy $U_{L/R}$ which represents the energy needed to overcome the coulomb repulsion when adding an electron to one of the two dots. Charging energy is intrically higher in CNTs compared to 2DEG quantum dots, and is of the order of $10\mu eV$.

### 1.3.2 Measurements on DQDs

There exists a series of measurements that can be performed on a DQD to asses the relative number of electrons present in each dot, and the relative position of energy levels on each dot compared to the fermi energy of the leads [10].

If the device is tuned so that the electronic states on each dot are well defined, which happens when the coulomb repulsion is the dominant energy scale ($k_{BT} <$

[1]The tunneling rate, defined in units of frequency, defines the average number of tunneling events between the lead and the dot per unit of time. In our system they are in the order of the $Ghz$.

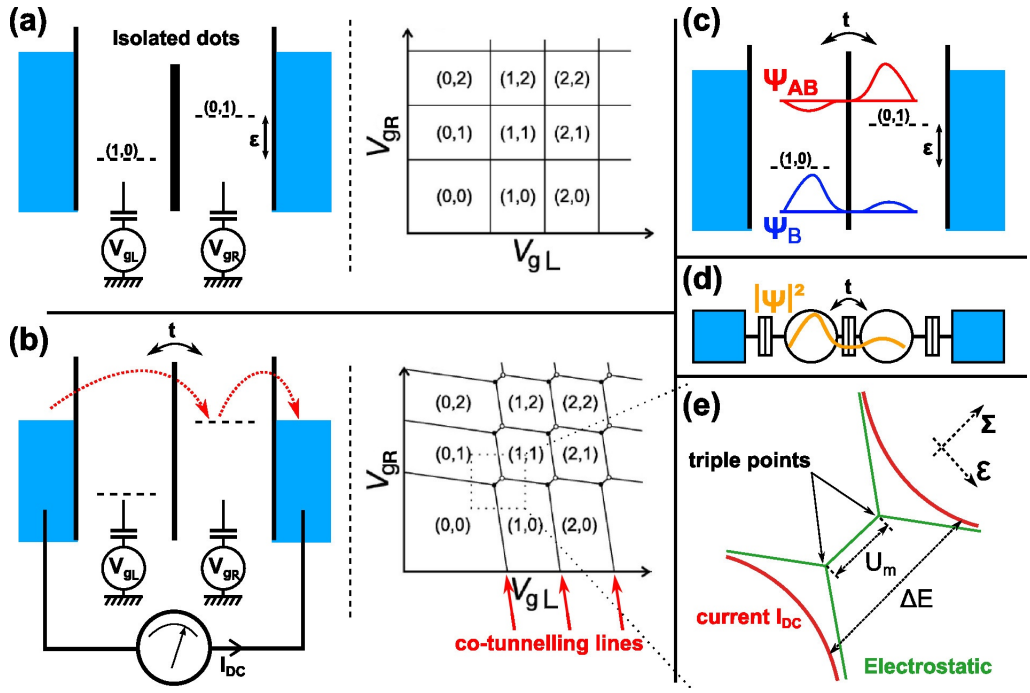


Figure 1.6: Basic transport properties of double quantum dots in the linear regime ($V_{SD} \approx 0$). Tuples ($N$,$M$) indicate that there are $N$ electrons in the left dot and $M$ electrons in the right dot. **(a-left)**: Schematic of a singly occupied double quantum dot (DQD) with one orbital depicted in each dot, tunnel coupled to fermionic leads (light blue). Energy detuning $\epsilon = V_{gL} - V_{gR}$ between the two orbitals is controlled by means of local gate voltages $V_{gL}$ and $V_{gR}$. **(a-right)**: Charge stability stability diagram for 2 isolated dots. Horizontal(Vertical) lines correspond to regions where the R(L) electronic orbital crosses the Fermi level of the electrodes(light blue). **(b)**: Principle of the DC transport spectroscopy. The two dots are electrostatically and tunnel-coupled, resulting in avoided crossings (as detailed in (e)). When the orbital of dot 1(2) is aligned with the Fermi level, current can flow (though this might be through co-tunneling, i.e. $2^{\text{nd}}$ order tunnel event) and this corresponds to the tilted vertical (horizontal) lines on the stability diagram. **(c)**: Close to zero detuning, left and right dots orbitals hybridize and form molecular bonding and anti-bonding states. **(d)**: Simplistic circuit representation of the DQD with the electronic corresponding wave-function. **(e)**: Zoom on the stability diagram close to an avoided level crossing. The two triple points are separated by the electrostatic mutual charging energy $U_m$. Finite tunnel coupling yields a curvature (hyperbola) of the molecular states, thus moving away from the purely electrostatic position of the triple points.

$\Gamma_{S/D} < U_{L/R}$[2]), the device is said to be in the Coulomb Blockade regime.

Referring to fig. 1.6(a-left), the blue continuum indicates the electronic states that populate the fermi gas in the leads, while $Vg_{L/R}$ are the chemical potential for

[2] As said before, we often confront rates ($\Gamma$) usually measured in $GHz$ and energies ($U$) usually measured in $meV$ or $\mu eV$. To confront them we usually multiply by $\hbar$ the rate to convert it to an energy.

the left/right dot. In this regime, with well defined and separated electronic levels, transport will only occur if one or both L/R orbitals are positioned near the fermi levels of the leads (condition depicted in fig. 1.6(b-left)) . If this condition is not respected, as in fig. 1.6(a-left), conductance will be practically zero.

A standard measurement that is performed is to probe the conductance in this regime, which can be extracted by monitoring the current flowing through the device when subject to a small bias voltage ($V_{bias} \simeq 50\,\mu eV$). The simplest case of charge transport happens when the Left and Right orbitals are close in energy and therefore electrons can tunnel between the left and the right dot (See fig. 1.7(a)). In this case transport happens through an electron hopping from $Source \rightarrow L \rightarrow R \rightarrow Drain$. This process, however, can happen only when the Left and Right dot levels are aligned at the same energy and if $t \neq \infty$. When instead only one of the two levels is aligned to the Fermi level of the leads (fig. 1.6(a-left)), Left to Right tunneling is suppressed and transport happens through a second order virtual process called *cotunneling*, that can be represented as $Source \rightarrow L \rightarrow Drain$ or $Source \rightarrow R \rightarrow Drain$.

It is evident that in this situation, at fixed $V_{gR}$, by varying $V_{gL}$ we will see (cotunelling) transport events only when one Left orbital crosses the fermi surface of the Source (and vice-versa). When such a crossing occurs, we can identify the increase/decrease in electrostatic energy of the dot with the increase/decrease of the number of electrons in the dot. The standard notation to indicate a DQD with $N_L$ electrons in the left dot $M_R$ electrons in the right dot with $(N_L, M_R)$. With this notation, when we cross a cotunneling line in $Vg_L$ it means that the number of electrons in the dots dot went from $(N_L, M_R)$ to $(N_L \pm 1, M_R)$. To know the absolute number of electrons one needs to lower $Vg_{L/R}$ enough so that no more electrons can tunnel out of the dots, and we would no longer see "cotunneling lines" where the current is non zero; this is not always possible, and often one can only know the relative number of electrons.

If we disable the tunnel coupling between L/R dots by raising the tunnel barrier to infinity, measuring the current through the device as a function of $V_{gL}$ and $V_{gR}$ yields a plot similar to the one sketched in fig. 1.6(a-right), where white areas resemble areas with no transport, and solid lines indicate lines where conductance is finite due to cotunneling.

If we set $0 < t < \infty$, allowing for electrons to tunnel between the left and the right dot, we will have both electrostatic repulsion $U_m$ between L/R dots and a tunnel coupling. By studying the systems through Linear Response Theory (right panel of fig. 1.6(b)) one can show that the cotunelling lines will tilt, and that a small gap of width $U_m$ will open to account for the repulsion. Since we have allowed interaction between the dots, the transport process $Source \rightarrow L \rightarrow R \rightarrow Drain$ is now available. The dynamics of the cotunelling events and how we related them to an additional electron added to the L/R dots remains unchanged, however, when the L/R orbitals are aligned in energy electrons will be able to tunnel between the two dots, and we can identify this with the tunneling of one electron from the L/R dot to the R/L dot, therefore by crossing this line we will go to a configuration with $(N_L, M_R)$ electrons to a configuration with $(N+1_L, M-1_R)$ or $(N-1_L, M+1_R)$ electrons.

Because of the hybridization between the two atomic orbitals transport events

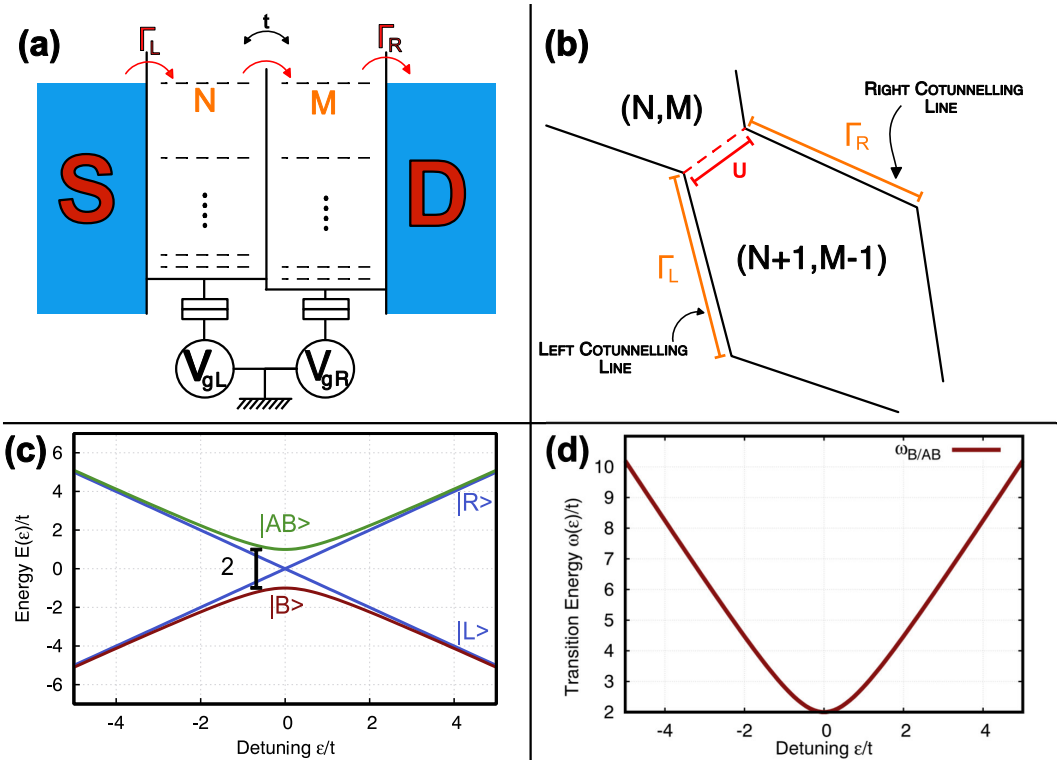


Figure 1.7: Properties of a DQD with two levels in resonance in the linear regime ($V_{SD} \approx 0$). **(a)**: Schematic of the DC transport process that happens for $\epsilon \approx 0$. **(b)**: schematic of the occupation numbers around a L/R transition and a depiction of all allowed processes. The length of the cotunneling lines is proportional to $\Gamma_{L/R}$ and as such an estimation of $\Gamma_{L/R}/\Gamma_{R/L}$ can be easily performed by looking at this plot. **(c)**: Energy as a function of detuning $\epsilon$ for atomic and molecular orbitals of the system approximated as a TLS. Note that at large detuning the molecular orbitals overlap with the atomic orbitals. **(d)**: Transition energy between the Bonding and the Antibonding orbitals, function of detuning $\epsilon$.

will never be due only to a single cotunelling event on the L or R dot, but will be due to a weighted superposition of the two. Measuring the current will not result in straight lines, but in the I-V Curve (panel e of fig. 1.6). If we focus on a single anticrossing, it is possible to define new coordinates $(\epsilon, \Sigma)$ centered in the middle of the gap, where $\epsilon$ naturally corresponds to the detuning of chemical potentials between left and right dots $\epsilon = \mu_L - \mu_R$ and $\Sigma$ is orthogonal to $\epsilon$. In those coordinates the distance between two current lines is:

$$\Delta E = U_m + \sqrt{\epsilon^2 + 4t^2} \tag{1.10}$$

If the inter-dot coupling $t$ is stronger than the coupling to the leads $\Gamma_{S/D}$ and the thermal noise, by fitting this equation to experimental results one can extrapolate $t$ and $U_m$. A note of caution must be given about the precision of those fits: since usually $U_m \gg t$, usually we can in theory achieve a decent precision on $U_m$ if we took data with an high accuracy ($\sigma_{U_m}/U_m \simeq 10\%$), but the error in this estimate of

$t$ will often be around 100%, therefore just giving the order of magnitude, because it just gives a minor contribution to $\Delta E$. To more accurately determine t one is better off using different procedures and fitting functions.

If we now go back to the anticrossing described previously, and consider the coordinates $(\epsilon, \Sigma)$ with origin on one such anticrossing, at low values of $\epsilon/t$ electrons will not be localized in the L/R orbitals, but will reside in the Bonding/Antibonding Molecular Orbitals, the symmetric/antisymmetric superpositions of the two atomic orbitals (fig. 1.7(c)). From now on, I'll often refer to the Bonding/Antibonding orbitals as B/AB.

Moving away from zero detuning, the overlap between the molecular orbitals and the spatial orbitals goes asymptotically in $\epsilon$ to unity , and the structure of the diagram will be mainly dictated by the coupling to the leads $\Gamma_{S/D}$, which can be used to estimate the ratio $R = \Gamma_L/\Gamma_R$ by comparing their lengths (fig. 1.7(b)).

### 1.3.3 Controlling the DQD state

A DQD operated at low bias voltages[3] in the vicinity of the zero-detuning line can be approximated to a two level system, as it's dynamics are dictated mainly by the two atomic orbitals (L/R) at fixed occupation number. The tunnel coupling between the two orbitals give rise to the molecular orbitals (B/AB) which are the orbitals where electrons actually reside. As can be seen from fig. 1.7(c), in the limit of strong detuning ($\epsilon \to \infty$) the molecular and atomic orbitals overlap, and the electron will be strongly localized on one of the two dots. By slowly sweeping $\epsilon$ from $-\infty$ to $\infty$ one transits adiabatically the electron from the left dot to the right, while the electron resides always in the same molecular orbital. If one, instead, makes a fast sweep the transition will not be adiabatical and the electron will be transited from one molecular orbital to the other. This is known as the Landau-Zener transition.

### 1.3.4 DQD as a Charge QuBit

A DQD operated in the vicinity of the zero-detuning line is a two level system, and therefore is a perfect candidate for a QuBit. A QuBit where the information is encoded in the position of an electron takes the name of charge QuBit, and those devices have been well studied for the last 10 years [11]. The principle of a charge QuBit is to encode the 1/0 information in the B/AB orbitals. This can be expressed by representing the system in the bloch sphere, where the two polar points are the B/AB states (fig. 1.8(a)) . The system will precess at a frequency $\Omega(\epsilon) = E_{AB}(\epsilon) - E_B(\epsilon)$ around the z axis (Bloch oscillations), but it is a necessity to treat it in the reference frame of the rotating frame rotating at a frequency $\Omega(\epsilon)$. Unfortunately, $\epsilon$ is set through experimental means, therefore it can be set up to a certain precision, under which it will oscillate around a mean value. Those oscillations in $\epsilon$ (known as charge noise) lead to an unaccountable oscillation in $\Omega$ proportional to $\frac{d\Omega}{d\epsilon}$ and therefore the rotating frame and the real QuBit frame will move more and more out of sync (fig. 1.8(b-c)) . The result is that, gradually, we will be projecting more and more the state vector on the interior of the Bloch sphere, which means that we will be killing off diagonal terms (which are the terms encoding

[3] Also known as the linear regime of the DQD.

the coherence properties of the system). This phenomena, charge noise, is the main responsible for decoherence in charge QuBits, and though it could be theoretically suppressed by operating the QuBit at $\epsilon \approx 0$ (fig. 1.8(d)) it rapidly increases as soon as one varies $\epsilon$, which is necessary for manipulating the QuBit. Although coherence properties of this implementation of a QuBit are poor, it is still used as a basis for more advanced designs, as those reported in the following sections.

## 1.4 Spin QuBit Architectures

As we have seen, a charge based DQD QuBit, even if it enables coherent control of a QuBit is not particularly well suited for this task because of their poor ability to maintain this information in time[4]. One might say that the facility with which one is able to couple the Quantum States is similar to the facility of the environment to couple to the system, destroying it's coherence. As we have said in the introduction, a promising alternative is to encode the QuBit in a Spin degree of freedom; spins are naturally less coupled to the environment and would have much better coherence properties. The first requirement for assessing the viability of such a design, as sketched in the abstract, would be the realization of single QuBit gates, which requires control and readout of a single electronic spin. Unfortunately, the price to pay for the augmented coherence properties of the Spin QuBit is the difficulty of coupling to it's transitions.

Nowadays it is possible to perform single-spin initialization and readout by exploiting a charge-to-spin and spin-to-charge conversion mechanism (such as the Pauli Spin Blockade, very similar to the Coulomb Blockaded transport described in section 1.3.2, but where the effect is sensitive only to the $\uparrow$ or $\downarrow$ spin [12]). The mechanism often employed is based on an auxiliary dot which drains the electronic spin out of the QuBit-system and converts it to a current, effectively destroying it.

One way of performing coherent manipulation of spins (which means applying single QuBit gates) is the use of collinear magnetic field, as those used in NMR experiments. This *Brute Force* approach consists in inducing a Zeeman splitting in the DQD by applying an intense magnetic field, in the range of $0.1T$, with the aid of superconducting magnets. Unfortunately this approach is not compatible with high frequency (Ghz) modulations of the field, with a local control of the field (locally modifying the $B$ field on each QuBit of an array), and with superconducting cavities that allow for reliable non destructive charge sensing. Viable alternatives emerged as the exploitation of intrinsic local properties of the host material, and they have been shown to be more reliable then the intense, real magnetic fields used in NMR experiments. Local properties that lead to an effective spin splitting of the states can be Overhausser fields [13], exchange spin orbit interaction or hybridization to

[4] I want to point out that there exist very good charge-based QuBit setups, such as the Transmon. With Transmons (a set of 2 Josephson Junctions) experimentalists based in California and in Denmark have shown promising coherence properties, that while not outstanding, are more than enough to perform error correction algorithms on a logical QuBit making the state effectively infinitely-long lived. Though it is true that research on those kind of QuBit is at much more advanced stage, as demonstrated recently by IBM with a working universal 5 QuBit computer, there exists major challenges in scaling up this design, which is the reason motivating research in alternative QuBit architectures.

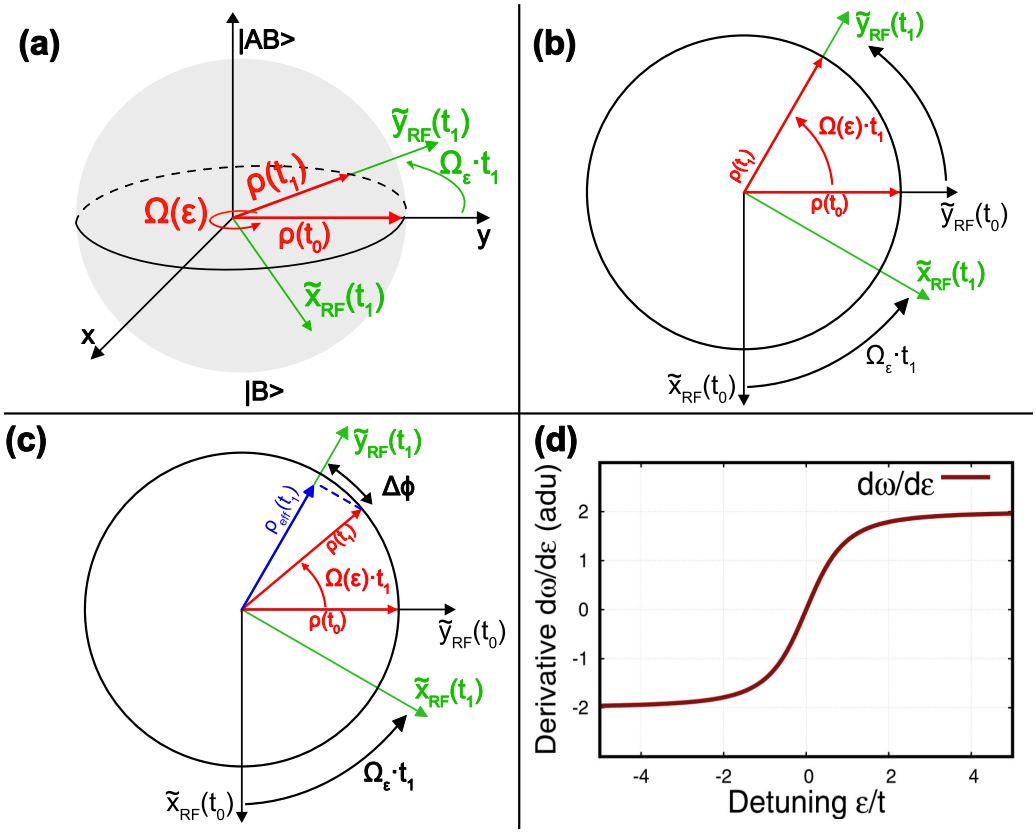


Figure 1.8: Representation of the QuBit state $|\psi\rangle = {}^1/\sqrt{2}(|B\rangle + |AB\rangle)$ and it's evolution in the Rotating Frame. The Bloch sphere is considered with the two polar states $|B\rangle$ and $|AB\rangle$, and the Bloch frequency is $\Omega(\epsilon) = 2\sqrt{t^2 + \epsilon^2}$, as taken from fig. 1.6(c). **(a)**: $\rho = |\psi\rangle$ on the Bloch sphere. It rotates around the z axis at frequency $\Omega(\epsilon)$. The green axis $\tilde{x}_{RF}(t_1)$ and $\tilde{y}_{RF}(t_1)$ are the axis of the frame rotating at constant frequency $\Omega_\epsilon$ after time $t_1$, with initial position equal to the canonical (x,y) axis and final position at time t $\tilde{x}_{RF}(t)$ and $\tilde{y}_{RF}(t)$. If $\epsilon$ is constant in time and can be set with an infinite precision, then the QuBit frequency and the rotating Frame frequency coincide $\Omega(\epsilon) = \Omega_\epsilon$ and $\rho$ is constant in the Rotating Frame. **(b)**: Same situation as **(a)** but showing the cut along the equatorial plane for clarity. $\rho(t_0)$ is the state at the initial time, $\rho(t_1)$ after having evolved for time $t_1$ and pulsation $\Omega(\epsilon)$. Because $\epsilon$ is constant then $\Omega(\epsilon) = \Omega_\epsilon$ and therefore $\rho(t)$ is constant in the rotating frame. When measured the measurement returns $\rho(t_1)$. **(c)**: Same graph as the previous panel, but with $\epsilon$ set with a non-infinite precision. If we do not know $\epsilon$ exactly, the Rotating Frame frequency $\Omega_\epsilon$ will be slightly detuned from the QuBit frequency $\Omega(\epsilon)$. As $\Omega_\epsilon \neq \Omega(\epsilon)$ then $\rho(t)$ is not constant in the reference frame. When we measure we always make the assumption that the ratio of the x and y component of $\rho$ in the rotating frame is constant. Therefore we project the dephased $\rho(t)$ vector on one direction, obtaining the $\rho_{eff}(t)$ (in blue). This vector has the same direction of the initial $\rho$, but it has a lower magnitude, which means that it has decohered. **(d)**: Plot of the derivative of the transition energy. Evidently, charge noise is higher for $\epsilon \to \infty$ and zero only at $\epsilon = 0$.

neighboring spins [14]. A major issue in those experiments is the nuclear spin of the host material: when the host material has a nuclear spin in the lattice that is not zero, the electronic spin can scatter with those, effectively suppressing his increased coherence time. In some of those experiments coherence times of the order of $\tau_2 \approx 10 - 100ns$ have been measured, still lower than the $\mu s$ achieved through charge QuBits. The novel approach predicted to increase the coherence time of a spin QuBit studied in this thesis is presented in the next section.

## 1.5 The Ferromagnetic CNT Spin-QuBit proposal

The main goal of today's research on spin QuBits is coherent manipulation on a spin with a long coherence time. Moreover, we want an implementation that is compatible with circuitQED (a thin superconducting layer used as a waveguide) so that we can perform non destructive measurements on the spin. To lift the spin degeneracy in a DQD we used an effective magnetic field induced by a ferromagnetic lead coupled to the leads (see following section). Not only this does not require intense external magnetic fields, and is therefore compatible with our cQED setup, but it has the added benefit that one can easily engineer the effective field so that it has a different direction in each of the two dots. A position dependent magnetic field, where the positions are represented by the L/R orbitals, is perfectly equivalent to an effective "spin-orbit" coupling, where the orbits are the atomic orbitals of the DQD. Harnessing the spin-orbit coupling would allow direct spin manipulation.

### 1.5.1 Induced magnetic field in CNT Quantum Dots

The key ingredient in this architecture is the effective magnetic field induced inside a QDot by the interface with a ferromagnetic lead (which is very similar to proximity effect in supercodunctors).

In a non interacting picture, one can use the scattering matrix formalism to compute the spectrum of a confined portion of coherent conductor connected to a ferromagnet via a barrier with transmission and reflection probabilities. The spin dependence of the quantized spectrum in the dot can arise from both the transmission probability and the phase of the reflection coefficient. If the transmission probability is spin dependent and non-zero, we can interpret it as an evanescent part of the electronic wavefunction inside the ferromagnet. This can be interpreted as an hybridization of the conduction orbital of the conductor with the first atomic layers of the ferromagnetic lead which naturally provide spin polarization of the total quantum state and that can be referred to as tunneling exchange field. This contribution strongly depends on the amplitude of the transmission probability, which is a

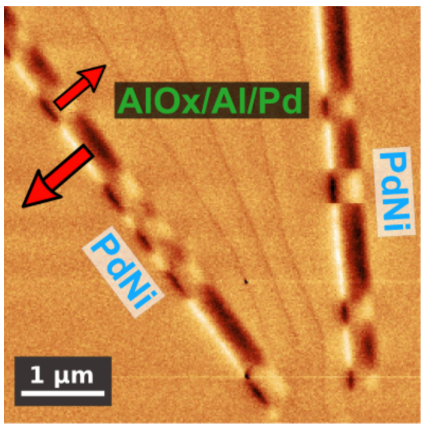


Figure 1.9: Magnetic Force Microscope image of a double quantum dot hosted on a CNT (not visible). The three metallic Al control gates are visible between the two ferromagnetic contact leads, where well defined magnetic domains are clearly visible.

related to the lead coupling rates $\Gamma_{S/D}$, and vanishes for a totally reflecting barrier ( $\Gamma_{S/D} = 0$). It has been observed in quantum dot spin valves and studied as a function of lead coupling lead on a Kondo resonance [15].

However the spectrum of the dot can also be spin polarized from spin dependent phase $\phi_\sigma$ at the reflection. One can thus think of a very opaque barrier with a different shape for spin pointing up and down, as it could happen for a connection to a ferromagnetic insulator for example.

In the non-interacting picture considered here, this confinement-induced exchange field yields an effective Zeeman splitting [4]:

$$2\delta = E_{ex} = \frac{\hbar v_F}{2L}(\phi_\uparrow - \phi_\downarrow) \tag{1.11}$$

where $v_F$ is the Fermi velocity, $L$ is the length of the dot and $\phi_{\uparrow(\downarrow)}$ is a spin-dependent interfacial phase shift. Because the dot spectrum is gate controlled it is in principle possible to tune the exchange field and in particular the tunneling contribution since it is lead dependent.

### 1.5.2 Properties of the ferromagnetic spin QuBit

In the previous section we have sketched the coupling mechanism between the dots and some ferromagnetic lead with a well defined magnetization. An alloy that exhibits well defined magnetization domains are thin layers of $PdNi$. A 30 nm thick, 10 nm wide $PdNi$ layer has well defined magnetic domains with alternating direction that span the whole length of the lead (fig. 1.9) . If we are able to couple our CNT to one of such domains, the discussion of the previous paragraph is valid and we will induce an effective magnetic field in each of the two dots.

To achieve single spin manipulation on this particular DQD, it is needed to build a device with a different magnetic field direction in each of the two dots. This can be achieved by evaporating the 2 ferromagnetic leads with an angle $\theta$ between them. The effective field present in each of the two dots will be defined along a different axis, and therefore in the effective hamiltonian we will have a coupling term between the Spin and the Atomic Orbital (or charge orbital) of the system. Evidently, the two atomic orbitals are tunnel coupled through the tunneling rate $t$. If $t = 0$, the two orbitals are uncoupled and the artificial S-O coupling will be effectively turned off, as the two orbitals won't talk. An effective hamiltonian written in the basis of $\mathcal{H}_{\mathrm{L/R}} \otimes \mathcal{H}_{\uparrow/\downarrow} = \{|\uparrow_L\rangle, |\downarrow_L\rangle, |\uparrow_R\rangle, |\uparrow_R\rangle\} = \{(\uparrow,0), (\downarrow,0), (0,\nearrow), (0,\swarrow)\}$, is [16](additional materials):

$$\mathcal{H}_{\mathrm{eff}} = \begin{pmatrix} -\epsilon/2 - \delta & 0 & t\cos\left(\frac{\theta}{2}\right) & -t\sin\left(\frac{\theta}{2}\right) \\ 0 & -\epsilon/2 + \delta & t\sin\left(\frac{\theta}{2}\right) & t\cos\left(\frac{\theta}{2}\right) \\ t\cos\left(\frac{\theta}{2}\right) & t\sin\left(\frac{\theta}{2}\right) & +\epsilon/2 - \delta & 0 \\ -t\sin\left(\frac{\theta}{2}\right) & t\cos\left(\frac{\theta}{2}\right) & 0 & +\epsilon/2 + \delta \end{pmatrix} \tag{1.12}$$

Where $\delta$ is the magnitude of the induced magnetic field in each of the two dots (for simplicity, assume that the magnitude is the same). The resulting level structure in the DQD is sketched in fig. 1.10 , where one can clearly see the effective Zeeman splitting that arose in each of the two dots.

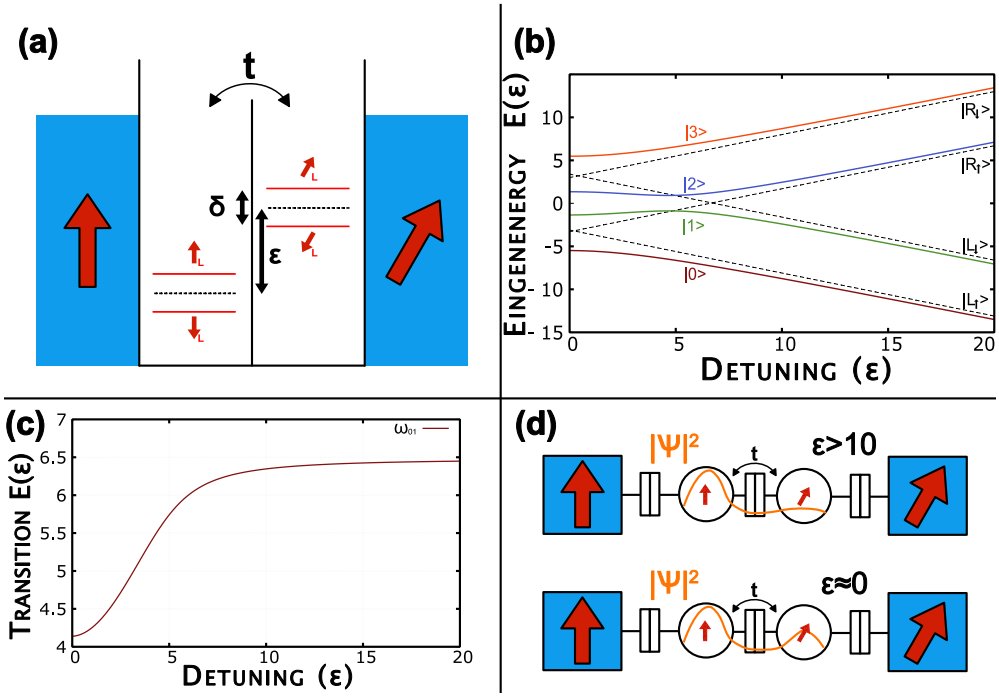


Figure 1.10: **(a)**: Representation of the levels in a ferromagnetic spin-QuBit. Dotted black lines represent the two *atomic* orbitals L/R of the DQD that are Zeeman-split into $\{|\uparrow_L\rangle, |\downarrow_L\rangle, |\nearrow_R\rangle, |\swarrow_R\rangle\}$ (in red) with a gap of $\delta$. $\epsilon$ is the detuning between the two dots.**(b)**: Energy spectrum of the four orbitals of the ferromagnetic spin-QuBit plotted as a function of detuning $\epsilon$. An anticrossing between levels $|1\rangle$ and $|2\rangle$ is visible at $\epsilon \approx 5\ GHz$. **(c)**: Transition energy $\omega_{01}$ between levels $|0\rangle$ and $|1\rangle$, obtained from panel b. Notice that it in the limit of high $\epsilon$ it's almost constant, therefore $\frac{\partial \omega_{01}}{\partial \epsilon} \to 0$ and the system is insensitive to charge noise when operated in this limit. **(d)**: Localization probability of the electron obtained from it's wavefunction. At high $\epsilon$ the electron is strongly confined to the left dot, and therefore does not interact with the induced spin in the right dot, effectively shutting off the effective S-O interaction. For $\epsilon \approx 0$ the system is delocalized between the two dots, resulting in an effective S-O coupling and in a transversal drive on the Bloch sphere, rotating the axis of precession.

---

Diagonalizing numerically this hamiltonian as a function of $\epsilon/\delta$ leads to the spectrum in fig. 1.10. From this spectrum it is evident that, as in the case of a pure charge DQD, the various orbitals hybridize and the system usually lives in a superposition of those, unless one goes at $\epsilon/\delta \gg 1$, where the molecular orbitals overlap with the elements of the basis. In this regime, since the detuning $\epsilon$ is the leading term in the spectrum, the two Zeeman-split duplets have a strong energy gap, resulting in a strongly anharmonic system that is perfectly suited for hosting a QuBit. Moreover, in this limit the transition energy between the two orbitals tends to a constant, therefore the system is not sensitive to charge-noise. This is due to the fact that in the limit $\epsilon/\delta \gg 1$, our state is almost a pure-spin state, as it's spatial charge probability $|\psi(x)|^2$ sits (almost) only on the left dot (panel b in fig. 1.10 ).

By decreasing $\epsilon$, the QuBit states gradually become less pure-spin states, and their charge component increases, as their orbitals overlap more and more with the orbitals of the other dot through the tunnel barrier. In this situation (panel c in fig. 1.10 ) the spatial charge probability $|\psi(x)|^2$ will have a non-negligible component in the Right dot, and this part of the wavefunction will interact with the field in the Right dot, effectively tilting the total field around which the QuBit states precess.

By coupling $\epsilon$ to a small AC field oscillating at the Larmor frequency of the QuBit transition, we will be oscillating the charge components of the QuBit on the two dots, and thanks to the effective S-O coupling, providing the necessary transverse torque necessary to perform coherent manipulations.

To perform measurements on the spin inside the DQD, it is possible to use traditional spin-blockade techniques starting from the left dot, but as this device does not need strong magnetic fields and is therefore compatible with a microwave coplanar waveguide, we expect it would be possible to perform non destructive measurements on the spin through a coupled microwave cavity.

# Chapter 2

# Coupling photons to a mesoscopic circuit

The core of this thesis is the study of a mesoscopic circuit through a coupled microwave cavity, which we will use to perform QND measurements on the circuit. As we have shown in the previous chapter, the mesoscopic device can be approximated to a few-level system, and in this chapter we will present the properties of the coupling between the few-level 'matter' system and the photonic field of the cavity.

## 2.1 Jaynes-Cummings Hamiltonian

To start investigating the rich physics of this category of devices we will start by studying the interaction of a photonic field with the simples possible system: a 2 level system. What we will be describing is a very famous toy model in quantum optics, the Jaynes-Cummings (JC) Hamiltonian [17]. The JC Hamiltonian describes a bath of bosons with energy $\omega_c$ coupled though coupling constant $g$ to a two level system with a transition frequency between the two levels of $\Omega$. The hamiltonian is the following: $H = \omega_c a^\dagger a + \frac{\Omega}{2}\sigma_z + g(\sigma_+ a + \sigma_- a^\dagger)$. This apparently simple hamiltonian describes extraordinarily well many systems, and it has been used extensively in this thesis to understand some phenomenas.

### Minimal Coupling Hamiltonian

In this section we will derive the coupling of a few-level atomic system with a charge $-e$ (an electron) with the electromagnetic field. The analysis starts from the Minimally-coupled hamiltonian obtained through the transformation $\vec{\mathbf{p}} \to \vec{\mathbf{p}} - e\vec{\mathbf{A}}$ where $\vec{\mathbf{A}}$ is the vector potential of the field.

$$\mathcal{H} = \mathcal{H}_{\text{Field}} + \frac{1}{2m}(\vec{p} - e\vec{A}) + eV(x) \tag{2.1}$$

$\mathcal{H}_{\text{Field}}$ is the hamiltonian describing the non interacting Electromagnetic field, V(x) is the electric potential around the particle, which for this treatment we will consider null.

$$\mathcal{H}_{\text{Matter}} = \int \psi^\dagger(\vec{x}) \left[ -\frac{\hbar^2}{2m}\nabla^2 + eV(\vec{x}) \right] \psi(\vec{x}) d\vec{x} \tag{2.2}$$

$$\mathcal{H}_{\text{Int}} = \mathcal{H}_{\text{Int},1} + \mathcal{H}_{\text{Int},2} \tag{2.3}$$

$$\mathcal{H}_{\text{Int},1} = \int \psi^\dagger(\vec{x}) \left[ -\frac{e}{m}\vec{A}\cdot\vec{p} \right] \psi(\vec{x}) d\vec{x} \tag{2.4}$$

$$\mathcal{H}_{\text{Int},2} = \int \psi^\dagger(\vec{x}) \left[ -\frac{e^2}{2m}A^2 \right] \psi(\vec{x}) d\vec{x} \tag{2.5}$$

**Low energy Approximation**

If we assume that we study our systems at low energy, we can assume that only 1-photon processes are allowed and 2-photon processes can be neglected, as they have a much smaller cross-section. This approximation is equivalent to neglecting terms $\mathcal{O}(A^2)$, therefore $\mathcal{H}_{\text{Int},2}$.

In this approximation it is possible to expand $\psi(x)$, the matter field, as a superposition of unperturbed matter wavefunctions $\phi_j(x)$, and the electromagnetic field $\vec{A}(\vec{r})$ in an analogous basis.

$$\psi(x) = \sum_j a_j \phi_j(x) \tag{2.6}$$

$$A^\dagger(\vec{r},t) = \sum_k b_k \vec{u}_k(\vec{r}) e^{-i\omega_k t} \tag{2.7}$$

I want to stress that $\vec{u}_k(\vec{r})$ encodes all the spatial dependence of the electromagnetic field. Substituting those two expansions in the Hamiltonian given above, one obtains the neat, second quantized form:

$$\mathcal{H}_{\text{Matter}} = \sum_j E_j a_j^\dagger a_j \tag{2.8}$$

$$\mathcal{H}_{\text{Int},1} = \hbar \sum_{j,k,\lambda} a_j^\dagger a_k \left( b_\lambda g_{\lambda jk} + g^\star_{\lambda jk} b_\lambda^\dagger \right) \tag{2.9}$$

where

$$E_j = \int d\vec{x} \phi_j^\star(\vec{x}) \left( -\frac{\hbar}{2m}\nabla^2 + eV(\vec{x}) \right) \phi_k(\vec{x}) \tag{2.10}$$

$$g_{\lambda jk} = \int d\vec{x} \phi_j^\star(\vec{x}) \left( u_\lambda(\vec{x}) \cdot \vec{p} \right) \phi_k(\vec{x}) \left( -\frac{e}{m}\sqrt{\frac{1}{2\hbar\omega_\lambda \epsilon_0}} \right) \tag{2.11}$$

where in $g_{\lambda jk}$ we have summed over all possible polarization and field vectors. This is a very complicated shape and it lends itself to an approximation:

### Electric Dipole Approximation

If the spatial behavior of $u_\lambda(\vec{x})$ varies slower than the electronic wave function $\phi_j(\vec{x})$ then we can approximate $u_\lambda(\vec{x}) \approx u_\lambda(\vec{x_0})$. In a physical picture this means that we suppose that the EM field does is constant across the whole mesoscopic circuit. This is justified as the wavelength $\lambda$ of the radiation is $\lambda >> r_e$, much bigger then the electronic radius. In our case we have a $\lambda_{\text{MW}} \approx 40$ mm[1] and $r_e \approx 10^{-9}$m which is the dimension of our nanocircuit. Evidently the electric dipole approximation is valid.

### Plane Wave Approximation

It is also useful to approximate the EM oscillatory behavior to that of Plane Waves, as the assumptions needed to do so are the same that we used above to get the Electric Dipole Approximation.

To do so, we simply get the oscillatory exponential in eq. () and expand the position dependence around $x_0$:

$$e^{i\vec{k}\cdot\vec{x}} = e^{i\vec{k}\cdot(\vec{x_0}+\vec{\delta x})} = e^{i\vec{k}\cdot\vec{x_0}}\left(1 + i\vec{k}\cdot\vec{\delta x} - \frac{|\vec{k}\cdot\vec{\delta x}|^2}{2}\right) = e^{i\vec{k}\cdot\vec{x_0}} + \mathcal{O}(\vec{k}\cdot\vec{\delta x}) \tag{2.12}$$

And neglecting terms of the order $\mathcal{O}(\vec{k}\cdot\vec{\delta x})$ is justified for the same reason explained above. This leads to the expression

$$u_k(\vec{x}) = \frac{1}{\sqrt{V}} e^{i\vec{k}\cdot\vec{x_0}}$$

Substituting this in $g_{\lambda jk}$ we get a much simpler expression for it:

$$g_{\lambda jk} = \frac{e^{i\vec{k}\cdot\vec{x_0}}}{A}\int d\vec{x}\phi_j^\star(\vec{x})\vec{p}\phi_k(\vec{x}) \tag{2.13}$$

Where $A = \sqrt{V}\left(-\frac{e}{m}\sqrt{\frac{1}{2\hbar\omega_\lambda\epsilon_0}}\right)^{-1}$. Recalling that $[\mathcal{H}, \vec{x}] = \vec{p}$ substituting the unpacked commutator into $\phi_j^\star(\vec{x})\vec{p}\phi_k(\vec{x})$, and having $\mathcal{H}$ act on it's eigenstates $\phi_j$ we obtain:

$$g_{\lambda jk} = \frac{e^{i\vec{k}\cdot\vec{x_0}}}{A}\left[E_j - E_k\right]\int d\vec{x}\phi_j^\star(\vec{x})\vec{x}\phi_k(\vec{x}) \tag{2.14}$$

Where every term is real expect for $e^{i\vec{k}\cdot\vec{x_0}}$. But there is always a good choice for the phase of the EM field which will make it real valued, and therefore $g_{\lambda jk} \in \mathcal{R}$.

Concluding, restricting ourself to the very general case of a long wavelength EM wave interacting with a small condensed matter system, we have the hamiltonian:

[1] from 7 Ghz

$$\mathcal{H} = \mathcal{H}_0 + \mathcal{H}_{\text{Int}} \tag{2.15}$$

$$\mathcal{H}_0 = \sum_j E_j a_j^\dagger a_j + \sum_k \hbar\omega_k b_k^\dagger b_k \tag{2.16}$$

$$\mathcal{H}_{\text{I}} = \hbar \sum_{\lambda jk} a_j^\dagger a_k g_{\lambda jk} (b_\lambda + b_\lambda^\dagger) \tag{2.17}$$

This hamiltonian respects the Schroedinger Equation:

$$\mathcal{H}\Phi = i\hbar \frac{d\Phi}{dt} \tag{2.18}$$

And by switching to the interaction picture with the transformation $U = e^{-\frac{i}{\hbar}\mathcal{H}_0 t}$ we can factor out the two non interacting terms:

$$\Phi_I = U^\dagger \Phi \tag{2.19}$$

$$\hat{\mathcal{H}_{\text{I}}}\Phi_I = i\hbar \frac{d\Phi_I}{dt} \tag{2.20}$$

In the Interaction Picture the operators $a_j$, $b_k$ oscillate at the frequency of the mode they represent, therefore they can be written as:

$$\hat{a_j} = a_j e^{-\frac{i}{\hbar}E_j t} \qquad\qquad \hat{b_k} = b_k e^{-i\omega_k t} \tag{2.21}$$

That when substituted into the Interaction Picture hamiltonian they lead to the expression:

$$\hat{\mathcal{H}_{\text{I}}} = \hbar \sum_{\lambda jk} a_j^\dagger a_k e^{\frac{i}{\hbar}(E_j - E_k)t} \left( b_\lambda^\dagger e^{i\omega_\lambda t} + b_\lambda e^{-i\omega_\lambda t} \right) g_{\lambda jk} \tag{2.22}$$

And by defining $\nu_{jk} = E_j - E_k$ we get:

$$\hat{\mathcal{H}_{\text{I}}} = \hbar \sum_{\lambda jk} a_j^\dagger a_k \left( b_\lambda^\dagger e^{i(\omega_\lambda + \nu_{jk})t} + b_\lambda e^{-i(\omega_\lambda - \nu_{jk})t} \right) g_{\lambda jk} \tag{2.23}$$

In a typical experiment for quantum Information we are mainly interested only on the first two levels of the matter system, therefore we are mainly interested in the transition energy $\nu_{01}$. Moreover, we usually want to couple the mesoscopic system with the field, and therefore we put the two in resonance or close to resonance. This means that $\omega_\lambda \approx \nu_{jk}$ for our systems, and therefore $\omega_\lambda - \nu_{jk} \approx 0$, $\omega_j + \nu_{jk} \approx 2\omega_\lambda$. This means that in the Heisenberg picture we will have a quasi-constant term accounting for resonant cavity-circuit processes, such as the adsorption of a photon and the excitation of an electron ( or the opposite ), and a fast oscillating term that can be shown to account for virtual processes (such as the emission of two photons, that later get re-adsorbed). In the case of not too strong external field, then we can neglect those fast oscillating terms: this is called the Rotating Wave Approximation (RWA).

In the RWA with the Dipole approximation, considering only one transition from the ground state to the first excited state $\nu_{01} = \Omega$, and renaming $\lambda = k$ for clarity we get the following result:

$$\hat{\mathcal{H}_{\text{I}}} = \hbar \sum_k a_0^\dagger a_1 b_k^\dagger e^{i(\omega(k) - \Omega)t} g_{k01} + \text{h.c.} \tag{2.24}$$

where $g_{\lambda 01} = -i(2\hbar\epsilon_0\omega_\lambda)^{-1}u_\lambda(\vec{x_0})d_{01}$, and $d_{01} = \langle\phi_0|\, e\vec{x}\,|\phi_1\rangle$, is essentially the dipole moment of the $0 \to 1$ transition.

Since we have restricted ourselves to the case of a 2-level atom, the non interacting part becomes:

$$\mathcal{H}_0 = \sum_{j=\{0,1\}} E_j a_j^\dagger a_j + \sum_k \hbar\omega_k b_k^\dagger b_k$$

### 2.1.1 Spin-operator description

In Quantum Information experiments we are only interested in addressing the transition between the ground state and the first excited state. This is because Quantum Information is built around the QuBit, a quantum version of a Bit, which can be in the two states $|0\rangle$ or $|1\rangle$. The Hilbert space of this system is therefore the same as that of a Spin-$\frac{1}{2}$, which has a very well known operator algebra. It is therefore customary in the field to describe the matter part of our system through some Pseudo-Spin operators $\sigma_+$, $\sigma_-$ and the Pauli Matrices.

In particular, considering once again one makes the identification

$$\begin{aligned} |0\rangle &\to |\downarrow\rangle = |\mathrm{g}\rangle \\ |1\rangle &\to |\uparrow\rangle = |\mathrm{e}\rangle \\ a_1^\dagger a_0 &\to \sigma_+ \\ a_0^\dagger a_1 &\to \sigma_- \end{aligned}$$

From which we can show that $|\uparrow\rangle = \sigma_z\,|\downarrow\rangle$, $\sigma_\pm^2 = 0$.

One can rewrite[2] the atomic part of the hamiltonian as:

$$\mathcal{H}_{0,\text{ Atom}} = \frac{\Omega}{2}\sigma_z \qquad \hat{\mathcal{H}_\mathrm{I}} = \hbar\sum_k \sigma_- b_k^\dagger e^{i(\omega(k)-\Omega)t} g_{k01} + \text{h.c.} \tag{2.25}$$

This description is very handy because one, given the 2x2 density matrix of the system, can immediately compute the probability for the system to be in the excited (ground) state as $p_e = \langle\mathrm{e}|\,\rho\,|\mathrm{e}\rangle = \langle\sigma_+\sigma_-\rangle$ ( and $p_g = \langle\sigma_-\sigma_+\rangle$). Lastly, the atomic coherence, which in a 2-level system is simply the off diagonal term of the (hermitian) density matrix is defined as $\rho_1 2 = \langle\sigma_+\rangle$.

### 2.1.2 Single Mode field: Jaynes Cummings Hamiltonian

In our experiments the coupling between the field and the artificial atom is obtained by placing a resonating cavity near the circuit. Using a cavity with a high Quality factor allows us to couple very precisely only to one transition, if the circuit has more than two states, and therefore makes the previous approximation valid. In the case of high Q cavities describing the field with a continuum of wavevectors $\vec{\mathbf{k}}$ is redundant, as only one mode $\omega_c$ will actually live in the cavity. By considering this further case, we obtain the well known **Jaynes Cummings Hamiltonian**.

$$H = \omega_c a^\dagger a + \frac{\Omega}{2}\sigma_z + g(\sigma_+ a + \sigma_- a^\dagger) \tag{2.26}$$

[2]Shift the energies so that $E_0 = -\frac{\Omega}{2}$ and $E_1 = \frac{\Omega}{2}$, then you can simply use the spin algebra $[\sigma_x, \sigma_y] = \epsilon^{ijk}\sigma_k$ along with the fact that $\sigma_\pm = \sigma_x \pm \sigma_y$ to show the above relation

and in the coupling constant $g$ we have grouped all now-constant factors of the coupling hamiltonian.

This coupling term $g(\sigma_+ a + \sigma_- a^\dagger)$ will be used extensively throughout this thesis.

## 2.2 Input/Output Formalism for a Two Sided Cavity

In this section we will describe the mathematical framework that is used to describe the coupling between the Microwave Resonator and the mesoscopic system, following approximately the same ideas developed in the additional materials of [18]. In the first subsection we will treat an uncoupled resonator to present the quantities that can be theoretically modeled and experimentally measured, then we will add a coupling to the mesoscopic system and lastly we will study it with the aid of the Linear Response Theory.

### 2.2.1 Input Output formalism for an Empty Cavity

In this section we consider a bare cavity coupled through 2 output ports (port 1 for input, port 2 for output) to the transmission lines used for measuring. In principle, one may add another output port to model cavity losses, but those will be neglected for now. The quantities that we wish to obtain are the transmission amplitude and the phase difference of the output signal compared to the input signal. As the mathematical derivations is rather lengthy and technical, in here I report only the most important steps that convey most of the content. For a more in-depth and rigorous derivation one might read [19] or the supplemental material of [20].
The cavity is modeled as a single bosonic mode with energy $\omega_c$ and associated ladder operators $a$, $a^\dagger$ ($\left[a, a^\dagger\right] = 1$). The cavity is coupled through it's ports to two non interacting bosonic baths with operators $\hat{b}_{q,i}$, $\hat{b}^\dagger_{q,i}$, while the coupling is given by the coupling factors $f_{q,i}$ where $q$ labels the momentum of the mode and $i = \{I, O\}$ labels the port. The hamiltonian is therefore:

$$\mathcal{H} = \mathcal{H}_{\text{cav}} + \mathcal{H}_{\text{bath}} + \mathcal{H}_{\text{coup}} \tag{2.27}$$

Where:

$$\mathcal{H}_{\text{cav}} = \hbar\omega_c \left(\hat{a}^\dagger \hat{a} + \frac{1}{2}\right) \tag{2.28}$$

$$\mathcal{H}_{\text{bath}} = \sum_{k,l} \hbar\omega_{k,l} \hat{b}^\dagger_{q,l} \hat{b}_{q,l} \tag{2.29}$$

$$\mathcal{H}_{\text{coup}} = -i \sum_{k,l} \left(f_{k,l} \hat{a}^\dagger \hat{b}_{k,l} + f^\star_{k,l} \hat{a} \hat{b}^\dagger_{k,l}\right) \tag{2.30}$$

Calculations will be performed in the Heisenberg representation, which is related to the Schroedinger representation through the unitary transformation $\hat{O}(t) = e^{i\mathcal{H}t/\hbar} \hat{A} e^{-i\mathcal{H}t/\hbar}$.

Calculating the time evolution $\dot{\hat{O}}(t) = \frac{i}{\hbar}\left[\hat{\mathcal{H}}, \hat{O}(t)\right]$ for operator $\hat{b_{q,i}}$ one obtains the relation

$$\dot{\hat{b}}_{q,i}(t) = i\omega_{q,i} \hat{b}_{q,i} + \frac{1}{\hbar} f_{q,i} \hat{a}(t) \tag{2.31}$$

This relation can be integrated in time between $t_0$ and $t$ giving $\hat{b}_{q,i}(t) = e^{i\omega_{q,i}(t-t_0)}\hat{b}_{q,i}(t) + \frac{f_{q,i}}{\hbar^2}\int_{t_0}^{t} d\tau e^{-\omega_{q,i}(t-\tau)}a(\tau)$ where $t_0 < t$. Knowing that the cavity will mostly contain photons around the cavity frequency $\omega_c$, we can suppose that $f_{q,i} \approx f_i$ and will not depend on $q$ in the small interval around the cavity frequency where it gives a contribution. Defining $\kappa_i = \frac{2\pi}{\hbar}\eta_i|f_i|^2$, computing the evolution for $\hat{a}(t)$ and substituting $\hat{b}_{q,i}(t)$, we obtain:

$$\dot{\hat{a}}(t) = -i\omega_c\hat{a}(t) - \sum_i \frac{\kappa_i}{2}\hat{a}(t) - \sum_i \sqrt{\kappa_i}\hat{b}_{in,i}(t,t_0) \tag{2.32}$$

$$\hat{b}_{out,i}(t,t_1) = \hat{b}_{in,i}(t,t_0) + \sqrt{\kappa_i}\hat{a}(t) \tag{2.33}$$

where $\hat{b}_{in} = \hat{b}_{in}(t_0)$ and $\hat{b}_{out} = \hat{b}_{out}(t_1)$ because we suppose that the input (output) signal does not interact with the system for times before $t_0$ (after $t_1$). In the resulting equations I therefore have $t_0 < t < t_1$:

$$\hat{b}_{in,i}(t,t_0) = \frac{f_i}{\hbar\sqrt{\kappa_i}}\sum_q e^{-i\omega_q(t-t_0)}\hat{b}_q(t_0) \tag{2.34}$$

$$\hat{b}_{out,i}(t,t_1) = \frac{f_i}{\hbar\sqrt{\kappa_i}}\sum_q e^{-i\omega_q(t-t_1)}\hat{b}_q(t_1) \tag{2.35}$$

Interpreting port $i = 1$ as the input port and port $i = 2$ as output port, and supposing thermal fluctuations to be negligible, I fix $\hat{b}_{in,2} \approx \hat{b}_{out,1} \approx 0$. Substituting those into 2.32 and 2.33, going into the Fourier space and carefully expressing the dependency as a function of the input power $\hat{b}_{in,1}(\omega)$, one gets:

$$\hat{a}(\omega) = \frac{\sqrt{\kappa_1}}{i(\omega-\omega_c) - \kappa/2}\hat{b}_{in,1}(\omega) \tag{2.36}$$

$$\hat{b}_{out,2}(\omega) = \frac{\sqrt{\kappa_1\kappa_2}}{i(\omega-\omega_c) - \kappa/2}\hat{b}_{in,1}(\omega) \tag{2.37}$$

where I put $\kappa = \frac{\kappa_1+\kappa_2}{2}$. Assuming a monochromatic input, input power is expressed as $P_{in} = \hbar\omega\left\langle\hat{b}^\dagger_{in,1}\hat{b}_{in,1}\right\rangle$, where the operator can be both in real or Fourier space, due to the monochromaticity. Output power, which in a generic system can span across many frequencies, can be expressed as $P_{out}(\omega) = \hbar\omega\left\langle\hat{b}^\dagger_{out,2}(\omega)\hat{b}_{out,2}(\omega)\right\rangle$.

With these definitions one can predict the cavity transmission at a given frequency as a function of input and output power (which is what can be experimentally measured):

$$T(\omega) = \frac{P_{out}(\omega)}{P_{in}(\omega)} = \frac{\kappa_1\kappa_2}{(\omega-\omega_c)^2 + \kappa^2/4} \tag{2.38}$$

One can also define the Phase of the transmitted signal as:

$$\phi(\omega) = \arg(P_{out}(\omega)) = -\frac{(\omega-\omega_c)}{(\omega-\omega_c)^2 + \kappa/4} \tag{2.39}$$

By plotting those two quantities as a function of frequency (see fig. 2.1) one notices immediately the characteristic lorentzian shape of the transmitted amplitude, and the inversion of the phase at the same frequency $\omega_c$.

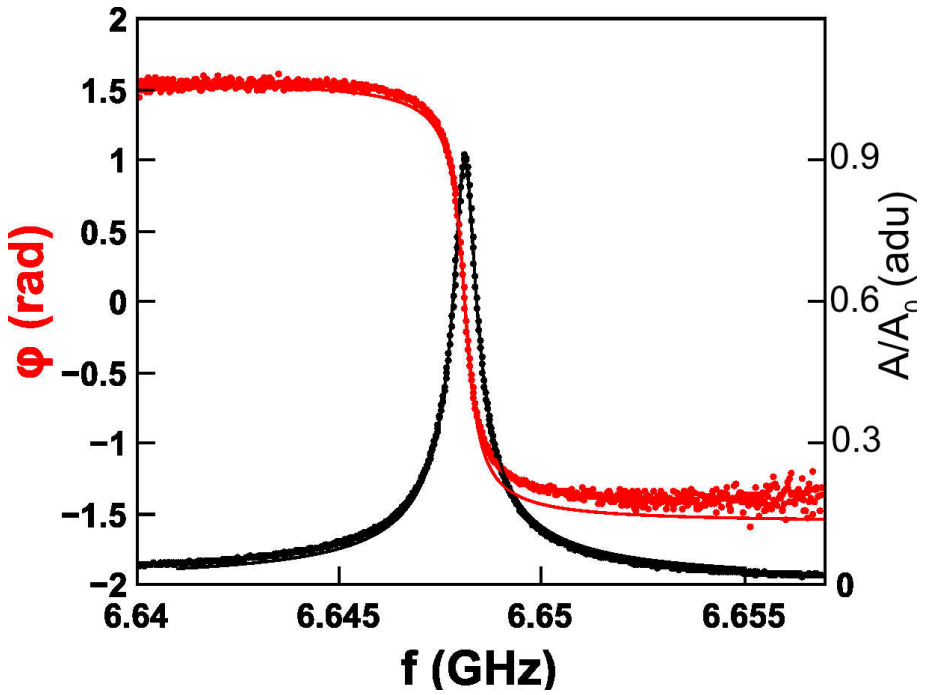


Figure 2.1: Normalized Transmitted Amplitude (black) and phase (red) of an uncoupled (bare) cavity with a resonant frequency centered at $\omega_c \approx 6.677, GHz$ and spread $\kappa$. One notices the lorentzian shape.

---

The last quantity of interest is the number of photons in the cavity. This can be computed by evaluating :

$$n = \left\langle \hat{a}^\dagger \hat{a} \right\rangle = \frac{P_{out}}{\hbar\omega_c \kappa_2} =_{\kappa_1=\kappa_2} \frac{2\sqrt{P_{in}P_{out}}}{\hbar\omega_c \kappa} \tag{2.40}$$

When running experiments it is important to know what is the average number of photons in the cavity because when sufficiently big, it allows us to perform the approximation $\hat{a}^\dagger\hat{a} \approx \hat{a}\hat{a}^\dagger$, known as the semiclassical approximation, that simplifies the treatment of the system.

### 2.2.2 Coupling to the quantum dots

The coupling between the mesoscopic circuit and the cavity can be described using the formalism described in the previous section. In sec. 2.1 we have described how to obtain an effective hamiltonian describing a two level system coupled to a photonic cavity. Exploiting our knowledge of the shape of the interaction term in the J-C Hamiltonian, one may directly rewrite eq. 2.4 with an effective field as:

$$\mathcal{H}_{\text{coup}} = -e \int d\vec{x} \psi^\dagger(\vec{x}) V(\vec{x}) (\hat{a} + \hat{a}^\dagger) \psi(\vec{x}) \tag{2.41}$$

where $\psi^\dagger(\vec{x})\psi(\vec{x})$ describes the electron density and $V(\vec{x})(\hat{a} + \hat{a}^\dagger)$ is the photonic pseudopotential. In the case of the J-C Hamiltonian $V(\vec{x})$ is supposed to be constant

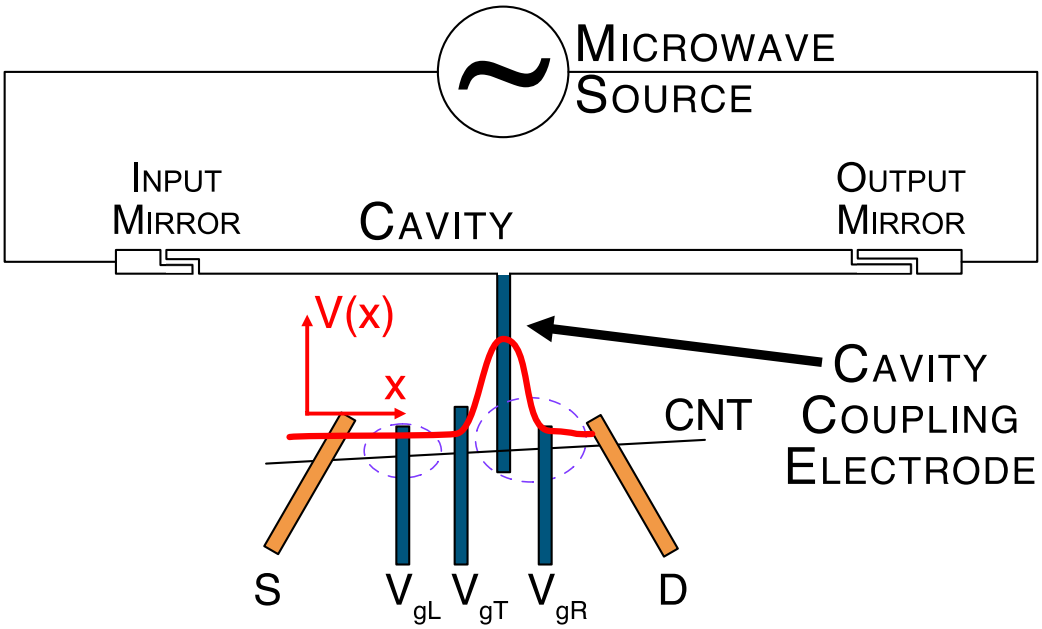


Figure 2.2: Schematic representation of a DQD coupled to a MW resonator. The orange S(ource) and D(rain) electrodes are the two ferromagnetic reservoirs, while the 4 electrodes in blue are Al gates for control ($V_{gl}$, $V_{gR}$, $V_{gT}$) and the coupling electrode. The dashed line represents the approximate areas of the L/R dots. Notice how we expect the photonic pseudopotential $V(x)$ to be confined in a small region by the two electrodes defining the right dot.

in space due to the dipole approximation. As sketched in the first chapter, though, we do not want to couple to a single electron, but to a double quantum dot embedded in a carbon nanotube. As the circuit requires several electrodes (normally set at a constant dc voltage during operation) we expect those to *confine* the photonic pseudopotential in a given region between the two nearest gates [20]. If we place the gates so that the arm used to couple the cavity to the circuit is well centered above one of the two dots, we will have achieved an orbital-dependent coupling to the cavity. A procedure to check experimentally if this kind of coupling is achieved in our device will be outlined after the following subsection.

### 2.2.3 Linear response theory of the driven cavity

In the case of a cavity coupled to a mesoscopic circuit one might start from the same hamiltonian of the bare cavity 2.27 and add two terms, one accounting for the hamiltonian of the circuit $\mathcal{H}_{\text{circ}}$ and one accounting for the coupling between the two $\mathcal{H}_{\text{coup}}$.

Treating the system in Linear Response Theory I suppose the system is weakly driven at frequency $\omega_d$ with intensity $D$, therefore I can factor out from the non interacting bath the drive term $\mathcal{H}_{\text{drive}} = D\hat{a}^\dagger e^{-i\omega_d t} - D^\star e^{i\omega_d t}$, therefore the hamiltonian

becomes:

$$\mathcal{H} = \mathcal{H}_{\text{circ}} + \mathcal{H}_{\text{coup}} + \mathcal{H}_{\text{cav}} + \mathcal{H}_{\text{bath}} + \mathcal{H}_{\text{cav-bath}} + \mathcal{H}_{\text{drive}} \tag{2.42}$$

Assuming that $\mathcal{H}_{\text{circ}}$ commutes with the photonic operators $\hat{a}$, one can derive again the equation of motion for the photonic field which will be analogous to 2.32 with an added term due to $\mathcal{H}_{\text{coup}}$:

$$\dot{\hat{a}}(t) = -i\omega_c \hat{a}(t) - \frac{\kappa}{2}\hat{a}(t) - \sqrt{\kappa_1}\hat{b}_{in,1}(t) - i\sum_i g_i \hat{n}_i \tag{2.43}$$

where $b_{in,1}(t)$ is obtained from 2.34 where in the sum only the single driving mode $\omega_d$ appears, and is therefore an oscillating term. The most important term appearing here is $i\sum_i g_i\hat{n}_i$, as it accounts for the interaction between the field and the mesoscopic circuit. To compute how the photonic field changes under driving because of it's interaction with the circuit, I will first compute linear perturbations of $\hat{n}_i$ in the coupling term $\mathcal{H}_{\text{coup}} \propto \hat{a}$, and then I will substitute it back in 2.43.

The linear response of $\hat{n}_i$ in terms of $\mathcal{H}_{\text{coup}} = \sum_i \hbar g_i \hat{n}_i(\hat{a}(t) + \hat{a}^\dagger(t)) = \sum_i \hbar g_i \hat{n}_i(\langle a\rangle e^{-i\omega_d t} + \langle a\rangle^\star e^{i\omega_d t})$, where I simply performed the substitution $\langle a(t)\rangle \approx \langle a\rangle e^{-i\omega_d t}$, gives:

$$\langle \hat{n}_i(t)\rangle = n_i(t_0) + \sum_j g_j \left(\chi_{i,j}(\omega_d)\langle a\rangle e^{-i\omega_d t} + \chi_{i,j}(-\omega_d)\langle a\rangle^\star e^{i\omega_d t}\right) \tag{2.44}$$

where the response function is defined as:

$$\chi_{i,j}(\omega_d) = -i\langle [n_i(\omega_d), n_j(\omega_d)]\rangle_{\mathcal{H}=\mathcal{H}_{\text{circ}}} \tag{2.45}$$

which gives the perturbation of the occupation of the i-th level as a function of the perturbation of the j-th level. $\chi_{i,j}$ depends only on the microscopic properties of the mesoscopic circuit, and in principle we might assume that we do not know it.

Substituting back eq. 2.44 into the averaged eq. 2.43, keeping only the leading terms in the driving amplitude $D$ and terms oscillating at the driving frequency $\omega_d$ one obtains:

$$\tilde{a}(\omega_d) = \langle a(\omega_d) - a(t_0)\rangle = \frac{\sqrt{\kappa_1}D}{i(\omega_c - \omega_d) + \frac{\kappa}{2} + i\sum_{i,j} g_i g_j \chi_{i,j}(\omega_d)} \tag{2.46}$$

This equation gives us a direct relation between the average value of the ladder operators for the photonic field in the cavity and the mesoscopic response function evaluated on the hamiltonian of the device uncoupled from the cavity. Given that average number of photons in the cavity is given by $n(\omega_d) = \langle \hat{a}^\dagger\hat{a}\rangle(\omega_d)$ (parametrized as a function of the drive frequency) we can use eq.2.46 to estimate the number of photons in the semiclassical approximation, where $n_{sc}(\omega_d) = |\langle a\rangle|^2$. It is immediately evident that the presence of $\chi_{i,j}$ makes it so the circuit influences the number of photons present in the cavity. In a later chapter we will show that the presence of the circuit usually leads to photon emission at a slightly detuned frequency than

the cavity frequency, resulting in a shift of the peak frequency of the (now quasi-)lorentzian peak. This means that at the resonating frequency of the bare cavity $\omega_c$ the photon number $n_0$ will be slightly decreased ($n(\omega_c) < n_0$) but at a certain resonant frequency $\omega_{res}$ the photon number will be increased ($n(\omega_{res}) > n_0$).

As the two quantities that can be directly probed experimentally are the transmitted phase and amplitude, one can compute those two starting from the previous equation by making the assumption that the output field is related to the cavity field linearly through the relation $\hat{b}_{out,2}(\omega) = \sqrt{\kappa_2}a(\omega)$. This is equal to assuming that photonic losses to the environment can be neglected, and that the output mirror defining the cavity has a transmission rate $\propto \kappa_2^{-1}$.

$$T(\omega) = \frac{\sqrt{\kappa_1\kappa_2}}{(\omega_c - \omega_d + \mathcal{I}(\sum_{i,j} g_i g_j \chi_{i,j}(\omega_d)))^2 + \kappa^2/4 + \mathcal{R}(\sum_{i,j} g_i g_j \chi_{i,j}(\omega_d))^2} \tag{2.47}$$

Therefore in the case of a single two orbital system with $g^2 = g_1 g_2$ a measurement of the cavity resonance shift is equivalent to a measurement of the real part of the susceptibility $g^2\mathcal{R}e(\chi)$ and a measurement of the cavity linewidth is proportional to $g^2\mathcal{I}m(\chi)$. In a later section we will show that this means that measurements of the Transmission will provide a direct probe of the imaginary part of $\chi$, while measurements of the Phase will probe the real part.

## 2.3 Master Equation Treatment of the coupling between cavity and circuit electronic transition

The formalism described in the previous section is able to describe the dynamics emerging from any kind of mesoscopic circuit, but this power comes with a cost: computing $\chi_{i,j}$, both analytically or numerically, is an hard task and requires many approximations that often cannot be tested experimentally. Now that we know that the transmitted phase and amplitude encode precisely the properties of $\chi$, we propose to derive those quantities for a simpler 4 level system at the steady state (therefore neglecting net transport of charge from the reservoirs to the system).

In the following section we will briefly present a model first proposed in the additional materials of [21] and [22], which will be used in section 4.1.2 to fit experimental data.

### 2.3.1 Master Equation approach

In this simple model, used to describe the charge degree of freedom of the DQD, we restrict the Hilbert space of the nanocircuit to only four states to make calculations possible and reduce the number of fitting parameters. The four states considered are $\mathcal{H} = \{|\emptyset\rangle, |B\rangle, |AB\rangle, |2\rangle\}$, where $|\emptyset\rangle$ is the empty state (no electrons) and $|2\rangle$ is the doubly occupied (1,1) state. To work in this basis it is convenient to introduce the projectors $\sigma_{AB} = |AB\rangle\langle AB|$, $\sigma_B = |B\rangle\langle B|$, $\sigma_\emptyset = |\emptyset\rangle\langle\emptyset|$ and $\sigma_2 = |2\rangle\langle 2|$. In the spirit of Pauli's sigma matrixes we also define $\sigma_- = |B\rangle\langle AB|$, it's hermitian conjugate $\sigma_+ = \sigma_-^\dagger$ and $\sigma_z = \sigma_{AB} - \sigma_B$. The hamiltonian can be rewritten in this basis as the following.

$$\mathcal{H} = \omega_c a^\dagger a + \frac{\omega}{2}\sigma_z + E_0\sigma_\emptyset + E2\sigma_2 + g\left(\sigma_- a^\dagger + \sigma_+ a\right) + \epsilon_{in}\left(e^{-i\omega_d t}a^\dagger + e^{i\omega_d t}a\right) + \mathcal{H}_{Bath} + \mathcal{H}_{Bath}^{Coupling} \quad (2.48)$$

In this equation $\omega_d$ refers to the frequency of the microwave drive on the cavity, while $\epsilon_{in}$ refers to it's amplitude. The Hamiltonian $\mathcal{H}_{Bath}$ describes the degrees of freedom of the source bath for the cavity and the fermionic baths for the 2 leads connected to the DQD, while $\mathcal{H}_{Bath}^{Coupling}$ describes the coupling between the system and the Baths. Together, those two terms are responsible for the decoherence processes in the system.

Because of the high quality factor of our cavity, decoherence processes in the system are dominated by the electronic decoherence due to electrons jumping in and out of the leads, and therefore we will restrict the bath-coupling term to the only two decoherence processes $\sigma_\pm$.

$$\mathcal{H}_{Bath}^{Coupling} = \sum_{q,\ i=\{L/R\}} \gamma_i\left(\sigma_+ b_{q,i} + \sigma_- b_{q,i}^\dagger\right) \quad (2.49)$$

In addition, we also consider a dephasing term $\Gamma_\phi$ on $\sigma_z$ arising for example from low frequency charge noise acting on the detuning $\epsilon$. We can then change the frame of reference by moving into the frame rotating with the driving field at a frequency $\omega_d$ by using the rotation operator $\hat{U}(t) = e^{-i\omega_d \hat{a}t}$[3], and then write the equations of motions in the rotated frame, obtaining the following:

$$\frac{d}{dt}\langle a\rangle = -(\kappa/2 + i\Delta_{cd})\langle a\rangle - i\epsilon_i n - ig\langle a\rangle \quad (2.50)$$

$$\frac{d}{dt}\langle \sigma_-\rangle = -(\gamma/2 + \Gamma_\phi + i\Delta_{cd})\langle \sigma_-\rangle + ig\langle a(\sigma_{AB} - \sigma_B)\rangle \quad (2.51)$$

$$\frac{d}{dt}\langle \sigma_{AB}\rangle = -ig(\langle a\sigma_+\rangle) - \left\langle a^\dagger\sigma_-\right\rangle) + \sum_j(\Gamma_{j\to AB}\langle\sigma_j\rangle - \Gamma_{j\leftarrow AB}\langle\sigma AB\rangle) \quad (2.52)$$

$$\frac{d}{dt}\langle \sigma_B\rangle = ig(\langle a\sigma_+\rangle) - \left\langle a^\dagger\sigma_-\right\rangle) + \sum_j(\Gamma_{j\to B}\langle\sigma_j\rangle - \Gamma_{j\leftarrow B}\langle\sigma B\rangle) \quad (2.53)$$

$$\frac{d}{dt}\langle \sigma_j\rangle = \sum_{i\neq j}(\Gamma_{i\to j}\langle\sigma_i\rangle - \Gamma_{i\leftarrow j}\langle\sigma_j\rangle) \quad (2.54)$$

In the above we have defined the QuBit-drive detuning $\Delta = \Omega - \omega_d$ and the cavity-drive detuning $\Delta_{cd} = \omega_c - \omega_d$; $\kappa$ is taken as in the previous section to be the total cavity loss factor, and $\Gamma_{j\leftrightarrows A}$ is the transition rate from level $|A\rangle$ to the reservoir j or viceversa.

[3]Note that for a time-dependent transformation such as $\hat{U}(t) = e^{-i\hat{A}t}$, the hamiltonian transforms as$\mathcal{H} \to \tilde{\mathcal{H}} = \hat{U}^\dagger\mathcal{H}\hat{U} - \hat{A}$.

As said before, we are only considering the left and right electronic baths, therefore $j = \{L,\ R\}$, and we determine the transition rates through Fermi Golden Rule[4]:

$$\Gamma_{j\leftarrow A} = \Gamma^{L}_{j\leftarrow A} + \Gamma^{R}_{j\leftarrow A} \tag{2.55}$$

$$\Gamma^{r=\{L,\ R\}}_{j\leftarrow A} = 2\pi|\gamma_r|^2 \nu_r f_r(E_j - E_A) \tag{2.56}$$

where $\nu_{r=\{L/R\}}$ is the density of states in reservoir L/R and $f_r(E_j - E_A)$ is it's Fermi function taken at the energy difference between the states $|j\rangle$ and $a$.

To obtain a closed system of equations we make use of the semiclassical approximation for the cavity which is valid in the limit of $n_{ph} \gg 1 \rightarrow$ we can treat the cavity field as classical. This is justified because most of our measurements are performed with $n_{ph} > 10$. The semiclassical approximation allows us to simplify the following: $\langle a(\sigma_{AB} - \sigma_B)\rangle \approx \langle a\rangle \langle \sigma_{AB} - \sigma_B\rangle$ and $\langle a\sigma_+\rangle \approx \langle a\rangle \langle \sigma_+\rangle$.

By looking for a solution to the system of equations 2.50-54 in the stationary regime ($\frac{d}{dt}\langle A\rangle = 0$) we obtain:

$$\langle \sigma_-\rangle = \frac{\chi}{g}\langle a\rangle \langle \sigma_z\rangle \tag{2.57}$$

$$\langle a\rangle = \frac{-i\epsilon_{in}}{i\Delta_{cd} + \kappa/2 + i\chi\langle \sigma_z\rangle} \tag{2.58}$$

Where the charge susceptibility $\chi$ for the DQD in this approximation is:

$$\chi = \frac{(g_o \sin\theta)^2}{-i(\gamma/2 + \Gamma_\phi) + \Delta} = \frac{g^2}{-i\Gamma_2 + \Delta} \tag{2.59}$$

where $\Gamma_2 = \gamma/2 + \Gamma_\phi$ is the inverse of the $\tau_2^\star$ of the charge QuBit, which is the coherence time of the quantum state. In the case of resonant driving ($\Delta_{cd} = 0$) we can obtain an useful formula relating the cavity field $\langle a\rangle$ to the variation in the resonating frequency valid for small shifts:

$$\Delta f_c = \mathcal{R}e\,(\chi)\,\langle \sigma_z\rangle \tag{2.60}$$

### 2.3.2 Linear Regime Approximation

To further reduce the number of parameters needed to fit our theory, we consider the particular case of $eV_{SD} < k_B T \ll \Omega$ (where $eV_{SD}$ is the average strength pushing electrons from the source to the drain). In this regime, known as the linear regime, the voltage difference between the source and the drain is smaller than the electronic thermal energy and therefore we can neglect it. In this case the electrons do not have a sufficient energy to jump from the ground state, the Bonding orbital, to the Antibonding orbital (as $k_B T\Omega$) and therefore we can consider $\langle \sigma_z\rangle = \langle \sigma_{AB} - \sigma_B\rangle \approx -1$ (A more formal proof is given in chapter 4 of [19]).

With this approximation we can simplify further eq. 2.60 obtaining a function with only 3 parameters.

[4] the $\hbar$ is not reported in the formula because, as said at the beginning of the chapter, we are working with $\hbar = 1$

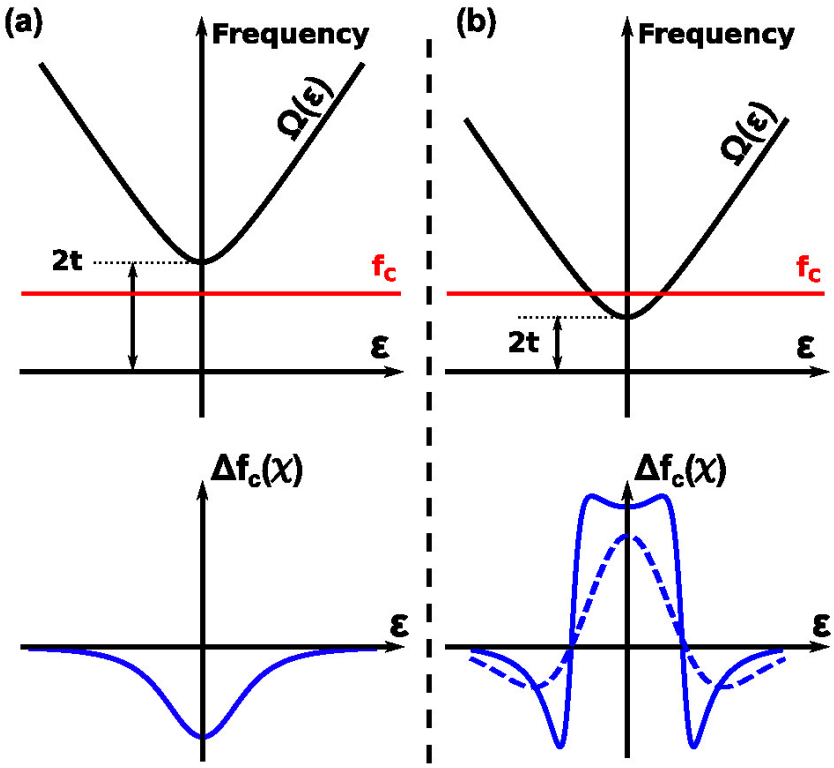


Figure 2.3: Dispersion relation $\Omega(\epsilon)$ and resonance displacement $\Delta f_c \propto \chi$ of a DQD charge QuBit read through a coupled cavity in the linear regime. **(a)** Non resonant case where the QuBit frequency is always detuned from the cavity frequency $(2t + \Gamma_2 > f_c)$ **(b)** near resonant case with $2t < f_c$. Cavity and QuBit lines cross. The susceptibility changes sign with the detuning $\Delta$ and qualitatively depends on whether there is strong decoherence (dashed line) or weaker (full line).

---

$$\Delta f_c = -\mathcal{R}e\,(\chi) = -g^2 \frac{\Delta}{\Delta^2 + \Gamma_2^2} \tag{2.61}$$

Using the definition given in section 2.1 for $\Omega$, we obtain the expression for the QuBit detuning $\Delta = \sqrt{\epsilon^2 + 4t^2} - \omega_c$. While $\omega_c$ is defined during the design of the sample, $\epsilon$ can be fully controlled through electrostatic gates. In theory, also $t$ can be controlled through the gates, but as will be shown in chap. 4 the control that we achieved on this parameter is poor. Nevertheless, controlling $\epsilon$ is sufficient to obtain a formula that should describe our experimental data, and allow us to extract quantities such as the coupling strength g and the charge QuBit coherence time $\Gamma_2^{-1}$.

In fig. 2.3(a) we present a plot of $\Delta f_c(\epsilon)$. In panel **(a)** the non resonant case with $2t - \Gamma_2 > \omega_c$ is presented. In this case the cavity and the QuBit do not affect the qualitative behavior of each other, and we only see a decrease of the resonance frequency when we approach the QuBit frequency as we expected from the qualitative discussion presented in sec. 2.2.3 . In panel **(b)** we present the

case where the QuBit frequency $\Omega$ crosses the cavity frequency $\omega_c$. In this case the detuning $\Delta = \sqrt{\epsilon^2 + 4t^2} - \omega_c$ changes sign, as does $\Delta f_c$. In the region where $\Delta \approx 0$ the shape of $\chi$ depends strongly on the coupling strength $g$ between the cavity and the QuBit. In our simple model we assume this is constant (though we know this is not correct).

Lastly, since the quantities that we are able to measure experimentally are variations in the transmitted amplitude $\frac{\Delta A}{A}$ and variations in the transmitted phase $\Delta\varphi$ through the cavity, we relate eq. 2.61 to those two quantities through eq. 2.47, obtaining the following relations:

$$T_{cav} = \frac{\sqrt{\kappa_1\kappa_2}}{i\Delta_{cd} + \kappa/2 + i\chi} \tag{2.62}$$

$$\Delta\varphi = -\arg(T_{cav}) \tag{2.63}$$

$$\frac{\Delta A}{A} = \frac{|T_{cav}|}{|T_{cav}(g_0 = 0)|} - 1 \tag{2.64}$$

$$\tag{2.65}$$

Where the formula used for $\chi$ will be eq. 2.59.

$$\chi = \frac{g^2}{-i\Gamma_2 + \Delta} \tag{2.59}$$

Therefore for fitting experimental data obtained from the cavity ($\Delta\varphi$ or $^{\Delta A}/_{A}$) we will have the following free parameters:

$\kappa_i$ with $i = 1, 2$, representing the opacity of the input and output mirrors/capacitors defining the cavity. $\kappa = \kappa_1 + \kappa_2$ is the total value. We will estimate $\kappa$ by looking at a bare, uncoupled cavity, and the ratio of $\kappa_1$ and $\kappa_2$ is set by the design, and it is the ratio in the length of the two capacitors.

$\Delta_{c,d}$ detuning between the cavity and the driving field. Since we will be performing resonant measurements, this will be 0.

$g$ coupling strength between the cavity and the mesoscopic device. This will be a free parameter in the fit.

$\Gamma_2$ $= \tau_2^{-1}$ is the inverse of the coherence time of the charge degree of freedom. This will also be a free parameter in the fit.

$\Delta$ $= \sqrt{\epsilon^2 + t^2}$, by keeping t fixed becomes essentially proportional to the detuning from the L/R degeneracy line. We give a rough estimate of $t$ by looking at the curvature of current lines, therefore $\Delta$ becomes a function of $\epsilon$, the horizontal coordinate in our fit.

# Chapter 3

# Experimental setup

One of the interesting aspects of the experiments in circuit-QED is the possibility-necessity of working with devices designed and manufactured in-house. Careful initial design of our devices is not sufficient to achieve our ambitious goal of controlling a single spin in a carbon nanotube. The philosophy in the field is that of feeding back the knowledge gained from issues encountered both during fabrication and measurement to fabrication itself, leading to a continuous evolution of the design, the recipes and therefore the resulting samples that is the only mean of achieving the final goal.

In this chapter I first wish to present the main challenges encountered during fabrication and how those constraint our ability to measure effectively. In the second section I will present the setup used for measurements.

## 3.1 Nanofabrication & device design

Our device design is essentially that of a DQD defined through 3 gates and 2 ferromagnetic contacts on a SW CNT. The fabrication of those devices is challenging due to the lack of precise control over many crucial steps of the process, in particular those involving CNTs.

All of the nanofabrication work was done in the clean room of the ENS.

Details of the many steps required to produce our samples are extensively reported in appendix A, and here I will only focus on two issues: the fabrication of high quality factor cavity and the steps involving CNTs.

### 3.1.1 Fabricating high Quality factor MW cavities

To transport the Microwave signal of the transmission line, and to define the resonating cavity on top of our Silicium chip we used a Coplanar Waveguide (CPW). A CPW (fig. 3.1) is a type of electrical transmission line which can be fabricated with conventional semiconductor manufacturing technology, as they consist of a single conducting track laid on top of a dielectric substrate (for example $SiO_2$) together with the ground (or return) conductors positioned at both sides of the transmission line. The ground conductors are separated from the central track by a small gap, which has an unvarying width along the length of the line. CPWs are very well known because of their central role in todays technology, and there exist several

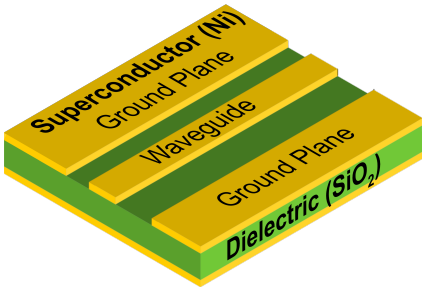


Figure 3.1: Representation of a Coplanar Waveguide (CPW). The green part is the Dielectric providing the insulation and mechanical support for the CPW.

commercial solution that allows one to compute the ideal gap as a function of the materials employed and the wavelength of the signal.

To define a cavity along a CPW it is simply needed to introduce two imperfect *mirrors*, implemented as capacitors, at the edges of the area that will define the cavity (fig. 3.2).

As the quality factor of a CPW is decreased by resistive losses in the conductor and in the dielectric, to achieve the highest possible Q factor our design employs $Nb$ for the ground and the transmission lines. $Nb$ is superconducting at low temperatures, reducing to zero all the losses that happen inside the lines and leading to very high quality factors. In theory Q could be improved by swapping the dielectric substrate for some low loss material as Sapphire, but those material complicate fabrication and requires depositing a layer of Al before each lithography, which could damage our nanotubes.

The substrates used were therefore undoped high resistivity (10k$\Omega$.cm) Si/SiO2 substrates, with 500nm oxide. Such substrates combined with fabrication techniques derived from aluminium resonators, yield high quality factor cavities with $Q \approx 10^6$ at large microwave powers, far higher than what was needed for our purposes.

### 3.1.2 Fabrication

In this section we will briefly report over the main fabrication steps; precise instructions are reported in Appendix A. Fabrication of our devices is done by using a variety of techniques, such as Optical Lithography for large-scale patterns ($l > 10\mu m$), Electron Beam Lithography for fine patterns, deep ion etching and metal evaporation. We start our fabrication from a $SiO_2$ chip where we evaporate a uniform layer of 250 nm of $Ni$. After evaporation we lithograph a negative resist mask on top of the chip by means of optical lithography[1] and then we perform deep ion etching on the masked chip, yielding all the patterns visible in fig. 3.2(a). Note that an approximately square $100 \times 100$ $\mu m$ area is etched during this step, leaving the $SiO_2$ exposed to allow the following fabrication steps; this area is visible in fig. 3.2(b), where the patterns present in the central area are obtained a following fabrication step. After etching we deposit a Carbon Nanotube in this area, following the procedure described in sec. 3.1.3. The nanotube is then contacted by first

[1] We use a Chromium Optical mask that we manufactured with electron beam lithography and chemical etching.

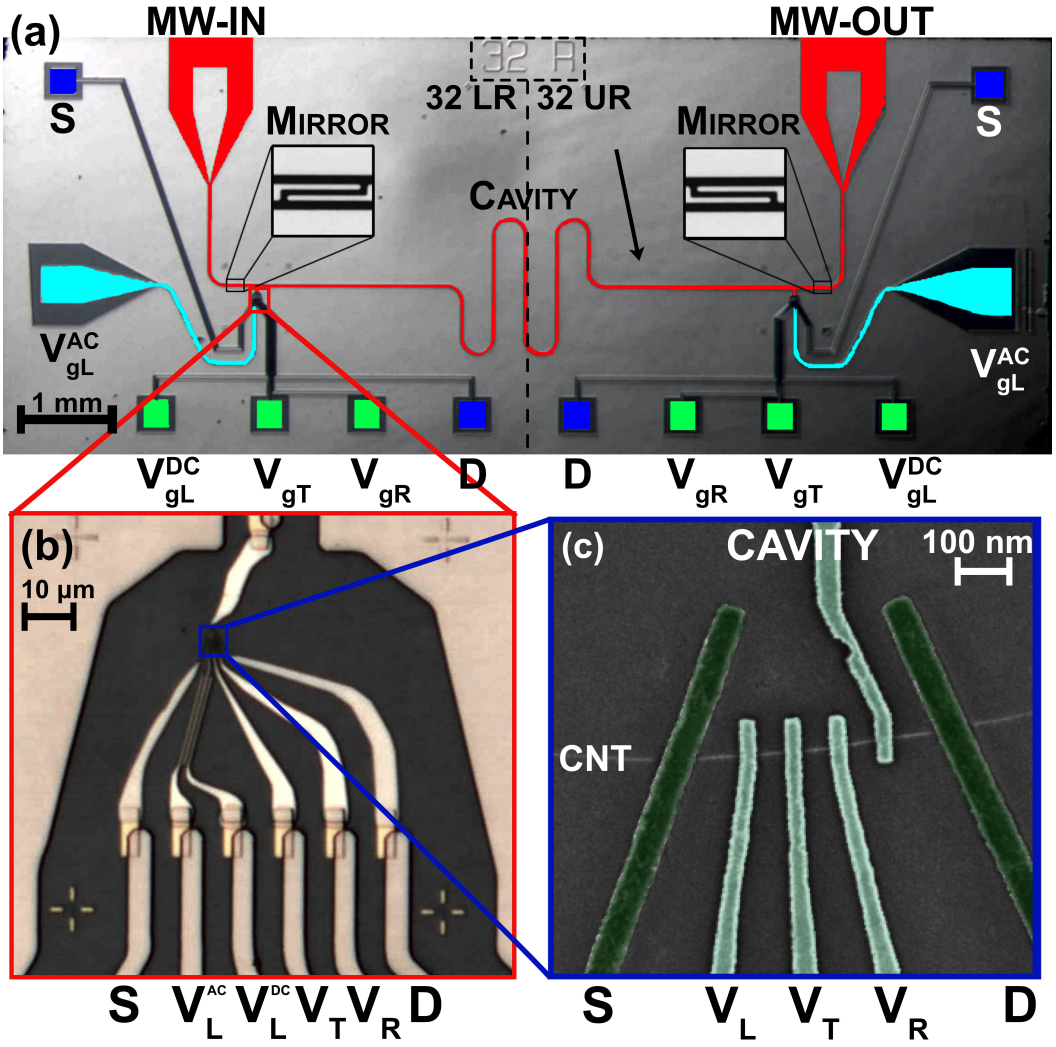


Figure 3.2: Optical photo of device SQBRESUT-32 at the end of the fabrication. The U-shaped Coplanar Waveguide (Colored Red) in the center is the cavity; the particular of the two capacitors/mirrors defining the cavity are zoomed in. The circuit is symmetric because on each chip we fabricate 2 independent DQDs, coupled to the same cavity. The two devices are labelled (SQBRESUT-)32LR and 32UR, which stands for Lower and Upper Right. This is because during fabrication we work on square chips with 2 Cavities (L/R) with 2 coupled DQDs each. They can be controlled independently. Next to the capacitors, in the small area where all the lines converge is located the area where the nanotubes will be stamped and the DQD will be fabricated. Bonding Pads are highlighted in Blue (Source and Drain), light blue ($V_{gL/R/T}$ and). The two separate lines for $V_{gL}$, namely $V_{gL}^{AC}$ and $V_{gL}^{DC}$ allow to mix (see fig.3.3) the two components of the control signal. In **(b)** the contacting between the patterns lithographed in different steps is visible; notice the gold rectangles (pre-contacts) used to contact the different stages. **(c)** shows the fine structures making up the DQD on top of the CNT. The dark highlight shows the ferromagnetic leads which are contacted with the CNT, while the lighter highlight shows the Al electrodes that are only capacitively coupled.

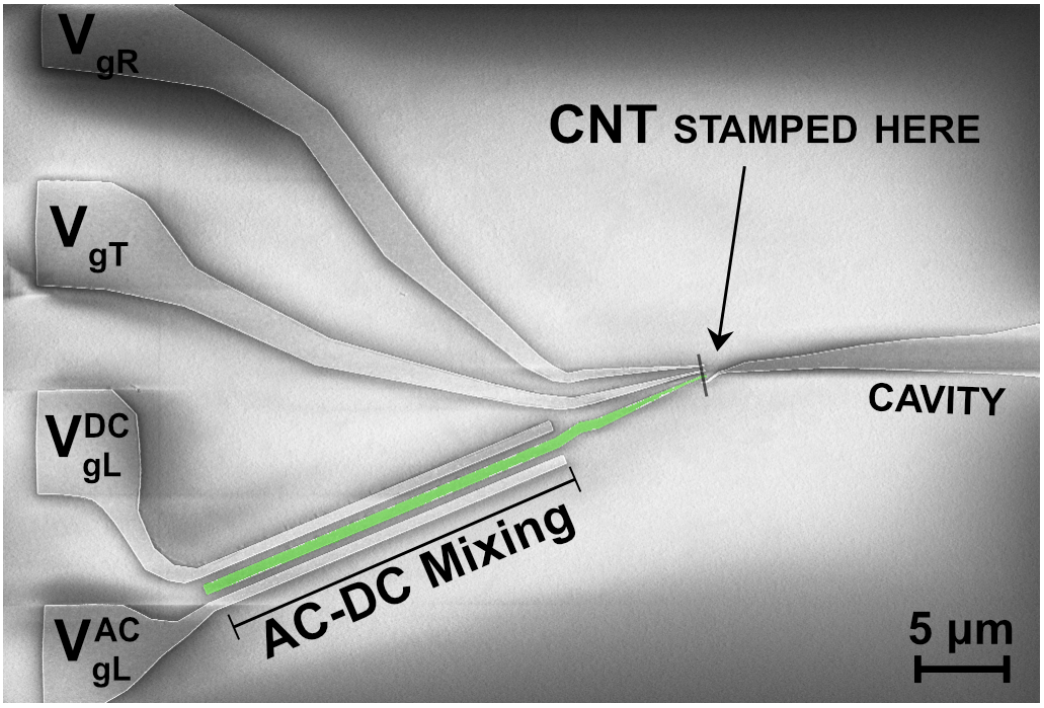


Figure 3.3: Electron Beam micrograph of a Fine Al lithography test. In the lower part of the picture the double capacitor used to mix $V_{gL}^{DC}$ and $V_{gL}^{AC}$ is visible. The central conductor (highlighted in green) is capacitively coupled to the CNT itself, and effectively acts as $V_{gL}$ while the other two are connected to the DC/AC generators in the laboratory. The position of the CNT is reported, but it's dimensions are not in scale. Note that this micrograph shows the same 4 central connectors of fig. 3.2(b), just with a slightly different geometry and rotated clockwise by $90^o$.

evaporating two ferromagnetic $PdNi$ electrodes (see sec. 1.5.1)for the Source (S) and Drain (D), shown as dark blue electrodes in fig. 3.2(c). To evaporate the patterns that we need we use electron-beam lithography to pattern the nanometric-precision resist mask prior to evaporation. The last step consists in evaporating, using the same technique, 4 aluminum control electrodes (highlighted in light blue) on top of a thin oxide layer to prevent direct galvanic contact between the electrodes and the CNT.

A new feature of the design that we fabricate, absent from previous iterations, is an AC-DC mixing capacitor on $V_{gL}$. As we ultimately envisaged the ability to perform $ns$ short pulses on the DQD, we need the ability to control both components (DC and AC) of the various gates in real time; as this is not trivial, in this test design (SQBRESUT-32) we only tried to achieve it on one of the electrostatic gates. The Mixing is done on chip, as close as possible to the DQD, as the Microwave and the DC lines are thermalized differently along the fridge, and therefore are transmitted using very different techniques. The mixing stage itself (see fig. 3.3) is composed of a double capacitor: a central conductor, capacitively coupled to the CNT is itself capacitively coupled to the AC and DC conductors that are placed in parallel to it. The length of the arms is calculated so that the DC capacitance between the two

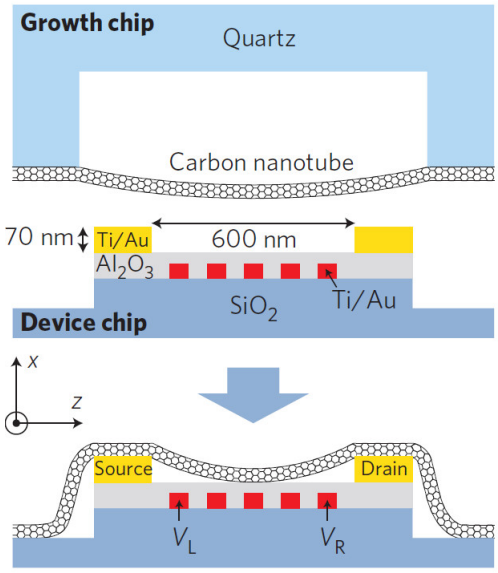


Figure 3.4: Principle of the pristine CNT stamping technique. (Source: [23])

arms and the central conductors is at least 20 times greater than any other parasitic capacitance in the system. Since a capacitor behaves differently for DC and AC, a calibration will be needed to know how strongly the AC component is coupled to the DQD compared to the DC.

### 3.1.3 Carbon Nanotubes

One major source of disturbances when performing measurements on a CNT device are defects present in the CNT. It is not uncommon for the cavity to couple to some internal transition of defects present in the structure of the CNT. Those transitions are extremely unpleasant, as they usually have a very broad line-width, are difficult to model and therefore very easily hide the signals that we are looking for. This is especially true when we try to perform spectroscopy on the system and shine very intense RF pulses on the system.

Those defects can be both structural in nature, such as displacement in the position of C atom in the lattice caused by mechanical strain, or caused by some residue of resist sticking to the CNT surface. For those reasons growing directionally a CNT exactly over the contacts and gates that will define the DQD would solve the majority of those problems. Unfortunately this is not possible, as the growth process of CNTs requires temperatures in the range of $900^o$ which are incompatible with the majority superconductors: Al, for example, has a melting point of $660^o$, while Nb, which has an higher melting point, will degrade it's superconducting property when baked as some of it's defect towards the surface experience a phase transition. Moreover, the catalyst used during growth, $Fe$ nanoparticles, are a dissipative medium and when they are located near a cavity they easily disrupt it's quality factor.

It is therefore evident that superconducting cavities are not compatible with

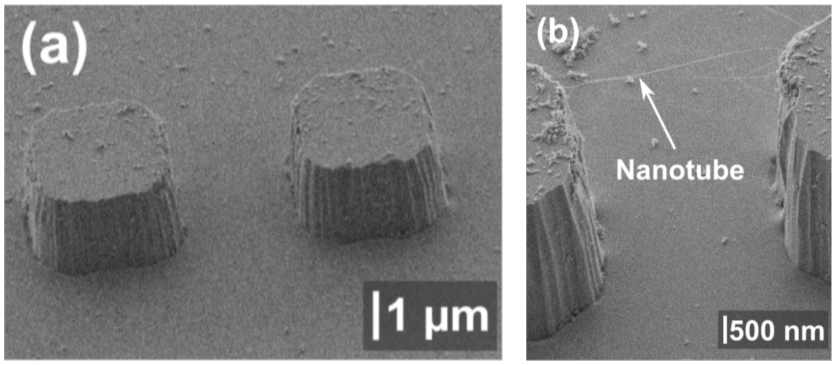


Figure 3.5: Electronic Microscope images of **(a)** a Quartz Chip etched through a RIE process to obtain two nanopillars approximately 1 $\mu m$ high. **(b)** same Quartz chip after CNT growth. A CNT suspended between the two pillars is clearly labelled.

CVD growth of CNTs, and that the two steps must be separated. The solution thought to solve most of the problems would be that of growing a suspended CNT between two nanopillars several $\mu$m high, align the nanopillars with the edges of the contacts on our $SiO_2$ chip and then apply some pressure to transfer the nanotube from one substrate to the other. If well performed, there should be very few induced defects in the region of the CNT used to define the Quantum Dots, and the CNT would not be exposed to any chemistry.

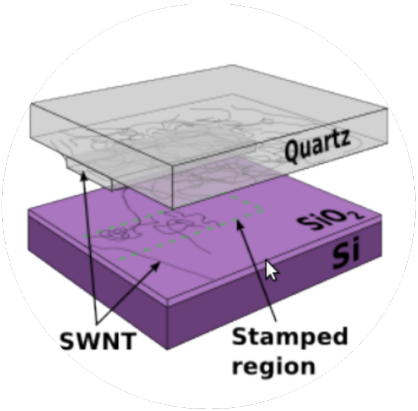


Figure 3.6: Representation of the stamping process. The quartz chip has some nanotubes grown on top of the nanopillars. By pressing the quartz on top of the $SiO_2$ chip some nanotubes are transferred to the $SiO_2$ substrate. (Image taken from [24])

Unfortunately this technique would require a high degree of control over the growth of the CNTs that we do not posses yet, and the $\mu$m level precision in the positioning requires dedicate equipment not available in our lab (at the moment only one group has achieved this nontrivial feat, very briefly reported in the additional materials of [23] in order to keep an edge over the competition).

A compromise between the number of fabrication steps to which the CNT was to be exposed, and our available technology has been found by growing CNTs semi-directionally on two nanopillars etched on a quartz substrate, stamp them on a dedicated area of $SiO_2$ near a previously-fabricated resonator (fig. 3.6) , and later evaporate contacts and gates.

One of the problems that we face is related to the growth: we do not have a control on the exact number of nanotubes grown between two nanopillars, and since stamping more than once on a cavity is not advisable as it adds quartz dust to the sample (which lowers the Q factor), we tend to grown a high number of nanotubes on the pillars. Moreover, those nanotubes are not really suspended

between the two pillars, but instead they are attached on one side to a nanotube and floating on the other side. This is still compatible with our process, even if it is not ideal.

The stamping procedure that we follow was first suggested in [24]. We start by gluing the quartz substrates to a bigger 5cm x 10 cm glass mask. For gluing we use super-adhesive double sided scotch tape that we try to attach to the glass without leaving any air bubble between the two. After the quartz is secured to the glass mask we position the glass mask on the optical mask holder of an Optical Lithography machine, and the $SiO_2$ sample on the sample holder of the same machine. Alignment of the nanopillars above the stamping area is done manually[2] with a precision in the order of 10 $\mu m$, though it is not vital. After alignment we manually lower the quartz and apply pressure through a micrometric screw. Since the machine was not designed for that purpose, we have no way to reliably know when contact between the nanopillars and the $SiO_2$ is achieved, and later how much pressure we are exerting. Nevertheless, by monitoring the $SiO_2$ with the 10X microscope of the machine one notices that at some point when contact occurs the resolution increases. We believe that this is because there are slight vibrations on the sample (induced by the numerous vacuum pumps located near the instrument) that are stopped when we the nanopillars contact it.

To monitor the pressure the most reliable thing that we have found is to look for an interference pattern on the inside of the nanopillars that appears after we are exerting sufficient pressure. When the patter appears we increase the pressure until the interference ends. This usually happen by turning the micrometric screw by a 2/10 of a turn[3].

The main problem encountered through this process is that sometimes the quartz and the sample are not parallel, and since we stamp two pairs of nanopillars at a time, sometimes we only achieve transfer on one of the two pairs. We tried to stamp one pair of pillar at a time, achieving an higher yield but we noticed that those samples had a lower Q factor for the cavities. We believe that this is due to the fact that the edge of the quartz touches the CPW cavity, depositing some quartz dust in the interstice between the two niobium planes.

As stamping is mainly uncontrolled, the following step consists in examining the samples in a STM to see where the nanotubes are located. During this step it is vital to carefully align the STM coordinates with the help of the gold crosses, because the pictures that we take of the nanotube are later used to draw the contacting gates and later lithograph them.

As STM imaging involves shooting high energy electrons on the sample, and therefore on the CNTs, we cannot image the sample many times. Previous experience in our group has shown that high energy electrons can induce displacements in the lattice of the CNTs, further degrading our sample quality. Nevertheless, imaging is an essential step in our fabrication step, therefore we decided to only take one single picture at high resolution and extremely low acceleration voltage (2 keV) of each stamped area. This constraints make imaging CNTs an extremely time consuming

[2] To align we continuously switch focus from the $SiO_2$ sample to the quartz pillars

[3] the screw normally controls the height of the optical mask. A rotation of 0.2 would normally be equivalent to lowering by 20 $\mu m$ the mask. We have not measured how much pressure this translates to in our setup

process, as imaging at 2 keV an insulating substrate with nm-resolutions makes focusing the STM particularly hard.

## 3.2 Measurement Apparatus

In this section I will describe the apparatus in the laboratory that we used to perform the experiment. The setup is composed of 3 sections: a dilution refrigerator to cool down the sample to 30 mK and thermalize the electrical lines coming from the room temperature setup, the DC current generators and measurement apparatus, and the Microwave generation and measurement setup. The setup had been initially assembled by J.J. Viennot and later improved by M. Dartiailh in the ENS. Laboratory [16], and it's design and assembly has not been part of this thesis.

### 3.2.1 Criogenic setup

All the measurement were performed in a wet Dilution Fridge (*Oxford Instruments Kelvinox MX 250*) with a base temperature of 20 mK, but because of a auxiliary pump failure we only operated it with a base temperature of 30-35mK. This fridge is designed to operate continuously for months; for example, sample SQBRESUT-32 has been cooled down continuously for 12 weeks. During operation we perform 3 Liquid Helium Transfers per week to refill the Fridge, and clean the Nitrogen trap once per week by pumping it while heating it to approximately 100$^o$C.

In fig. 3.7(a) a full picture of the fridge insert is reported. The support for the sample holder is located at the bottom of the insert, and above it are located 5 thermalization plates (4.2K, 1.5K, 600mK, 100mK and 20mK). Both the flexible DC lines and the semi-rigid MW lines running from the room temperature equipment to the sample holder are thermalized by at every intermediate plate as can be seen from the schematic 3.8 or fig. 3.7(b-c). DC thermalization is obtained by including portions of copper strip lines running over a *kapton* sheet that is glued with *Stycast* on the fridge frame (fig. 3.7(c-d)).

Thermalization of the inner and outer conductor of the RF lines is achieved through two techniques: at some stages some RF adapters and gold plated connectors are strongly crimped to the thermalization plates, while on other stages 50Ω terminations are thermally anchored to the plates and connected to the RF lines through circulators.

RF cables going down are strongly attenuated ($\approx -60dB$) to preserve the input signal/noise ratio, to prevent hot photons degrading the electronic and fridge temperature and to ensure a small photon number in the cavity,necessary to reach the quantum regime.

In order to maximize the output signal/noise ratio superconducting $NbTi$ cables were used for the output lines to minimize losses. An added benefit of superconducting lines is that one can avoid thermalization as they carry negligible heat. Between the output port of the sample and the output signal cryogenic amplifier there are 2 circulators with one termination blocked at 50Ω, which sensibly ($\approx -18dB$ each) reduce the back action of the cryogenic amplifier on our cQED device. The output cryogenic amplifier amplifies the output signal at the frequencies of our interest

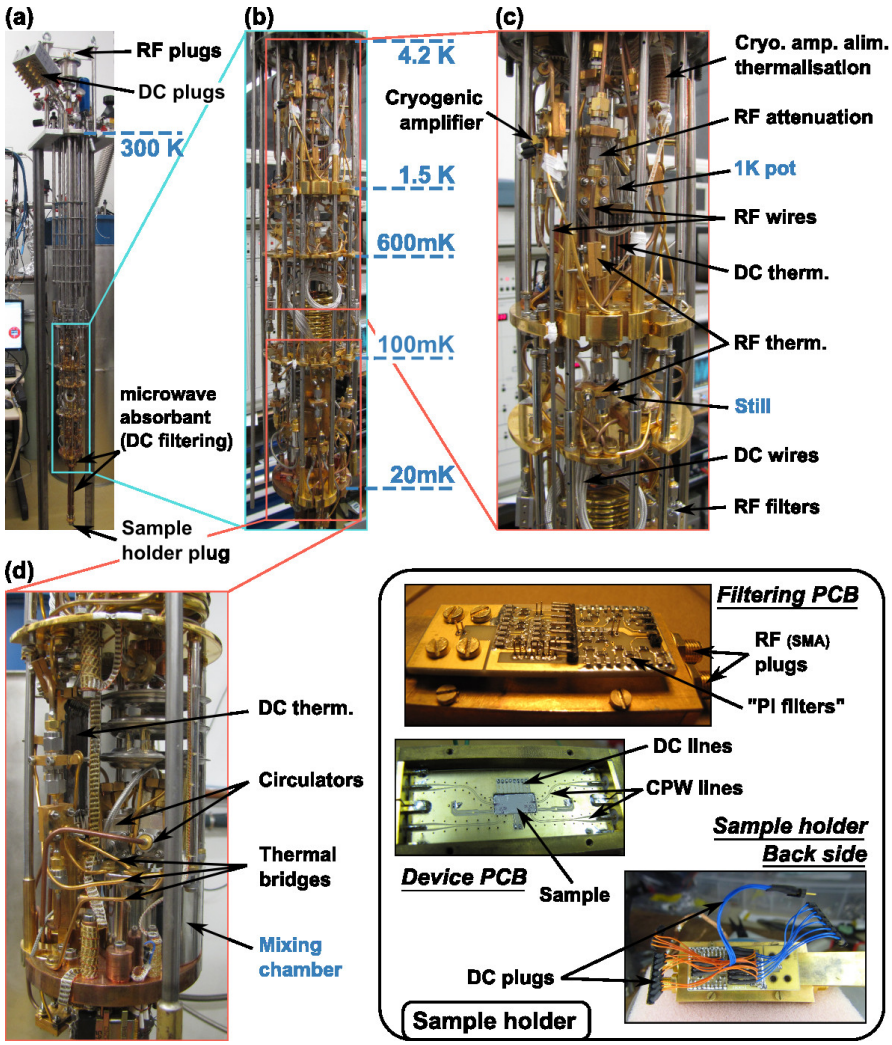


Figure 3.7: Photographies of the dilution fridge insert and sample holder (courtesy of [22]) . (a) Whole view of the insert with the room temperature connections on top, then shields for the helium bath underneath and space corresponding to the inner vacum chamber (IVC), see light blue rectangle zoomed in in (b). The different temperature stages are given by fridge plates on which cryogenic equipment sets the temperature (blue dashed lines). (c), (d) Zoom on the higher and lower part of the IVC showing all the fitted measurement apparatus.

($\approx 7Ghz$) by $+32dB$, and is thermalized to the liquide $He$ bath through the upper thermal plate.

The custom-designed sample holder (insert of fig. 3.7) is a machined solid copper piece plated with gold. In it a Printed Circuit Board (PCB) provides the pads used to bond wires to the Silicium chip sample, $50\Omega$ lines for the RF lines and thermal contact. The holder also is also designed to screen environmental RF frequencies.

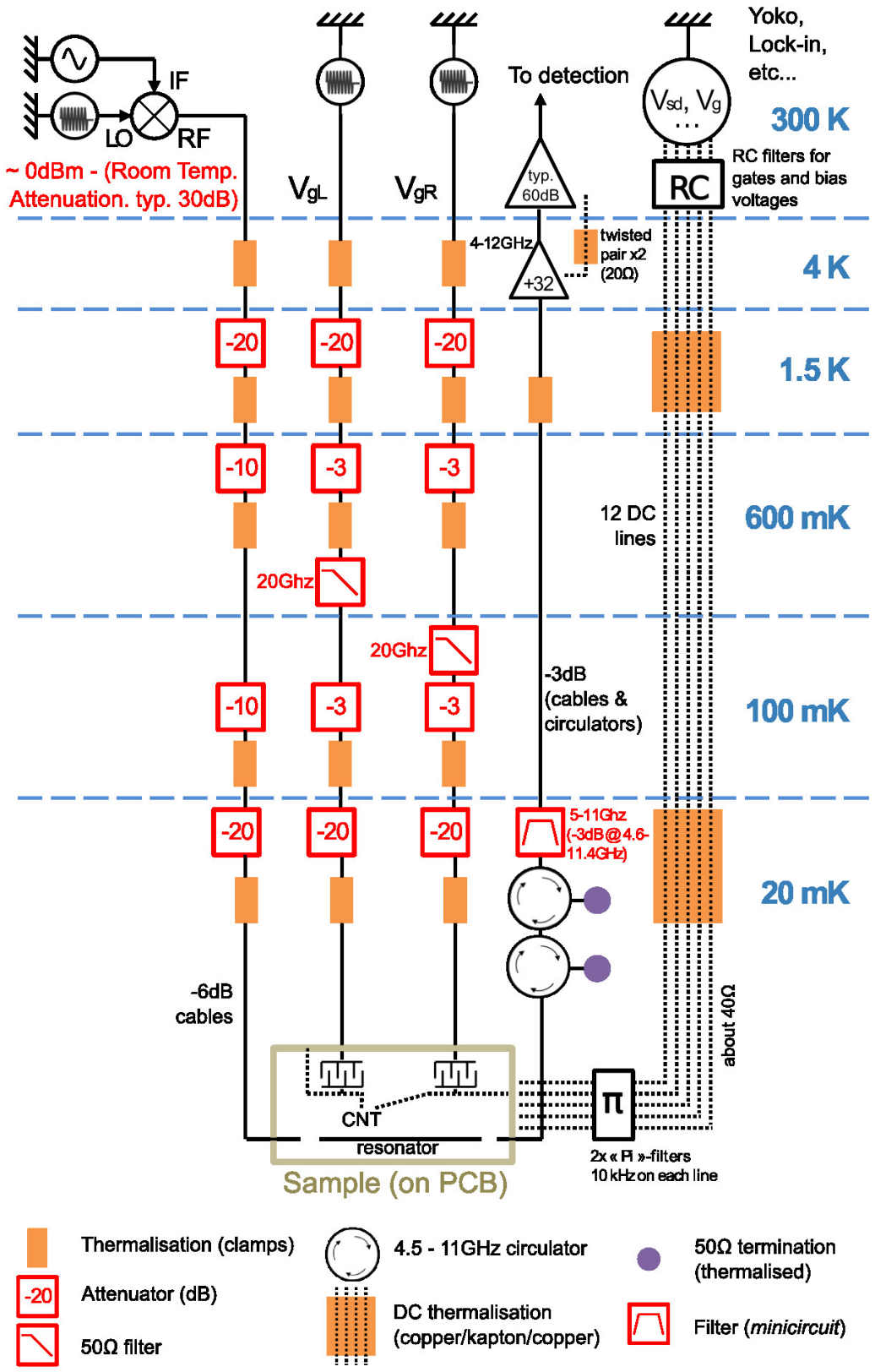


Figure 3.8: Schematic of the thermalisation stages wired inside the frige for DC and MW lines. (courtesy of [22])

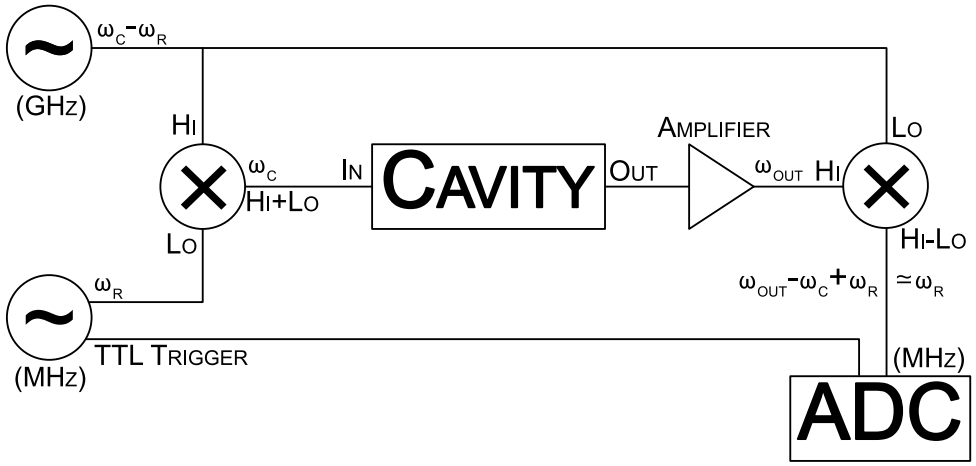


Figure 3.9: Schematic representation of the Microwave measurement setup. The $GHz$ source proviodes a signal at frequency $\omega_c - \omega_r$ sightly detuned from the cavity frequency $\omega_c$. A programmable $MHz$ source provides a second signal at freq. $\omega_r$. Those two signals are fed into a mixer, and only the upper-sideband is taken, which will now be at approximately the cavity frequency, and fed into the experiment. After amplification, the output is fed into an identical multiplier, where the same frequency $\omega_c - \omega_r$ will be subtracted, obtaining a low frequency signal that will be triggered by a logic TTL signal from the programmable source.

### 3.2.2 DC measurements and control

Control of the device is achieved through 3 capacitive gates ($Vg_L$ and $Vg_R$ for the chemical potentials of the two dots, and $Vg_t$ for the tunnel coupling between the dots). The voltages are supplied by *Yokogawa GS200* sources operated in the $10-100$ mV range and controlled from a custom interface on a computer. Those DC signals are carried by resistive wires through the various stages of the fridge, and are passed through three filtering stages: the first stage consists of a home-made shielded RC filters in series cutting of frequencies above the $kHz$. The signals are also attenuated by a factor of 1000 with a voltage divider, reducing the signals to the $10\mu V$ range needed for our experiments. A second filtering stage strongly dissipates microwaves ($3dB/cm$@1Ghz and up to $120dB/cm$@18Ghz). The last filtering stage is made by two pi-filters mounted on a PCB placed on the sample holder, therefore thermalised at the base temperature.

The line carrying the biasing voltage to the device (the source) is filtered in the same way, and usually operated up to $50\mu V$, while the drain (or the output signal for a transport measurement) is connected to a home-made amplifier at room temperature amplifying the total current. Transport measurements where performed with a *Keithley 2000* digital multimeter. Usual integration times for the current measurement is $2-20ms$ and the achieved accuracy is of the order of the $nA$.

### 3.2.3 Microwave measurements and control

The input line for the MW signal of the cavity is heavily attenuated inside the fridge (approximately -66dB including the transmission lines) and outside(-30/-60dB depending on the measurement) allowing us to reach a few (and even single) photon regime and preserving the signal/noise ratio. The output signal coming from the cavity is instead not attenuated until the cryogenic amplifier located at 4K *LNA Caltech SNL012* with a gain of $+40dB$ in the $4 - 12$ $Ghz$ Bandwidth.

Microwave measurements on the cavity were performed in two ways: with a home-made $MHz$ homodyne-like setup and with an *Agilent Portable Network Analyzer (PNA)*. The PNA is the most reliable instrument in terms of calibration and precision in the measurement, though the home-made setup is better suited for continuously scanning a wide parameter range in the DC gates.

With the PNA we measured the transmission characteristic of a bare, uncoupled cavity at cryogenic temperature ($\approx 1K$). By zooming in the frequency window around the cavity resonance we were able to measure the resonant frequency $\omega_c \approx 7Ghz$ and the Quality factor $Q \approx 10000$. Those values were obtained by measuring with a moderate photons number $n \approx 50$[4]

A schematic representation of the homodyne setup is reported in fig. 3.9. In the actual implementation several terminated circulators are present in order to suppress reflections along the lines. The measurement is then performed with a flash ADC operating at a sampling rate of 500 Mhz. The homodyne setup allows us to strongly filter frequencies around a certain frequency $\omega_c$ by modulating (and then demodulating) a lower frequency probe $\omega_r$ over the carrier band at the cavity frequency. Demodulating at a frequency of 20 $MHz$ and sampling at a rate of 500 $MHz$ provides us with 25 samples per period.

[4]Computed using equation 2.40

# Chapter 4

# Experimental Results

As described in section 2.1, the electron charge is naturally coupled to the electric field and so to the electromagnetic field of the cavity. Therefore the most elementary measurement that one can perform on the device that we described in section 1.5.2 is a test of this cavity-charge coupling. Assessing it's presence and it's relative strength is fundamental if we want to progress towards the study of the effective electromagnetic field that we have engineered in our device, the Spin-QuBit. After having verified the presence of the cavity-charge coupling we had planned on performing spectroscopy of the device, to study it's excited states and see if they are also coupled to the spin degree of freedom. This step by step approach is very similar to what has been done in studies of competing architectures, such as superconducting QuBit [25] or InAs QuBits [26].

Int his chapter we will present low bias measurements on two devices, a test device that present a symmetric coupling between the cavity and the charge (section 4.1.1) and the real Spin-QuBit device, with an asymmetric coupling (section 4.1.2). The results for the Spin-QuBit device are fitted to the theory of section 2.3.2, and agreement between the two will be demonstrated. In section 4.2.1 we characterize the AC/DC coupling capacitor described in section 3.1.2. The chapter ends with a brief presentation of our late attempts at spectroscopy, that unfortunately gave no results.

## 4.1 Low Bias Measurements

In this section we will describe measurements performed by applying a low DC voltage ($\sim 50\ \mu V$) on the sample across the source and the drain electrodes. We expect this to place the sample in the Coulomb Blockade Regime which has well defined electronic states separed in energy. Moreover, such a low DC voltage falls into the linear Regime condition ($V_{DC} < k_b T$) and therefore we expect to be able to describe our results with the theory developed in chapter 2.

### 4.1.1 Simmetric Coupling

Coupling the photonic field to different electronic dipoles inside the DQD allows us to observe different properties in the electronic structure of our device. Though our objective is that of obtaining a strongly asymmetric coupling, we started by

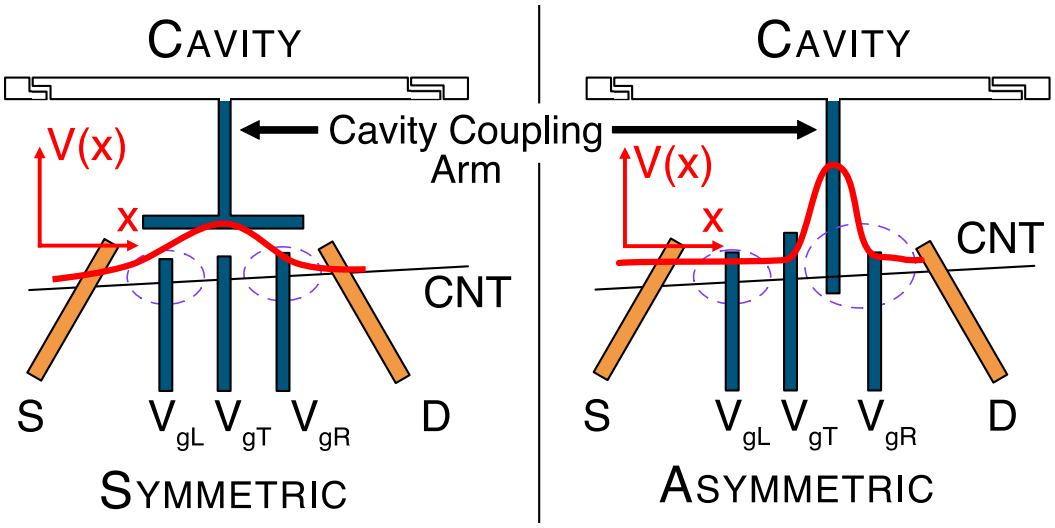


Figure 4.1: Comparison between a symmetric and asymmetric cavity-DQD coupling. The red solid line plotted is a qualitative representation of the photonic pseudopotential describing the coupling between the charge in the DQD structure and the photons in the cavity, while the dashed violet line gives an idea of the approximate locations of the Left and Right dots. The Symmetric case corresponds to sample SQBRES-10R, presented in this section, while the asymmetric case corresponds to the Spin-QuBit device studied later.

studying a simpler device, similar to what was described in section 1.5.2, but where a symmetric coupling between the field and the charge degree of the DQD was engineered. This was done to allows us to compare the qualitative behavior of the two devices, and confirm that our understanding of the coupling was correct.

In this sample (SQBRES-10R)[1] a symmetric coupling between the L/R dots and the cavity is obtained by evaporating a small superconducting coupling arm $5\,\mu m$ from the DQD, without any electrode connecting the cavity and the nanocircuit. Since there is no cavity coupling electrode evaporated directly on top of the nanotube, we expect the coupling in this test device to be weaker than what we will find in our real device, the Spin-QuBit.

For a depiction of the potential confining the charge in the DQD the reader can refer to fig. 1.4, which is valid on both the DQDs studied in this chapter.

Another interesting feature that we can investigate is the *openness* of the DQD: the transition rate between the S(D) lead and the L(R) dot play an important role in the coherence time of the charge QuBit, and we would want it to be low enough as to have an high coherence time. This coupling can be symmetric or asymmetric, depending on fabrication (this device was designed to have a symmetric lead coupling), and it can be understood in terms of lever arms, where the arms are simply ratios of capacitances that explain the tilting of the traditional DQD stability diagram (fig. 1.6, also seen in fig. 4.2).

We expected the coupling capacitances between the S(D) leads and the L(R) dot

[1] This is a sample that had been fabricated in the lab prior to my arrival in the group.

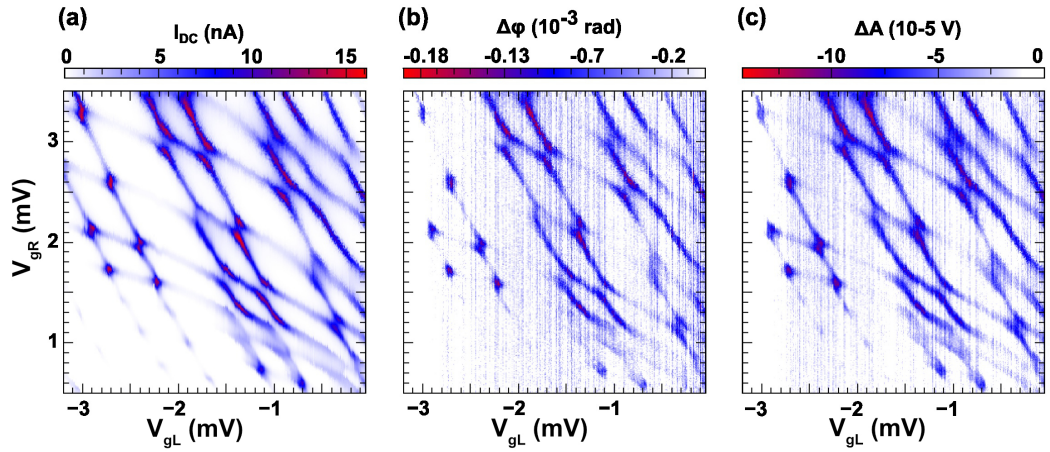


Figure 4.2: Stability Diagram for the sample SQBRES10R measured at bias $V_{SD} = 10\mu V$ and $V_{gt} - 200\mu V$. **(a)** DC current flowing through the DQD measured as a function of $V_{gL}$ and $V_{gR}$. **(b,c)** Phase and amplitude variation of the microwave signal. The measurement that yielded those 3 graphs ran for approximately 48 hours.

$C_{l,i}$ to be of the same order of magnitude, as we have not introduced any feature in the design to prevent this. This can be verified by looking at the diamonds in fig. 4.2(a): a pattern of alternating small-big-small diamonds can be seen by looking at the DC conductance measurement, where the smaller diamonds can be attributed to the filling of 2 electron spin-triplet state [10]; neglecting the smaller diamonds, we can extract the ratio between the coupling capacitance Source-Left dot $C_{S,L} \propto \Gamma_{S,L}$ and the coupling capacitance between the Drain and the Right dot $C_{D,R} \propto \Gamma_{D,R}$ with a simple procedure.

The procedure is the following: first we identify one of the bigger diamonds[2]. A diamond is delimited by 4 longer lines (cotunneling) and 2 shorter (often not clearly defined) lines (L/R degeneracy); we are interested in the longer cotunneling lines, which come in pair of 2, each one representing a Left or Right cotunneling event. The more vertical lines (those that are crossed when varying $V_{gL}$) represent Left cotunneling events and their length is proportional to $\Gamma_{S,L}$, while the more horizontal lines (those that are crossed when varying $V_{gR}$) represent Right cotunneling events and their length is proportional to $\Gamma_{D,R}$. Measuring the length yields the approximate value $R = \Gamma_{D,R}/\Gamma_{S,L} \simeq 1.3$.

In panels **(b)** and **(c)** of fig. 4.2 the variations in the transmitted phase and amplitude across the cavity are presented, as a function of the two gate voltages controlling the chemical potentials of the L/R dots. We acknowledge that they report approximately the same features that can be seen from the DC measurement **(a)**, as we expected after having shown in section 2.2.3 that the Transmission of the cavity depends on the properties of the susceptibility $\chi$ of the coupled circuit.

[2]In theory each big diamond should give the same result, in practice, there are many potentials that change the coupling depending on the control voltages, often yielding very different results depending on which diamond one considers. Nevertheless, if those vary slowly enough, the results will hold for a diamond and those diamonds immediately next to it.

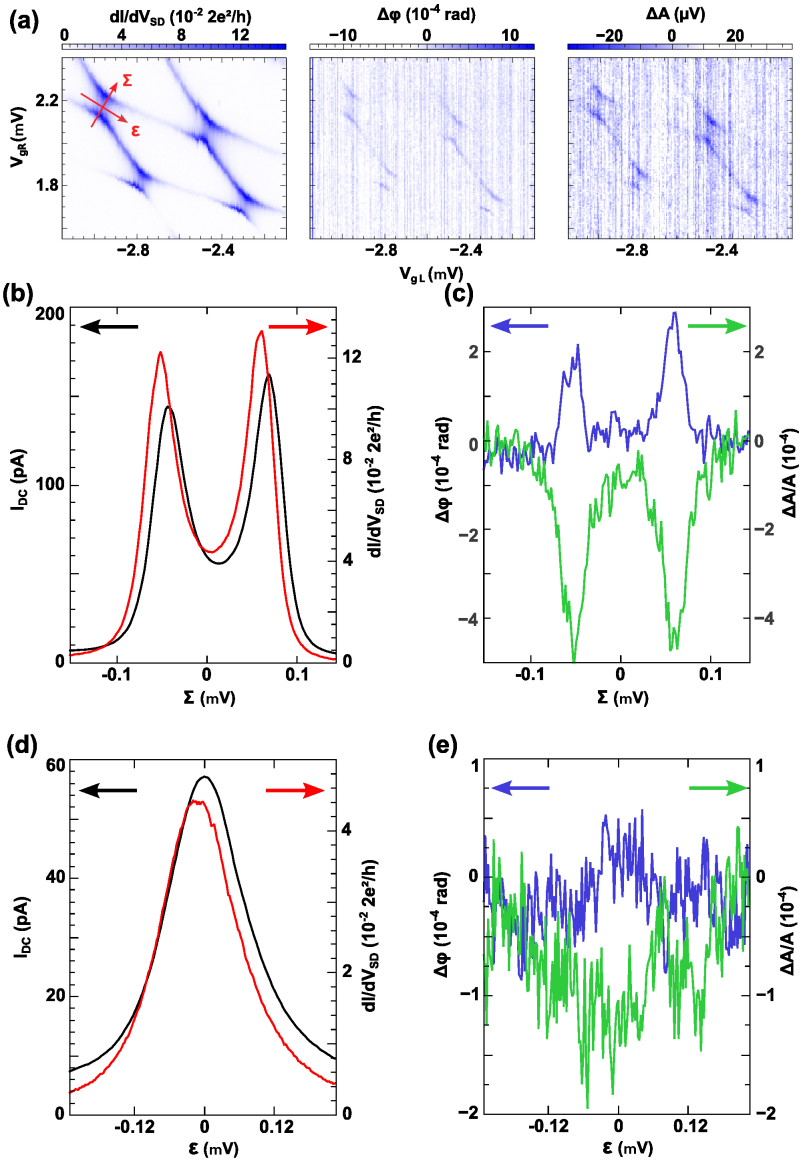


Figure 4.3: Detailed zoom of a smaller region in ($V_{gL}$, $V_{gR}$) of the stability diagram with an higher $V_{SD} = 40\,\mu V$. **(a)** shows the differential conductance, phase shift and amplitude variation across this area. **(b)** DC current (Black) and Differential Conductance (Red) measurements along the Σ direction as shown in (a). **(c)** Transmitted phase (blue) and amplitude (green) along the same direction Σ. **(d,e)** same measurements along the $\epsilon$ direction.

Since those maps are taken by scanning only at the cavity resonant frequency $f_c \approx 6.92\ GHz$, the minima in the transmitted amplitude can be thought of as changes of the resonance frequency due to the cotunneling events. In the DC measurement performed at low bias we would expect not to see a change in the current between the areas (N,M) and (N-1,M+1), but we do not have an high enough resolution in the DC measurement to distinguish this region. Moreover, by looking at the

curvature of the cotunneling lines in the DC measurement, we can extract a value for $t \approx 15\ \mu eV \approx 30\ GHz$.

The coupling between the dots and the cavity can be described through two capacitances $C_{c,L}$ and $C_{c,R}$. Since the device is pretty much symmetric, we expect those two values to be similar in magnitude. From those we can extract the two lever arms for the cavity coupling $\alpha_{L(R)} = \sum_{i=\{L,R\}} {}^{C_{c,i}}/_{(C_{c,L}+C_{c,R})}$. The coupling is symmetric if $\alpha_L \approx \alpha_R$. To estimate the lever arms we need to study some processes symmetric ($\propto \alpha_{L/R}$) and asymmetric ($\propto \alpha_L - \alpha_R$). Those two quantities will be presented soon after in fig. 4.3(c).

In fig. 4.3 we report some additional, more precise measurements performed on a specific region of the ($V_{gL}$, $V_{gR}$) map previously presented. To choose this region we zoom on the Left to Right transition line of a single diamond where the cotunneling lines are sufficiently thin (the coherence time is sufficiently long) but still can be easily distinguished from the background. Moreover, often some areas result noisier than others, with noise often appearing in front of our data and therefore rendering some of those areas not available for measurement. Since we have not yet found some precise and quantitative markers to guide us in the choice, choosing the area where to zoom in is a qualitative, essentially trial and error process.

Figure 4.3(a) shows a positive phase shift along the lines where there is a decrease in the transmitted amplitude, which we can interpret as a positive cavity frequency shift $\Delta f_c$[3]. In panel (c) we present a cut of the cavity-measured data along the $\Sigma$ direction, therefore perpendicular to the L/R transition line. Following this cut we cross both the Left and Right cotunneling lines, going from a (N,M) diamond to a (N+1,M+1) diamond (a symmetric process); following the simple model described in the additional materials of [4] we expect the height of the two peaks in this panel to be proportional to the square of the L and R lever arms $\alpha_L^2$ and $\alpha_R^2$. A cut along the $\epsilon$ direction is presented in fig. 4.3(e): following this direction we are crossing the L/R transition line, therefore going from the (N+1,M) diamond to the (N,M+1) diamond (an asymmetric process). We expect the height of the peak to be proportional to $(\alpha_L - \alpha_R)^2$, and measuring a very small peak, as opposed to what is measured by the current (fig. 4.3(d)), confirms that the coupling is symmetric.

Lastly, knowing the the mutual charging energy $U_m$ gives the main contribution to the width of the L/R degeneracy line, we use the distance between the two peaks in **(b)** to estimate $U_m \approx 100\ \mu V$[4].

Summing up, we have quantitatively verified that we can achieve a symmetric coupling between the cavity and the DQD. The sample also shows a very high L/R transition frequency $t \approx 30\ GHz$ which is much higher than the cavity frequency, and therefore the cavity is coupled weakly to the transition and we will not be able to extract more informations from this sample in the framework of the proposed model. The reason being that the theory presented in section 2.3.2 requires the L/R transition energy and the cavity frequency have to be in tune $\omega_c \approx \sqrt{\epsilon^2 + 4t^2}$ to see an interplay between the two and therefore extract more informations.

[3] This can be inferred from the graphic in fig. 2.1.

[4] For the explanation, see fig. 1.6(e)

### 4.1.2 Asymmetric Coupling

In this subsection we will present the results obtained by studying the device engineered in section 1.5.2 (the Spin-QuBit) and fabricated following the techniques outlined in section 3.1.2. All the data presented here was obtained from sample SQBRESUT-32UR, which was fabricated in late April 2016. In this device the cavity is capacitively coupled to (approximately) only the Left dot of the DQD, as represented in the left part of fig. 4.1. The cavity has a resonating frequency of approximately $f_c \approx 7.2\ GHz$. The quality factor of the bare, uncoupled cavity, that we refer to as bare quality factor was measured on a device with no nanotube and is approximately $Q \approx 1$ Million. This Q factor greatly degrades after stamping the nanotube and contacting it with the cavity, resulting in a quality factor $Q \approx 5000$ at the end of the fabrication process.

The first measurement that we performed on the device is the same stability diagram measurement that we had done on the previous device and reported in fig. 4.2. The measurement that we obtained is reported in fig. 4.4. In this plot we report only the transmitted phase and amplitude, and we do not report the transmitted current, which instead was present in the previous sample. This is because to obtain a sensible measurement in the current we needed to average at least $100\,ms$ per point, leading to very long measurement times (taking a not-extremely detailed map like those in fig. 4.4 took approximately 7-8 hours). Long measurement time, coupled with the variety of random noises that we had and some drift effects, made obtained data extremely noisy and hard to understand. The drifts we noticed in our data were particularly noticeable when the set took more than $t > 300$ min to record; during those measurements, after some time, the various features saw in the previous graphs started to disperse with a different speed and became more blurred, lowering our contrast. Another issue we found was that sometimes the data we were looking for would disappear, and a very high and broad peak in the transmitted power/phase would appear in place of what we expected, always in random positions, disappearing after some time. We believe that this is due to some charges trapped in the Si substrate or in some defects of the nanotube, that suddenly come in resonance with our system. We have not investigated the issue, as we found that by speeding up the measurement we could prevent the vast majority of those *modes* from appearing. To speed up the measurement we simply stopped recording the transmitted current data: since cavity measurement are at least 20 times faster ( to generate a point we usually average 5000 traces $1000\,ns$ long ), by not recording the current we were able to sensibly reduce measure time and therefore ignore the effects described previously leading to much cleaner data samples. To give an idea, the not detailed dataset of fig. 4.4 took only 25 minutes to be measured, while the much more detailed data in fig. 4.5 was taken in 3 hours.

The behaviour found in fig. 4.4 is qualitatively different from the $\Delta A/A$ and $\Delta\phi$ measured in the previous samples. The main characteristics that we note are:

- The stability diagram is found by scanning the ($V_{gL}$, $V_{gT}$), when we would expect $V_{gT}$ to control the tunneling rate $t$, and the stability diagram to be in the ($V_{gL}$, $V_{gT}$) space.

- We see a negative phase response along the L/R degeneracy line. This is

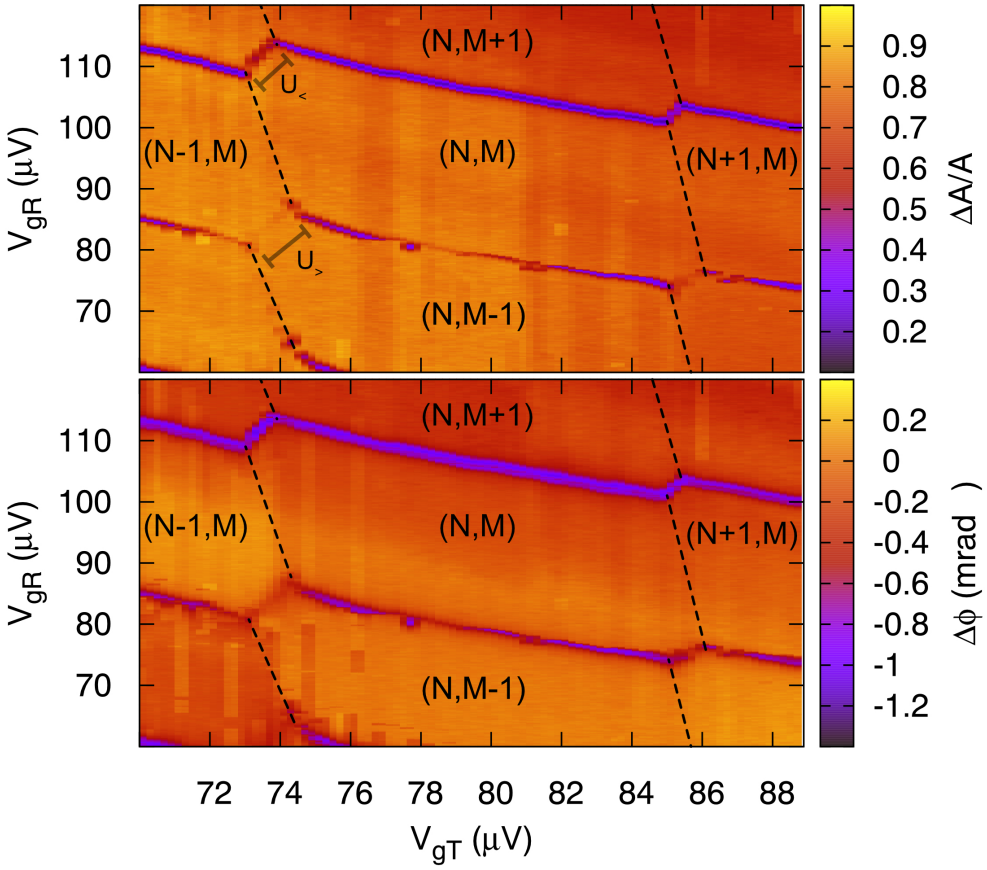


Figure 4.4: Measurement of sample SQBRESUT-34UR with $V_{SD} = 15\ \mu V$, $V_{gR} = 30\ \mu V$ **(a)** Amplitude variations as a function of $V_{gT}$ and $V_{gL}$. $V_{gT}$ in this sample is coupled to the charge as $V_{gR}$ in the previous. The dashed lines follow co-tunneling lines, outlining a stability diamond with occupation number (n,m) in DQD. **(b)** Phase variation measurement in the same range of parameter, performed at the cavity resonance.

expected in the case of asymmetric coupling.

- Only right cotunneling lines are visbile in the plot, while the Left are barely visible if not visible. This is due to the asymmetric coupling of the cavity to the DQD: as the cavity is coupled only to the $R$ dot, we can only probe Right cotunneling events such as $S \to R \to D$ and not left cotunneling events such as $S \to L \to D$, as those interact only weakly with the right dot, and therefore with the cavity.

From those plots we see that cotunneling lines are narrower compared to the previous sample, which is a signature for a smaller value of $\Gamma_{Lead}/U_m$. As previously, we can estimate the mutual charging energy from the length along the $\Sigma$ direction of the L/R degeneracy line, obtaining a value of $U_m \sim 10\mu eV$.

A well defined zero-detuning region ($\epsilon = 0$) can be identified, and we expect to be able to couple to the transition between the Bonding and Antibonding orbitals

through the cavity, effectively operation the device as a charge QuBit.

#### Interpretation of the anomalous $V_{gT}$ coupling

At the start of the measurement session for this sample we started to search in the ($V_{gL}$, $V_{gR}$) parameter space. Unfortunately we never found any area that looked qualitatively like the L/R degeneracy line. Only later we tried to search in different combinations of parameters, finally resulting in the plot here reported. We also point out that a line qualitatively similar to the L/R transition was found in the ($V_{gR}$, $V_{gT}$) space, while $V_{gL}$ was only weakly coupled to the DQD as it was barely affecting it's spectrum. Our interpretation is that in this sample the R orbital is localized where we expect it, approximately under the $V_{gR}$ electrode (refer for example to fig. 1.3), while the L orbital is shifted and is localized under the top electrode. The fact that the two orbitals are located at a lower distance would also explain the increase by one order of magnitude of the mutual charging energy. The existence of a tunnel barrier between the L and R orbitals in the absence of a real electrode applying a negative potential between the two could also be explained if the L/R atomic orbitals are essentially defects localized under the electrodes, which naturally bound to electrons. We think the defect could be a displacement of a C atom in the CNT structure happening during evaporation of the electrodes. This explanation would also be consistent with the observation that our QuBit was extremely hard to control and often coupled to external noise sources. We believe that with additional studies we could test this theory, but as it was not the aim of our work, and the device appeared to work even if with no control on $t$, we decided to continue on our research ignoring this phenomena.

### 4.1.3 Resonant Regime measurements

In fig. 4.5 we report a measurement similar to that in fig. 4.4 performed with an higher accuracy in a different area of the parameter space. We report a L/R transition line where we can extract an even lower mutual charging energy $U_m \approx 5\ \mu eV$. Around the $\epsilon = 0$ (zero detuning) line two negative dips in $\Delta\phi$ appears. In the same region we notice that the transmitted amplitude decreases by approximately 1%.

We will now interpret those results through the theory described in section 2.3; in particular by combining eqs. (2.59) and (2.63) to (2.64) we can show that:

$$\frac{\Delta A}{A} \propto \mathcal{R}e[\chi](\epsilon) \quad = g^2 \frac{\Delta}{\Gamma_2^2 + \Delta(\epsilon)^2} \tag{4.1}$$

$$\Delta\phi \propto \mathcal{I}m\left[\chi\right](\epsilon) = g^2 \frac{\Gamma_2}{\Gamma_2^2 + \Delta(\epsilon)^2} \tag{4.2}$$

where $\Delta(\epsilon) = \sqrt{\epsilon^2 + 4t^2} - \omega_c$.

If $\Delta(\epsilon) > 0\,\forall\epsilon$, for example when $t \gg \omega_c$ as in the previous sample, both the Imaginary and Real part of $\chi$ are always positive and they have a trivial shape with a single global minima.

[5] The cut is obtained through bilinear sampling along the $\epsilon$ direction. Approximately 150 points are sampled. We average across 20 parallel cuts shifted along the $\Sigma$ direction.

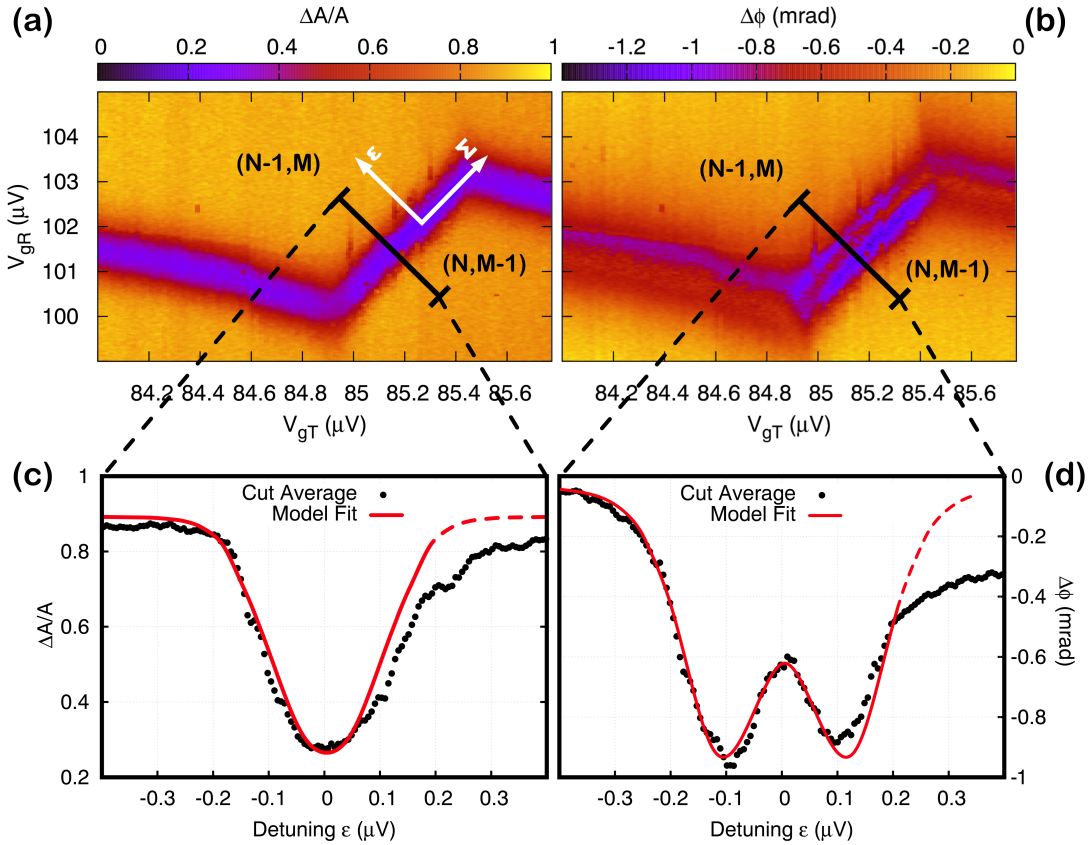


Figure 4.5: DQD response for $V_{SD} = 5\ \mu V$ and $V_{gL} = 40\ \mu V$. In **(a)** and **(b)** a color map for the transmitted amplitude $^{\Delta A}/_{A}$ and phase variations $\Delta\phi$ as a function of the two gate voltages $V_{gR}$ and $V_{gT}$. The map is centered on a L/R degeneracy line separating the charge states $(N, M)$ and $(N-1, M+1)$ (tilted line going upwards) and the two Right cotunneling lines are visible to it's left and right; Left cotunneling events are not visible. In **(c)** and **(d)** a cut along the $\epsilon$ direction, averaged along $\Sigma$ is reported[5]. Black dots are experimental points extracted from the cut, and the red line is obtained by fitting data of **(d)** with eqs. (2.59), (2.63) and (2.64). We dashed the fit line where there is no match between the model and experiment. From the fit we extract $t \approx 3\ GHz$, $g \approx\ 50 MHz$ and $\Gamma_2 \approx 400\ MHz$.

When instead $t$ is small enough so that $\sqrt{\epsilon^2 + 4t^2} < \omega_c$ then $\Delta(\epsilon) < 0$ and two local minima can appear symmetrical respect to $\epsilon = 0$. In the data reported in fig. 4.5(d) we observe two local minima in the transmitted phase $\Delta\phi$ located at $\epsilon_\pm = \pm \simeq 0.1\,\mu eV$. At the minima we have $\Delta(\epsilon_\pm) = 0$ therefore $\mathcal{I}m\,[\chi]\,(\epsilon_\pm) = {}^{g^2\Gamma_2}/_{\Gamma_2^2} = {}^{g^2}/_{\Gamma_2}$. The depth of the minima is therefore proportional to the ratio $R = {}^{g^2}/_{\Gamma_2}$ between the square of the coupling strength and the dephasing rate $\Gamma_2$, and since this depth can be extracted from the data without doing a complex fit, we use the extracted value $R \simeq 0.8$ to constraint the fit of $\mathcal{R}e/\mathcal{I}m\,[\chi]\,(\epsilon)$ on the experimental data. This is handy trick that effectively reduces the fit from the three parameters $t$, $g_0$ and $\Gamma_2$ to only two.

Focusing on fig. 4.5(c) we observe a single, wide, global minimum. Our model

predicts that this happens when $2t + \Gamma_2 > \omega_c$, but we know from the analysis on the phase that $2t < \omega_c$, therefore we have a $\Gamma_2 > \omega_c - 2t$. If $\Gamma_2 < \omega_c - 2t$ then we could observe two local minima and a maximum in between on the amplitude (see fig. 2.3).

Just by looking at the features (presence/absence of minima) in our data, and without having yet performed any statistical regression we have extract information about the tunneling rate, $2t < \omega_c$ and about the charge decoherence time $\Gamma_2 > \omega_c - 2t$.

By performing a cut along the $\epsilon$ direction we are able to fit our simple model to the data. We perform the cut by centering it at $V_{gT} = 85.1\ \mu V$[6] and obtain from the fit the order of magnitudes for $2t \approx 6.4\,GHz$, $g_0 \approx 50\,MHz$ and $\Gamma_2 = 1.0\,GHz$. The tunnel barrier we have achieved is very opaque compared to what is conventionally achieved in CNTs [23], but because we have no real control on $t$ on this sample, we could not investigate if this is a consequence of the particular localization of one of the two dots, which might live on a defect; investigating other samples might shed light on the issue.

Note that with this fitting model we can only extract the total dephasing $\Gamma_2 = \gamma/2 + \Gamma_\phi$ and not the two separate value of the charge relaxation $\gamma$ and the dephasing $\Gamma_\phi$. To determine the two separate quantities a spectroscopic measurement of the energy levels of the QuBit is needed.

By looking at the cut and our best fit in fig. 4.5(c-d) we notice that the two phase minima have slightly different depths and this is not well reproduced by our model. We believe the reason for that lies in the simplistic description of our model: it considers a cavity coupled to the B/AB transition, neglecting the fact that, in the real sample, we are really only coupled to one of the atomic orbitals, the Left one. We could express this asymmetry by considering two different cavity-orbital couplings $g_L$ and $g_R$, and the total coupling between the cavity and the B/AB transition as a crossover function. Since the depth of the amplitude dips depends on the coupling to the A/AB transition as $g^2/\Gamma_2$, we would get a different depth for left and right dip. Adding another fitting parameter, however, in the absence of further data is not very wise (as we would make the fitting easier), and we decided against this until we had more data available.

Moreover, we also see that the fitted curve does not reproduce the height in the area between the two dips, as our model predicts a lower value of the amplitude. Similar issues when fitting experimental data with Equation of Motions models computed in the steady state are common in the literature [21], and it is usually justified by saying that self consistency of the cavity field is not enforced (thus violated) when performing this calculations in order to obtain a closed set of equations.

## 4.2 Spectroscopy attempts

We have now verified that the sample behaves like a DQD, and we have extracted the orders of magnitude for the parameters that control it's spectrum, verifying that we have achieved a strong coupling between the cavity and the QuBit. The natural prosecution of the work is to try to identify the excited states of the system and asses

[6] We remember that in this sample $V_{gT}$ behaves as what we usually label as $V_{gR}$.

the transition rates between those levels. To do so, we planned to send some high frequency pulses on $V_{gL}$, and sweep the frequency and amplitude of those pulses. Before proceeding with the spectroscopy we needed to validate the design of the AC-DC capacitor used to mix the two components of $V_{gL}$, and to extract a ratio in of the AC to DC coupling strength.

### 4.2.1 AC/DC Mixing Characterization

Since the sample studied in the previous section, SQBRESUT-34R, is not strongly coupled to $V_{gL}$ we did not expect a strong coupling to the AC signal either (as in fact our failed attempts at spectroscopy will show), and therefore we decided to check the AC/DC mixing on another sample (SQBRESUT-27UL) which had a damaged resonating cavity. We had initially neglected this sample as it's very low Q factor prevented us from measuring any meaningful signal from the cavity, but to measure the mixing ratio a DC measurement is sufficient.

To test the relative coupling, we first obtained a ($V_{gR}$, $V_{gL}^{DC}$) map (fig. 4.6(a)) and tried to identify some lines dispersing in $V_{gL}$. We could not recognize patterns similar to those shown in previous maps, but we could still identify lines that looked line cotunneling lines, as the DC current has a peak along them. Even if we could not clearly label them, we still see that they dispersed similarly in $V_{gL}$ and therefore they can be used for our purpose.

We identified a value of $V_{gR}$ where we had some clearly distinguished peaks, and then we perform another scan at fixed $V_{gR}$ by varying $V_{gL}^{DC}$ and $V_{gR}^{AC}$, visible in fig. 4.6(b).

We expect that by sending a low frequency square wave with amplitude $V_{gL}^{AC}$ on $V_{gL}$ the system will spend half of it's time at $V_{gL} = V_{gL}^{DC} + V_{gL}^{AC}/2$ and half of it's time at $V_{gL} = V_{gL}^{DC} - V_{gL}^{AC}/2$, therefore the peaks of the previous maps will split in two different peaks; and by increasing the amplitude of the AC signal, $V_{gL}^{AC}$, we expect the peaks to spread out even more, until they eventually merge with other peaks.

This means that in the colormap plotted as a function of $V_{gL}^{AC}$ and $V_{gL}^{DC}$ the peak in transmitted amplitude will appear as a horizontal V-shaped signal (see fig. 4.6): the point where the two *legs* of the V merge is at $V_{gL}^{AC} = 0$, because with zero microwave power the system stays in a single state the whole time, but by increasing $V_{gL}^{AC}$ the peak splits in two peaks (the legs of the V), corresponding to the two values of $V_{gL}$ at the max and min of the square wave.

The inclination of those lines depends on the ratio of the AC and DC couplings, therefore we can give an estimate of R simply by computing $R_{DC/AC} = \Delta V^{DC}/\Delta V^{AC} \simeq 2.5\,\mu V/\approx 1.25\,mV \simeq 500$. This ratio confirms that, through the mixing capacitor and the transmission lines, we achieve a much stronger coupling to the DC component as opposed to the DC component. Nevertheless, a microwave amplitude of 1 mV on the sample, after a chain of -57 dB attenuators, is equivalent to a peak to peak voltage of $V_{pp} = 1.35V$ on the microwave generator, which is well within the range of our experimental setup, and therefore we can still explore the coupling to $V_{gL}^{AC}$.

An interesting thing is the quasi-horizontal line, highlighted with a dashed blue segment, that in fig. 4.6(b) does not disperse in the microwave power. Those lines

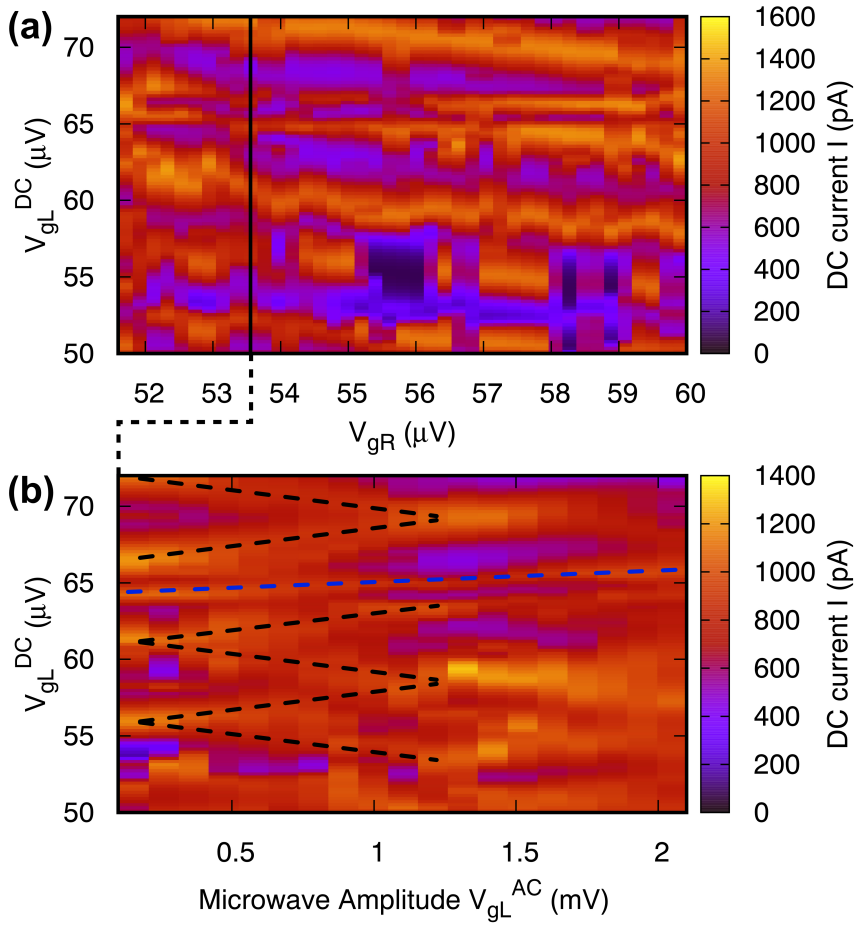


Figure 4.6: DC current measurements on sample SQBRESUT-27UL, with $V_{SD} \approx 200\ \mu V$. **(a)** shows the usual map in the two DC parameters ($V_{gR}$, $V_{gL}$). The vertical line at $V_{gR} \approx 53.6\ \mu V$ represents the value where we performed the second measurement. In **(b)** the measurement at fixed $V_{gR}$ and varying AC/DC intensity of $V_{gL}$ is presented. The splitting of the conductance peaks in two is visible for the two peaks below the blue line. All those lines have the same angular coefficient. The peak above the blue line ($V_{gL}^{DC} \approx 66\ \mu V$) does not split, but this might be related to the presence of an horizontal, thin line (dashed blue) that does not disperse. We believe this to be the coupling of the conductance to some inner defect.

are typical of damaged or not clean samples, and they show the coupling of the conductance to some inner mode, typically that of a defect [27][7].

[7] Unforunately Carbon Nanotubes DQDs have been investigated only recently, and the literature is still in it's infancy. For that reason, those modes have not yet been extensively studied, and the reference here refers to Lattice defects in Superconducting QuBits, which present a very similar measurable signature.

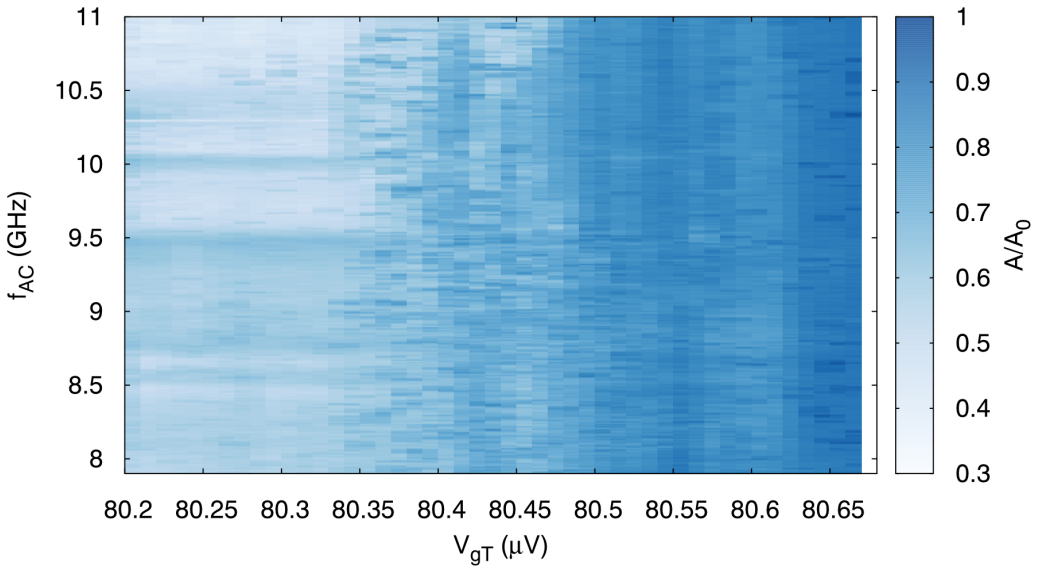


Figure 4.7: Spectroscopic measurement with no clear result. We span the interval above the cavity frequency for $f_{V_L} \in [7.8, 11]\ GHz$ in a small range of $V_{gT} \approx \epsilon \approx 0$. Some constant frequency lines (horizontal) are visible. If those were dispersing as a function of $V_{gT}$ we could interpret them as transitions to excited states, but they do not.

### 4.2.2 Attempting spectroscopy

After having made sure that our AC signals where coupled to the DQD we attempted to perform spectroscopy on sample SQBRESUT-32UR. This sample is not ideal for spectroscopy, as we can send fast pulses only on $V_{gL}$, and as described previously $V_{gL}$ is not very coupled to the DQD. We believe this to be the main reason for our failure, but since Fabrication is a 3 weeks long process, and because of bad luck with 2 subsequent batches and we had no samples available for months and we attempted anyway.

Spectroscopy was attempted by taking measurements near the L/R degeneracy line, where the B/AB transition is lower in energy, as the one previously described in fig. 4.5 and by changing the frequency and/or the amplitude of the signal. By creating a map in $\epsilon$ and $f_{AC}$ we expected to see some lines appear and disperse in $f_{AC}$ as a function of $\epsilon$, because changing $\epsilon$ would change the orbital energies.

No lines dispersing in $\epsilon$ where observed (the results of one of those measurements is reported in fig. 4.8 ).

Other than the poor coupling between the DQD and $V_{gL}$ we attribute the negative result of this experiment to the fact that each measurement of $\Delta A/A$ and $\Delta\phi$ is obtained by performing FFT on the average of $N \approx 1000 - 10000$ traces, each $1000\,ns$ long. But since at low $\epsilon$ we expect the excited states to have poor coherence times, we think that the DQD spends most of it's time in the ground state, reducing the Signal-to-noise ratio of the signal we are looking for.

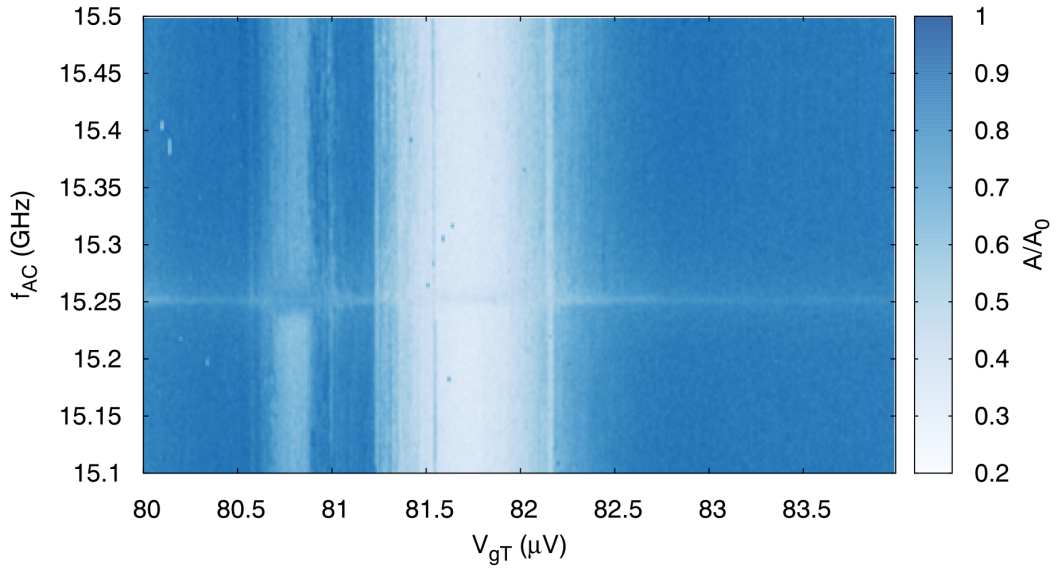


Figure 4.8: Same measurement, for $f_{V_L} \in [7.8, 11]\ GHz$. The two vertical minima in the transmitted amplitude correspond to the $\epsilon = 0$ structures seen before, because what is seen is a cut along the $V_{gT} \approx \epsilon$ direction, and therefore by varying $\epsilon$ we cross the two minima. The single horizontal line appearing at $f \approx 15.2\,GHz$ is unxpected: we expected a similar line at $f = 2f_c = 14,4\,GHz$, at twice the cavity frequency, but this one is too much detuned from it.

# Chapter 5

# Numerical Study of a Landau Zener Manipulation

The final objective of our research is to measure the coherence time $\tau_2$ of our Spin-QuBit design. A standard experiment that allows to measure the $\tau_2$ of a QuBit is known as 'Rabi Spectroscopy'. Rabi spectroscopy on a simple two level system (B/AB) consists in monitoring the amplitude of the time-oscillations in the wavefunction of a mixed population state such as $|\psi\rangle = {}^{(|B\rangle + |AB\rangle)}/\sqrt{2}$: the amplitude of those oscillations decay exponentially, and the decay constant is $\tau_2$.

As we have already said, we modeled our CNT based spin-QuBit system as a 4 level system, where 2 are due to the charge degree of freedom and 2 due to the spin degree of freedom. If we label all states available to the system with $|0\rangle$ , $|1\rangle$ , $|2\rangle$ , $|3\rangle$ so that $E_0 < E_1 < E_2 < E_3$, our QuBit is represented by only the two lowest level eigenstates, as they are immune to charge noise for a sufficiently high detuning $\epsilon$ (see the discussion of section 1.5.2). In the two level system the initial superposition of $|B\rangle$ and $|AB\rangle$ can be created starting only from the lowest level eigenstate $|B\rangle$ through a fast $\epsilon$ sweep, a Landau Zener Transformation. For our 4 level system we were unsure if such a procedure could still work to create the superposition $|\psi\rangle = {}^{(|0\rangle + |1\rangle)}/\sqrt{2}$, and we were also unsure if our experimental setup would be able to allow us to perform this experiment.

For that reason we performed a numerical study of how our four-level system behaves under Landau-Zener transitions, we tried to extract the necessary speed of the detuning pulse that the experimental setup must be able to generate, and lastly we investigated how this pulse should be shaped to provide a cleaner initial state.

## 5.1 Definition of the problem

Assuming that we know the 4x4 hamiltonian of the system, we will have 4 different levels that we can label as $\mathcal{H} = \{|\uparrow_L\rangle , |\downarrow_L\rangle , |\uparrow_R\rangle , |\uparrow_R\rangle\} = \{(\uparrow, 0), (\downarrow, 0), (0, \nearrow), (0, \swarrow)\}$. The levels can be essentially thought of as a Zeeman splitting of the two Bonding and Antibonding levels. In a recent article [16] a technique to populate only the lowest energy spin-state (the parallel spin state) in the two Bonding and Antibonding levels was proposed. We considered this as the starting point for our future research: supposing that we have a coherent, symmetric occupation of the

levels $|0\rangle = |\uparrow, 0\rangle$ and $|2\rangle = |0, \nearrow\rangle$, would it be possible to engineer a manipulation in order to produce a state with a coherent occupation of levels $|0\rangle = |\uparrow, 0\rangle$ and $|1\rangle = |\downarrow, 0\rangle$?

To describe the dynamics of the Spin-QuBit device we will take the hamiltonian proposed in the original article [28], which considers two detuned ($\epsilon$), tunnel coupled ($t$) quantum dots, each coupled with a different strength to a ferromagnetic lead $g_{/R}$. The two leads, therefore the induced magnetic field in the dots, are rotated by the angle $\theta$ between themselves. The effect of a quasi-collinear external magnetic field $B$, with $\phi$ angle representing the difference in the direction of the intrinsic magnetic field and the external magnetic field.

The hamiltonian $H$ of the Spin-QuBit system is given below:

$$\mathcal{H} = \begin{pmatrix} -\frac{\epsilon}{2} - \Delta_L - g_l B & 0 & t & 0 \\ 0 & -\frac{\epsilon}{2} + \Delta_L + g_l B & 0 & t \\ t & 0 & \frac{\epsilon}{2} - \Delta_R * \cos(\theta) - g_r B & \Delta_R * \sin(\theta) \\ 0 & t & \Delta_R * \sin(\theta) & \frac{\epsilon}{2} + \Delta_R * \cos(\theta) + g_r B \end{pmatrix} \tag{5.1}$$

This effective hamiltonian is expressed as a function of the macroscopic quantities:

- $\epsilon$, the detuning defined as usual as the difference in the chemical potential between the left and right dots. This is the only parameter upon which we have a fast control;
- $\Delta_L$ and $\Delta_R$, are the difference in energy between the two spin states in a single dot: $\Delta_{L/R} = \left|\uparrow_{L/R}\right\rangle - \left|\downarrow_{L/R}\right\rangle$. We took $\Delta_L = \Delta_R = 3\,GHz$;
- $g_L$ and $g_R$, coupling rates between the electron spin in the Left and Right dots and the external magnetic field. We considered $g_L = g_R = 1\,MHz$;
- $B$, an external, collinear magnetic field used to increase the spin effects in the system; We considered $B = 50\,mT$;
- $\theta = 45^o$, the angle between the two ferromagnetic leads;

The value for $t$ has been taken in agreement with the previous experiment. The other values have been taken from a similar experiment [29]. As $\epsilon$ is the only quantity that we can control at the ns-time precision needed for the Landau Zener transition, we will consider different time-dependent variations for $\epsilon(t)$, that we will call pulses.

Our idea is therefore that of writing the density matrix $\rho_0 = \rho(t = 0)$ corresponding to the initial state $|\psi_0\rangle = {}^{(|0\rangle + |2\rangle)}/\sqrt{2}$, and then evolve it according to it's equation of motion $\dot{\rho} = -\frac{i}{\hbar}[H(t), \rho]$. By numerically integrating this equation we can extract the density matrix at the final time $\rho(t_f)$, and compare it with the state that we wish to obtain $|\psi_0\rangle = {}^{(|0\rangle + |1\rangle)}/\sqrt{2}$.

In this process, the only time-dependent part of the hamiltonian is the diagonal detuning component $H(t) = H_0 + D(t)$, where $D(t) = \epsilon(t)\mathcal{D}iag(-1, -1, 1, 1)$. The detuning pulse is defined by the shape of $\epsilon(t)$, and we will test the evolution of the density matrix according to many different shapes of this function.

A constraint in the evolution might also be given by incoherent, dephasing and dissipative processes that can kill the quantum nature of the superposition of the

state (the off-diagonal terms in the density matrix), yielding a classical state. To account for those processes we will use the Lindbladian framework, where they are naturally described.

### 5.1.1 Lindlabian Framework

The Lindbladian framework is a mathematical technique that allows an easy treatment of incoherent processes, such as interactions with the environment, in a time-independent quantum system. This is possible because it relies on the density matrix, which is able to describe both classical and quantum mixtures of states.

Typically, we assume that the time-evolution of the density matrix for a general system is:

$$\dot{\rho} = -\frac{i}{\hbar}[H(t), \rho] \tag{5.2}$$

with few assumptions it can be shown that the above equation, in the time-independent case, can treat decoherence events if we add a simple term:

$$\dot{\rho} = -\frac{i}{\hbar}[H, \rho] + \sum_C \left( L(C)\rho + L(C^\dagger)\rho \right) \tag{5.3}$$

Where $L(C)$ is the Lindblad superoperator for the collapse operator $C$, defined as

$$L(C)\rho = C\rho C^\dagger - \frac{1}{2}\left( C^\dagger C\rho + \rho C^\dagger C \right) \tag{5.4}$$

Adding to the time evolution a Lindblad Superoperator for a non-hermitian operator C, such as $C = a$ or $C = a^\dagger$ will make the evolution non unitary, introducing dissipation and decoherence. To write the time Partial Differential Equation 5.3 for the evolution of $\rho$ in the Lindblad Framework, after considering the unitary term arising from the hamiltonian, one identifies all possible incoherent processes and assigns to those a rate.

#### Example

To make an example, we will consider the Hamiltonian for a 2 level (B/AB) Double Quantum Dot with tunneling between the two levels:

$$H = \frac{\Omega}{2}\sigma_z + t\sigma_x \tag{5.5}$$

This hamiltonian describes a system with one electron between two dots (L and R) and with a tunneling probability between the two. As the two atomic orbitals hybridize, we can also think the system as formed by two molecular orbitals B/AB in the diagonal basis.

Incoherent processes can be distinguished in two categories: environment-based processes that change the occupation number of a level, like an electron jumping from B(AB) to AB(B) as a consequence of the absorption of some thermal energy, or coherence-based processes, like charge noise, that do not change the occupation number but change the off-diagonal terms of the density matrix.

We can therefore list the following processes, along with their operators:

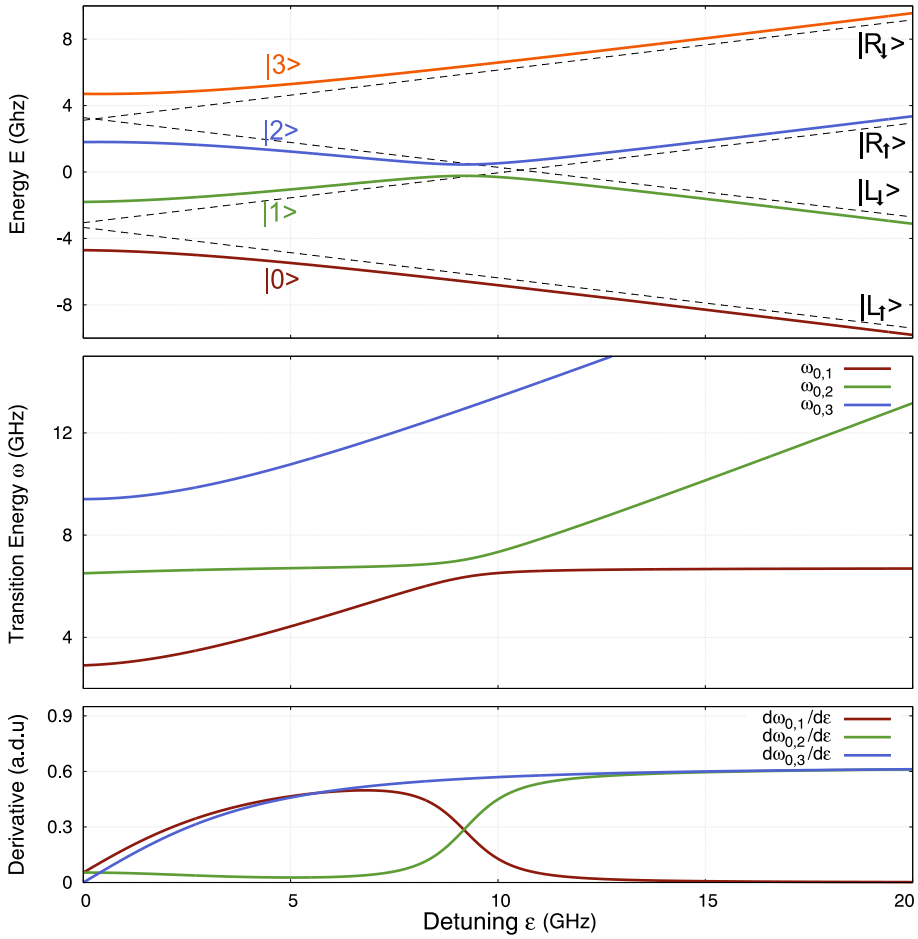


Figure 5.1: **(a):** Numerical diagonalization of the hamiltonian reported in the previous section, for the values reported. The four colored lines are the diagonal eigenstates, the dashed black lines are the elements of the canonical basis (which we refer to as asymptotic basis). **(b):** Transition energies between level $|0\rangle$ and $|i\rangle$ for $i = 1, 2, 3$, as a function of detuning $\epsilon$. **(c):** $\epsilon$ derivative of the transition energy. Notice that for $\omega_{0,1}$, the derivative goes to 0 at high $\epsilon$, meaning that charge noise is suppressed.

---

- Excitation of the charge QuBit from Bonding to Antibonding due to interaction with the leads and environment; process represented by $\sigma_+$ and rate $\gamma_{charge,B\to AB}$;
- De-excitation the the charge QuBit from Antibonding to bonding; process represented by $\sigma_-$ and rate $\gamma^{\star}_{charge,AB\to B}$;
- Decoherence Process (charge noise) acting not on the population of the two levels, but only on the coherence between the two, reducing the entanglement; represented by operator $\begin{pmatrix} 1 & 0 \\ 0 & 0 \end{pmatrix}$ for rate $\gamma_{2,B}$ and $\begin{pmatrix} 0 & 0 \\ 0 & 1 \end{pmatrix}$ for rate $\gamma_{2,AB}$.

When one takes one writes the superoperator of the operators listed above through formula 5.4 one will notice that all but the last one act on the density matrix elements by changing the diagonal elements, therefore the population of those levels, and the off-diagonal elements by a proportional quantity. The last kind of noise, instead, leave untouched the population and only changes the off diagonal terms. The effect of this is that the probability of the system to be in the B or AB level is the same as the original level, but the noise drives the system to a classical state where the coherent oscillation from one state to the other are no longer measurable.

#### Implementation of charge noise

In principle we should consider all sources of noise in our system, but in this analysis we decided to consider only charge noise as all the others have lower rates than charge noise. To model charge noise we used the same argument presented in section 1.3.4: in a two level system we identify the charge noise rate $\gamma_{charge}$ to be proportional through some constant $c$ to the first derivative of the transition energy $\Omega(\epsilon)$ between the two levels, therefore $\gamma_{charge} = c \cdot \frac{\partial \Omega(\epsilon)}{\partial \epsilon}$. For our four level system we use the same argument: we have four levels with eigenenergies $E_i(\epsilon)$ (fig. 5.1(a) ) where $i = 0..3$ and therefore we identify six different transition energies $\omega_{i,j} = (E_i(\epsilon) - E_j(\epsilon))$ (fig. 5.1(b) contains $\omega_{0,i}$). Since we expect the charge noise acting on each off diagonal element of the $4 \times 4$ density matrix $\rho_{i,j}$ $(i \neq j)$ to be proportional to the derivative of the transition rate between levels i and j (fig. 5.1(c)), we define the charge-noise operator acting on levels i and j as:

$$\tilde{C}_{i,j}(\epsilon) = c \left( \frac{\partial (E_i - E_j)(\epsilon)}{\partial \epsilon} \right) \cdot (|i\rangle \langle j| + |j\rangle \langle i|) \tag{5.6}$$

And then, summing across all possible rates we obtain the total charge noise operator C:

$$\tilde{C}_{tot}(\epsilon) = \sum_{(i,j) \neq (i,i)} \tilde{C}_{i,j}(\epsilon) \tag{5.7}$$

Then, starting from this operator we compute the Linbladian superoperator $L(C)$ that we will use for the evolution of the system.

It is important to note that this operator depends on the detuning $\epsilon$, and therefore during a sweep in $\epsilon$ it will change. This is exactly what we wanted, as we expect the charge noise between the levels 0 and 1 to go to 0 as we approach large detuning.

### 5.1.2 Algorithm

Before presenting the algorithm used to perform the integration, let us discuss a small complication in performing the computation. As we have already said, we will be evolving the system starting from the initial density matrix $\rho_0$ according to the differential equation 5.3 (rewritten in a more convenient form below

$$\dot{\rho} = -\frac{i}{\hbar}[H, \rho] + c\mathcal{L}_{charge} \tag{5.8}$$

$$\mathcal{L}_{charge} = \sum_{C} \left( L(C_{tot})\rho + L(C_{tot}^{\dagger})\rho \right) \tag{5.9}$$

If the charge noise was zero ($c = 0$) we could perform the numerical computation of this system of differential equations in the same basis as the one in which the hamiltonian is written (which I'll refer to as asymptotic basis). Then to obtain the occupation numbers of the eigenstates $|i\rangle$, once we have obtained numerically $\rho(t_i)$ at every interval i, we could convert $\rho(t_i)$ from the asymptotic basis to the diagonal basis with the change of basis $\tilde{\rho}(t_i) = P(\epsilon(t_i))\rho(t_i)P^{\dagger}(\epsilon(t_i))$, where $P(\epsilon(t_i))$ is the matrix that diagonalizes H at time $(\epsilon(t_i))$, defined as $P(\epsilon(t_i)) \mid diag(\lambda_i((\epsilon(t_i)))) = D((\epsilon(t_i))HD^{\dagger}(\epsilon(t_i))$.

We have expressed the charge noise operator in the diagonal basis, therefore if we want to implement in the previous procedure the charge noise, we will have to convert it to the asymptotic basis. But since the base-change matrix $D$ is time-dependent, we will have to do it at each iteration. Therefore obtaining

$$C_{tot}(\epsilon(t_i)) = \left(DC_{tot}D^{\dagger}\right)(\epsilon(t_i)) \tag{5.10}$$

We have shown that to write all the operators in the same basis we need to compute the change of coordinate matrix $D$ that diagonalizes $H$ for every $\epsilon$. As $H$ is a 4x4 hermitian matrix $D$ is a real matrix and always exists, homwether, obtaining an analytical formula expression for $D$ that holds $\forall\epsilon$ is, as far as we know, impossible, therefore we resorted to numerical diagonalization of $H$ to obtain $D$.

At every time-step, after computing the value of $\epsilon$ given the shape of the pulse, we use the above procedure to obtain $C_{tot}(t)$ and therefore $L(C_{tot})(t)$. $H(t)$ is easily obtained from it's analytical expression, where we only need to plug the right value of $\epsilon$. After we have computed the two operators, we cast the differential equation as follows:

$$\dot{\rho}_t = -\frac{i}{\hbar}[H_t, \rho_t] + L(C_{tot,t}) = \mathcal{L}_t\rho(t) \tag{5.11}$$

where $\mathcal{L}_t$ is the 4x4 matrix holding all the needed information to perform one time-step. At this point computing $\rho_{t+\Delta t}$ is equivalent to solving the above differential equation. To do so, we used a custom-written Runge-Kutta (RK) algorithm of $4^{th}$ order with an adaptive time-step (often addressed as RK 4.5 algorithm). To compute the time-step, at each iteration we compute $\rho_{t+\Delta t}$ both using a single step of RK(4) and using a single step of RK(5), then the two results are confronted. If the two differ by more than a certain threshold $r$, the algorithm halves $\Delta t$ and repeat the same procedure until the difference between the two algorithms is low enough. After each time-step, $\mathcal{L}_t$ is recomputed for the new value of $t$ and the procedure is repeated.

## 5.2 Behavior check

After having written the code used to perform the numerical time-integration for the system, we validated it by checking the time-evolution in some cases where we knew what features to expect.

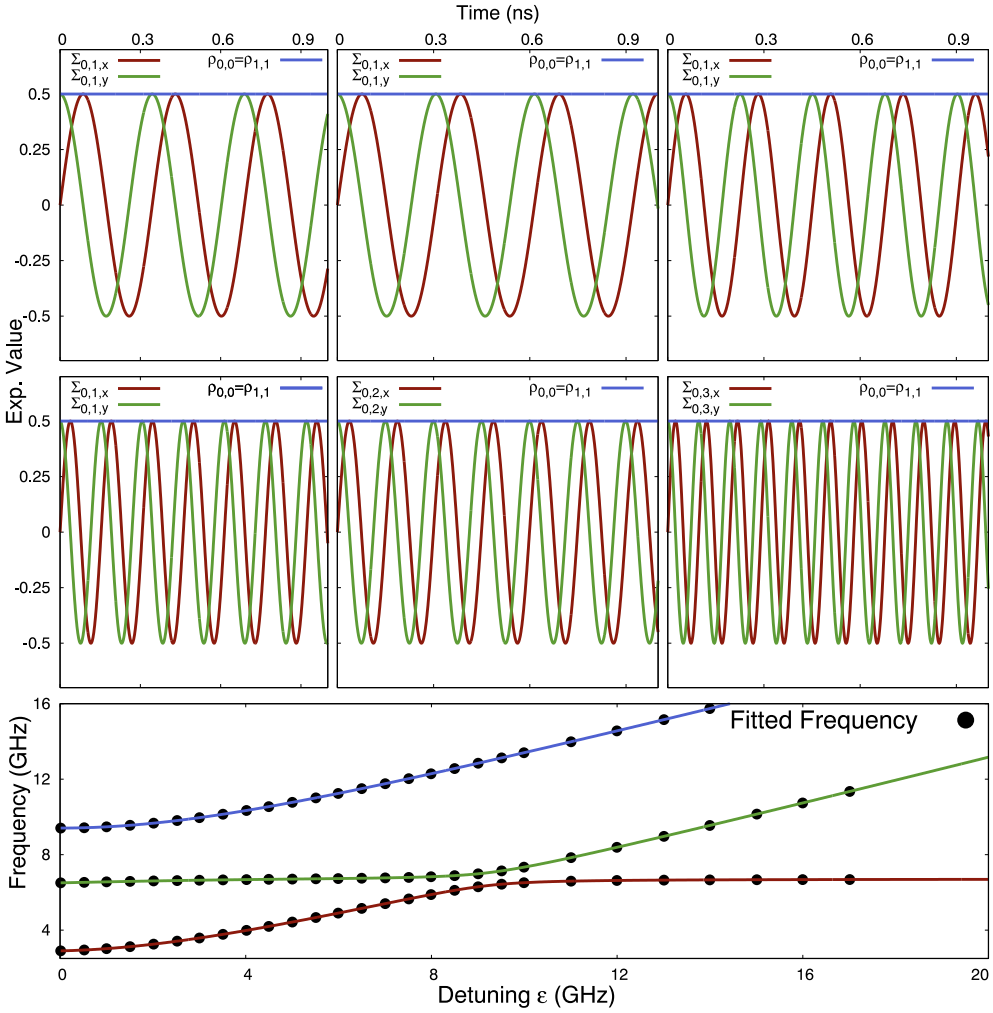


Figure 5.2: Data generated through our algorithm, for the case described in this section. In the 6 smaller panels the time evolution for $t \in [0, 1]$ of the $\Sigma_{i,j,x/y}$ operators is shown (oscillating), along with the populations of the non-zero levels (constant), for different i, j and $\epsilon$. The first four panels have starting condition $|\psi\rangle = \frac{1}{\sqrt{2}}(|0\rangle + |1\rangle)$ and $\epsilon = 0$, 2, 4, 10, the fifth has $|\psi\rangle = \frac{1}{\sqrt{2}}(|0\rangle + |2\rangle)$ and $\epsilon = 4$ while the last has $|\psi\rangle = \frac{1}{\sqrt{2}}(|0\rangle + |3\rangle)$ and $\epsilon = 4$. The lower, wide panel reports as black dots the frequencies obtained by fitting the above panels through sin and cos (and additional data that is not reported). Each smaller panel, corresponding to one simulation, yield one black dot. The solid lines superimposed are the transition energies for our model, which (at least partially) validate our code.

### 5.2.1 Quantum Oscillation's frequency

A common feature of all N-levels quantum systems are quantum oscillations, which can more easily be understood qualitatively in the case of a Two Level system. The state of the Two level system can be thought of as a vector in the Bloch Sphere. If the initial state of the system is on the equator, $|\psi\rangle = \frac{1}{\sqrt{2}}(|\uparrow\rangle + |\downarrow\rangle)$ and let it

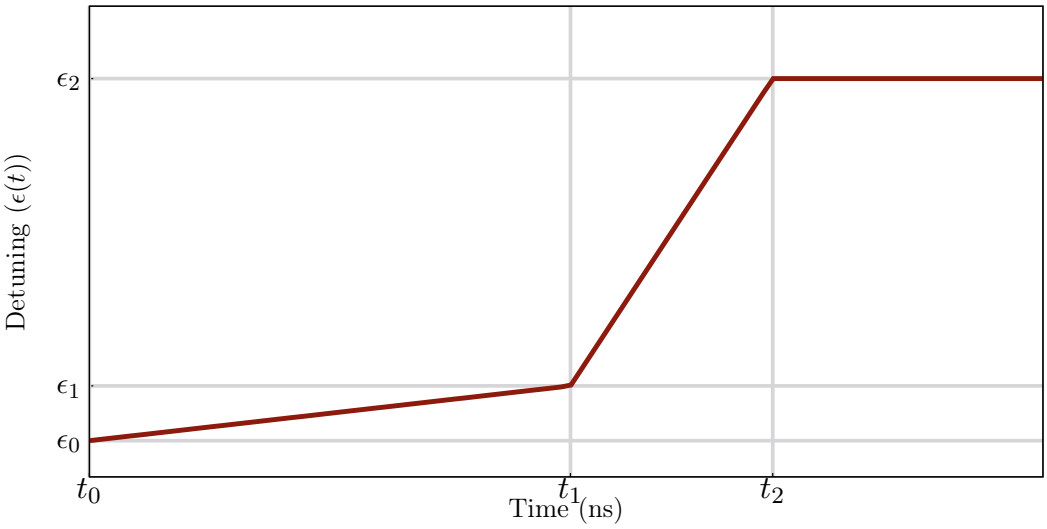


Figure 5.3: Sample pulse with the values that define it: $t_0$ is the start time, $t_2$ the end time and $t_1$ the crossover time, at which it switches from slow ramp to fast ramp.

evolve in absence of decoherence, we expect the diagonal terms $\rho_{0,0}$ and $\rho_{1,1}$ of the density matrix (the populations of the two levels) to remain constant in time, while the 2 off diagonal terms $\rho_{0,1} = \rho^{\star}_{1,0}$ will have a different behavior. In particular, the real and imaginary part will oscillate with a frequency $\omega$ equal to the transition energy between the two levels. This is a consequence of the fact that $\langle\sigma_x\rangle = \mathcal{R}e(\rho_{0,1})$ or $\langle\sigma_y\rangle = \mathcal{I}m(\rho_{0,1})$.

In the case of $N > 2$ this property is still valid, though the expressions become much more complex. To simplify them and obtain an easy-to-perform test on our numerical integrator, we again consider only a state that is an equal mixture of two eigenstates $i$, $j$ among the N available: $|\psi\rangle = \frac{1}{\sqrt{2}}(|i\rangle + |j\rangle)$. In this case, oscillations analogous to the one described in the previous chapter can be observed by defining operators $\Sigma_{x,y}$ that generalize $\sigma_{x,y}$

$$\Sigma_{i,j,x} = \begin{array}{c} \\ i \\ \\ j \\ \\ \end{array} \begin{array}{c} \begin{array}{cccc} & i & .. & j \end{array} \\ \begin{pmatrix} 0 & & & & \\ & 0 & & 1 & \\ & & 0 & & \\ & 1 & & 0 & \\ & & & & 0 \end{pmatrix} \end{array} \qquad \Sigma_{i,j,y} = \begin{array}{c} \\ i \\ \\ j \\ \\ \end{array} \begin{array}{c} \begin{array}{cccc} & i & .. & j \end{array} \\ \begin{pmatrix} 0 & & & & \\ & 0 & & -i & \\ & & 0 & & \\ & i & & 0 & \\ & & & & 0 \end{pmatrix} \end{array} \tag{5.12}$$

Those two operators neglect all other levels except for the two considered, i and j, and they are evaluated as their expectation value equals the real (x) or imaginary (y) part of the coherence $\rho_{i,j}$.

As $\langle \sigma_{x/y} \rangle$ are known to oscillated with the Bloch frequency of the two level system $\Omega$, we expect $\langle \Sigma i, j, x/y \rangle$ to oscillate at the transition frequency $\omega_{i,j}$, while the sum of their modulus square, $\langle \Sigma_{i,j,x} \rangle^2 + \langle \Sigma_{i,j,y} \rangle^2$ will stay constant if we consider no charge noise ($c = 0$). In the 6 small panels of fig. 5.2 evolution of $\Sigma_{0,i,x/y}$ for various values of $\epsilon$ are presented. Initial condition where always $|\psi\rangle = \frac{1}{\sqrt{2}}(|0\rangle + |i\rangle)$. We also considered other transitions, but do not report the plot. All those test evolution where fitted through a sin/cos function and the extracted frequency is reported as black dots in the lower panel of fig. 5.2. The reader can see that the black dots reproduce perfectly the curves of the transition energies $\omega_{i,j}$ of fig. 5.1(b), which tells us that our numerical integration is, at least in this case, giving right results.

## 5.3 Landau Zener Pulse

After having made sure that our numerical procedure plays well with our system, we applied it to our system of interest. As we had said earlier, we are interested in finding the shape of a detuning pulse, $\epsilon(t)$, that can transfer the coherence $\rho_{0,2}$ to $\rho_{0,1}$ and the population of the level 2, $\rho_{2,2}$ to level 1, $\rho_{1,1}$. It is generally known that the best shapes to do so, are collections of slow and fast ramps [30], therefore we started our analysis by using a first slow (quasi-adiabatic) pulse, and then perform a fast ramp. A sample pulse is presented in fig. 5.3; this *double ramp* pulse can be identified by it's 3 pairs of values $(t_i, \epsilon_i)$ for $i = 0, 1, 2$. We put $t_0 = 0$ for simplicity, and for the reasons presented before we are interested in pulses starting from zero detuning, therefore $\epsilon_0 = 0$. The end value of the pulse, $\epsilon_2$, must be sufficiently high so that charge noise for the 0-1 levels is small, but small enough so that we stay inside a single coulomb diamond like the ones we measured in the previous chapter. We chose $\epsilon_2 = 10\,GHz$, as it satisfies both conditions: $\frac{\partial \omega_{0,1}}{\partial \epsilon}(\epsilon = 10) \approx 0.1$, and $\epsilon = 10\,Ghz \rightarrow \hbar 10\,Ghz \simeq 6\mu eV$ which is comparable to the charging energy $U$ of our charge QuBit. Therefore we have left only 3 free parameters on the pulse: $t_1$, $\epsilon_1$ and $t_2$.

Because we want the first slow ramp to be adiabatic, as long as the ramp is slow enough it's duration $\Delta t_{slow} = t_1 - t_0$ is not important, and only the end value, $\epsilon_1$, will determine the evolution of the system [31]. For that reason, we decide to also fix $m_1 = \frac{\epsilon_1 - \epsilon_0}{t_1 - t_0}$ and only study how variations of $\epsilon_1$ and $m_2 = \frac{\epsilon_2 - \epsilon_1}{t_2 - t_1}$ affect the result of the pulse. Essentially, we will perform the same simulation for different values of those two free parameters, and see which ones yield the best transfer of coherence.

Two sample simulations are presented in fig. 5.4; respectively, on the left column a badly-performing pulse is shown, while on the right column a good-performing pulse is reported. In the lower panels we show the pulse, composed of the two different ramps. In the top panels we presented the evolution of the coherences $\rho_{0,i} = \langle \Sigma_{0,i,x} \rangle^2 + \langle \Sigma_{0,i,y} \rangle^2$ for $i = 1, 2, 3$. The top green line shows $\rho_{0,2}$ which starts at the maximum value 0.5 because the initial vector is the coherent superposition $|\psi\rangle = \frac{1}{\sqrt{2}}(|0\rangle + |2\rangle)$, while the lower red line for $\rho_{0,1}$ is equal to 0. The coherences are left untouched by the slow pulse, while the fast pulse transfer some value from $\rho_{0,2}$ to $\rho_{0,1}$. You can see that for the good pulse (right) after the fast ramp $\rho_{0,2} \approx 0$ and $\rho_{0,1}$ approaches the maximum value, while for the bad pulse they simply exchanged

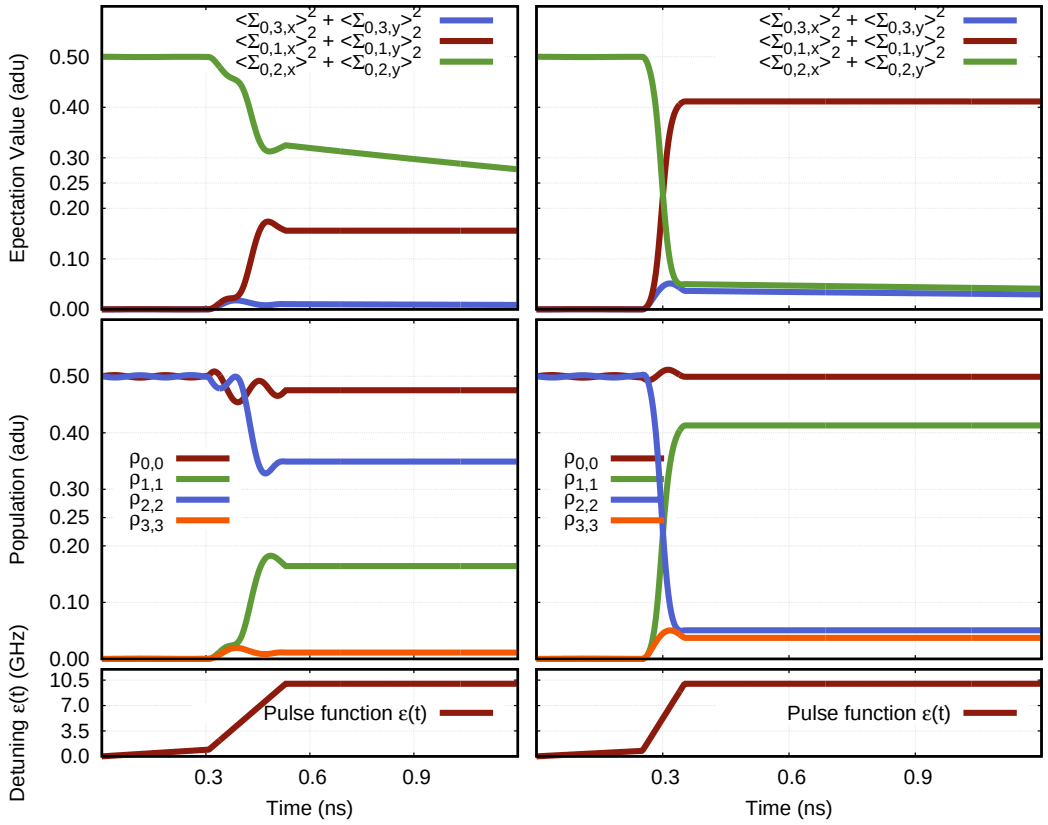


Figure 5.4: Plot of certain elements of the density matrix of a state as a function of time, with starting state $|\psi\rangle = \frac{1}{\sqrt{2}}(|0\rangle + |2\rangle)$. The values are obtained numerically by applying a pulse on the system. The two columns correspond to two different pulses (visible on the bottom line). On the top line the coherences are reported, while on the middle line the populations are reported. A transfer of population and coherence from level 2 to level 1 is visible.

a fraction of the coherence, and $\rho_{0,2} > \rho_{0,1}$. After the fast pulse we also see $\rho_{0,2}$ decreasing as a consequence of charge noise. The effect is less visible on the *good* simulation because in this case most of the population was transferred to the 0-1 levels which are insensitive to this noise.

In the central panels we reported the populations (diagonal elements of the density matrix) of the 4 levels. As expected, we see that charge noise does not influence the population of $\rho_{2,2}$ but only it's coherence. Moreover, we see that with the good pulse the transfer of populations is much better than with the other pulse.

To judge what parameters yield the best evolution we ran this evolution[1] for

[1]The code is mostly written in Python with a Cython wrapper to call C-functions for the most performance-heavy parts. A single simulation runs as a single thread and cannot be parallelized, and takes on average 10 seconds per nanosecond of simulated time, depending on how fast the pulse is (if the ramp is extremely fast, the adaptive algorithm will keep decreasing the time-step, thus increasing computation time). To run the $70^2$ simulations needed to produce fig. 5.5, we

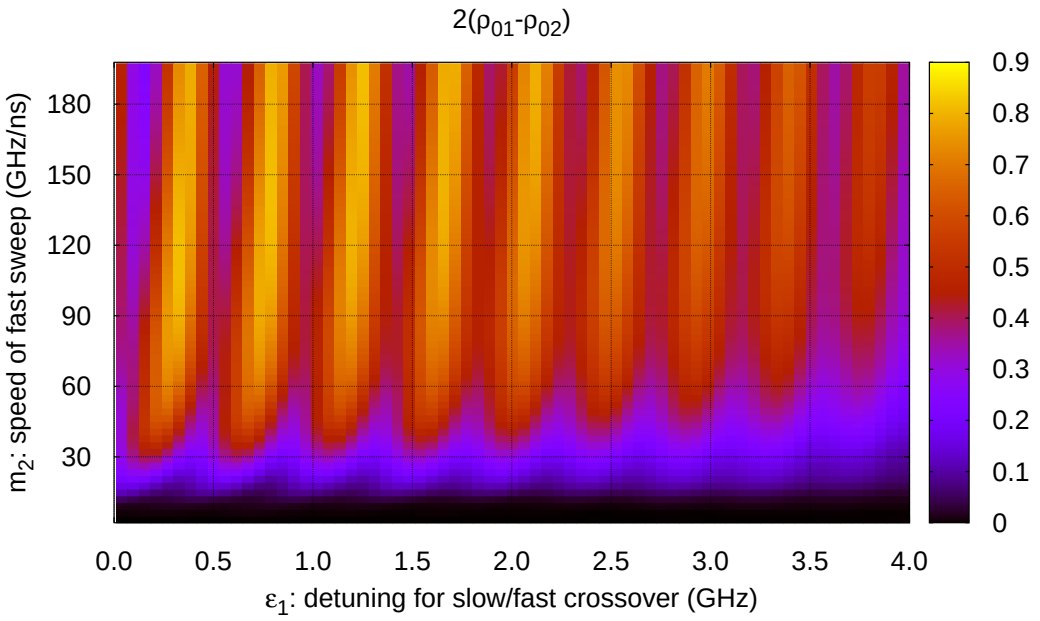


Figure 5.5: Colormap for the function $2(\rho_{01} - \rho_{02})$. A bright color represents a good transfer of coherence, while a dark color represents a bad transfer. The two axis are respectively $\epsilon_1$, the detuning value at which we cross over to a fast ramp ending the slow ramp, and $m_2$, the speed of the fast sweep.

various values of $\epsilon_1$ and $m_2$. In fig. 5.5 we present only the relative coherence transfer $2(\rho_{0,1} - \rho_{0,2}$ at the end of the pulse sequence. We immediately notice that to have a coherence transfer of at least 80% we would need to change the detuning on the device at a speed of approximately $m_2 \approx 100\,{}^{GHz}/_{ns}$, which corresponds to approximately ${}^{50\mu eV}/_{ns}$. With our current setup we can achieve a maximum of some ${}^{\mu eV}/_{ns}$, therefore to perform the manipulation described in this numerical study we would need to upgrade our experimental setup.

Another interesting feature that we notice from this plot is that one cannot simply evolve use on the system the fastest possible pulse and hope to achieve a good coherence transfer, but one must also *sync* to the right value of $\epsilon_1$. Varying $\epsilon_1$ we see that the coherence transfer quality decreases and increases again with a period of approximately $0.45\,Ghz$. A very similar result was recently published by H. Ribeiro and J. Petta [33], who obtained experimentally a similar pattern when looking at the Landau Zener coherence transfer in a Superconducting QuBit. They explain their results by noting that their fast pulse must be *synced* to a precise phase of the Bloch (or Quantum) Oscillations[2] of the Coherence.

modified the code to use Distributed Computing: a master node distributes the simulation code and some precomputed data to a cluster of 15 slaves, which report back only the result of the simulation. Inter-Node communication was implemented through the Dispy Library [32]. This allowed to reduce the computation time by a factor of 500 (15 nodes times 32 threads per node).

[2]The very same oscillations were used to check if our code was performing good.

We think that a further study of this interesting phenomena is going to yield interesting results, also because we could compare calculations for the Spin-Qubit with experimental data from the Superconducting QuBit community (the paper by Petta and Ribeiro). Moreover, progress in this numerical line of research is going to benefit from the code that was written during this thesis, allowing us to focus on probing the system instead of worrying about the numerical details and checking if the numerical procedure is correct.

# Chapter 6

# Conclusions and Perspectives

In this thesis we presented a QuBit Architecture with the desirable properties of a long coherence time and of implementing single-QuBit gates in the QuBit itself. This architecture has been physically realized in a Ferromagnetic Double Quantum Dot hosted in a Single Wall Carbon Nanotube, and studied through a coupled Microwave cavity.

The fabrication process for this device has proved complex, and several months have been spent during this work trying to define a better recipe to be used in the clean room. The first problem that we confronted was the extremely low yield ratio of the stamping process used to transfer Carbon Nanotubes from their Quartz growth substrate to the Silicium Chip hosting the samples. By refining the procedure used in the clean room I have been able to improve the successful transfer rate from approximately 20% to 70% (section 3.1.3). Even if I was able to improve our stamping rate, the percentage of transferred but damaged nanotubes remained constant at about 70%, which is an issue considering that we can detect damaged nanotubes only after cooling them down to $T \approx 2\,K$, resulting in a very time-consuming trial and error process. Precise mechanical manipulation that does not introduce defects is a very ambitious goal sought after not only by academic groups, but also by technology giants such as IBM as Intel that see Carbon Nanotubes as a candidate in replacing Silicium in the Semiconductor Industry. For that reason our group started to design a custom made, low temperature (Liquid He) and high precision (Piezoelectric actuators) transfer setup to reduce strain induced on the nanotubes during the stamping process. We think that this setup will improve the stamping rate while at the same time greatly reduced the number of damaged nanotubes.

During those 7 months I also contributed to the physical design of the QuBit device by engineering a coupling capacitor to mix an AC and a DC signal and feed it asymmetrically to one Dot of a Double Quantum Dot. The design was validated using a damaged sample that was fabricated in the clean room and we were able to extract a ratio in the coupling strength between the dot and the two components of the signal, DC and AC, finding that AC signals couple 500 times less to the charge in the DQD than DC signals (section 4.2.1). This result will be used in the following years to refine the design of the coupling capacitor itself.

Of the two working samples that we were able to fabricate in the clean room, one was damaged, and was used to perform the coupling capacitor calibration, while

the other was working and we were able to extract interesting physics from it (section 4.1.2). The design of the asymmetric coupling between the cavity and the charge degree of freedom of a Double Quantum Dot was validated by comparing results of this device with a previously-fabricated, symmetrically coupled device.

We began the study of those devices by probing the charge degree of freedom and fitting experimental data through a simple 4-level master equation with only 2 free parameters (section 2.3.2). The model reproduced features of our signal and allowed us to extract order of magnitudes for some microscopic properties of the device. We found that our device has low charge coherence time $\Gamma_\phi \simeq GHz$, an inter-dot tunneling rate close to the microwave cavity resonant frequency $2t \simeq 6.4\,GHz$ and a charge-photon coupling rate of $g \simeq 50\,MHz$. While charge coherence is not particularly good for this class of devices, will be irrelevant when operating the device as a Spin-QuBit. The charge-photon coupling rate confirms that the two are strongly coupled, validating the design of a superconducting electrode evaporated over an insulating layer on top of the Nanotube. We reached strong coupling between the photons in the superconducting cavity and the electrons in the nanotube, promising interesting results in double quantum dot physics unattainable on conventional transport setups that cannot perform Quantum Non Destructive measurements.

Towards the end of my time in the lab we also attempted to perform a spectroscopic measurement of the excited states of the QuBit, but had no results. We attributed the lack of results to the particular way that the gates are coupled to the Left and Right dots in our sample: the gate that is used to send fast AC pulses to the nanotube, necessary to perform the spectroscopy, is weakly coupled to the charge degree of freedom of this sample, hindering our attempts exposed in (section 4.2.2.

I also have developed a numerical code able to evolve in time the state of our device keeping track of charge noise, granted that it's microscopic parameters ($g$, $t$ and the others) are known. We used this software to confirm if it's possible to transform the state $|\psi\rangle = \frac{1}{\sqrt{2}}(|0\rangle + |2\rangle)$ to $|\psi\rangle = \frac{1}{\sqrt{2}}(|0\rangle + |2\rangle)$ through a fast pulse (chapter 5). A manipulation similar to the one described I have studied numerically will be needed to transform the long-coherence-time Spin State to a measurable Charge State and viceversa. The code also allowed us to give an estimate of the minimum time resolution needed to perform such an experiment, and the shape of the pulses to use.

As we discussed in chapter 4, collecting the data necessary for high resolution maps is a process that takes on average 2 hours, rendering our measurements prone to drifts in the potentials used to control the QuBit. Those drifts play a minor role when measuring the steady state configuration of the device (a measurement that takes about 30 minutes), but they may be a considerable issue when probing the excited states of the system or taking longer scans. Such big sources of uncertainty acting on the QuBit as those hard-to-predict drifts, coupled together with rapidly varying fields induced by the AC signals that we used for spectroscopy, prevented us from observing a clear signature of the excited states.

To overcome the problem of long measure times we plan on implementing a technique described in a recent article by J. Petta that reduces hour-long measurements to $1/30^{th}$ of a second, allowing them to control in real time their circuit [34]. The technique is based on amplifying the output signal of the microwave cavity through a Quantum Limit Amplifier, a device with an extremely high Signal to Noise Ratio.

Lowering by 5 orders of magnitude the time required for a measurement not only permits us to neglect drifts and random spurious modes in the measures, but would also allow us a much higher resolution when needed. Unfortunately, fabrication of a Quantum Limited Amplifier has proven challenging until recently, as they must be cooled to mK temperatures and shielded from magnetic fields, requiring a much bigger Cryostat than the one currently at our disposal. For that reason, the project to which we collaborated has now been put on hold, while our group tries to build a suitable Quantum Limit Amplifier and we wait for the funding necessary for a new fridge.

# Appendix A

# Fabrication

In this section fabrication of the samples is depicted. Samples are prepared

### A.0.1 Chip Preparation

#### Substrate cleaning

Samples are fabricated starting from a 1cm X 1cm Silicium chip 0.5 mm deep, where the top layer has been oxidized, resulting in a layer 500 $\mu m$ deep of $SiO_2$.

Those chips are supplied by a general vendor and come with a protective resist layer that must be removed to allow the process to start. To remove this layer samples are exposed to the following standard recipe:

RECIPE:

- chip in a beaker with acetone ($C_3H_6O$) and put in an ultrasonic cleaner for 5 minutes. This is done 2 times, changing the solution.
- chip in a beaker with Isopropanol ($CH_3CH(OH)CH_3$) and put in an ultrasonic cleaner for 5 minutes.
- Dry with Nitrogen gun
- check under optical microscope (20X, 50X). If there are resist residues remove mechanically with clean-room paper and/or cotton swabs imbued with acetone. Repeat until the chip is clean.
- chip in a beaker with Isopropanol ($CH_3CH(OH)CH_3$) and put in an ultrasonic cleaner for 5 minutes.
- Dry with Nitrogen gun

Usually in this step only 1 chip out of 4 requires mechanical cleaning.

### A.0.2 Alignment Marks

The first step in the fabrication is the deposition of Gold crosses used later for alignment, and gold precontacts used to contact DC and AC lines of different thicknesses. Those gold features are fabricated by

Clean samples are spin coated with electronic resist (PMMA). The sample is secured on the spin coater and then two drops of PMMA are deposited on it with a plastic pipette. Spin coating is done at 4000RPM for 30 seconds, with an acceleration of 4000RPM/s. The resist is then baked for 15' at 165ř on a hot plate.

Spin coated samples are then loaded in an Electronic Microscope for the lithography stage. Grounding of the chip is performed by scratching a small area of resist on one side of the sample.

Samples are then unloaded and resist get developed by stirring them in a developer solution of 1:3 MIBK:IPA for 20 seconds. Immediately after developer gets removed from the samples to avoid overdeveloping by stirring them for 1 minute in a IPA solution.

After developing samples are loaded in an evaporator, where we evaporate a 80 nm thick layer. Evaporation is performed with an electron gun pointing at gold pellets, set at 10keV with a current of 50 pA.

Lift off is performed by leaving samples in Acetone and/or AZ100 remover for 30 minutes. After 30 minutes a pipette and/or a siring is used to flow acetone on top of the sample to finish the liftoff.

After the Liftoff the sample is cleaned again following the same recipe used to clean new chips.

### Niobium Evaporation

The following step consists in evaporating a 250 nm thick layer of Nb over the whole chip. The chip was loaded in a *Plassys MEB450SUHV* Ultra High Vacuum Evaporator with a loading chamber, left in the loading chamber for approximately 1 hour, until we reach a pressure of $10^{-6}$ mbar. Subsequently, to obtain an highly pure deposition we cooled down the Evaporation chamber by flowing Liquid Nitrogen in a dedicated interstice of the vacuum chamber. The evaporation is performed when the inner vessel is at approximately -30řC. The electron gun is set at 10keV, 300 pA. The layer of Nb we evaporate is 250 nm thick.

### Optical lithography

The following step consists in etching the main patterns (gates, pads, resonator...) on the Nb substrate.

First, the sample gets spin-coated with Optical Resist. We used *MicroChem AZ5214E*. It is usually stored in a fridge at 3řC, and it is therefore very viscous. Therefore we found ideal to let the resist inside a pipette warm up at 23řC for 10 minutes to obtain ideal viscosity before performing the spin coating.

Since the resist is very viscous, we found that a thicker layer of AZ5214E remains around the edges after spin coating. To counter this issue we decided to deposit only one drop of resist on each chip, and cover the whole chip with this single drop by tilting it. As soon as the whole chip was covered, it was spin coated. Spin coating settings are the same as before, namely: 4000RPM, 4000RPM/s, 30s.

Optical resist was baked on an hot plate at 115řC for 1.30'

The sample is then loaded on a *Suss Microtech MJB4* Optical Lithography Machine along with a Chromium Mask. Alignment is performed by eye using the

alignment crosses and (mainly) by aligning the mask lines with the gold precontacts. Settings for the lithography are the following: Hard Contact (5"), Exposition (8").

After Lithography the resist is developed by manually stirring the sample in AZ-MIF developer for 20", and residues of developer are then washed away by stirring the developed sample in de-ionized $H_2O$ for 2'.

#### Nb Etching

When we have a perfect negative mask, we place our samples (usually in sets of four) in a Reactive Ion Etching Machine (*Corial 200R*), and we perform Dry Nb etching through a RIE process defined by the vendor. To monitor the etching we shine a laser on an area of the Nb that we want to etch, and through a dedicated detector we monitor the reflected light. During the etching process the reflected intensity will gradually decrease, until a minimum hit when the Nb is fully etched and the $SiO_2$ is exposed. After the minimum is reached we wait 10" until stopping the process by shutting down the plasma and flowing Ar in the RIE chamber.

After etching we remove the Resist mask with the following cleaning recipe:

1 5' Acetone at room temperature

2 10' Acetone at 50ř

3 60' AZ Remover-100 at 50ř

4 mechanical cleaning with folded clean room paper dipped in Acetone

5 Rinse in IPA

6 5' $O_2$ Stripping

At this point the samples are usually free of any resist (that appear as dark spots in an optical microscope).

## A.1 CNT transfer

The following step consists in transferring Carbon Nanotubes from the growth substrate to our samples. The growth process, explained in section 3.1.3, results in 1mmX1mm quartz chips with 4 sets of nanopillars 100$\mu m$ tall, between which we have grown carbon nanotubes. We call the transfer process *stamping*, and it is explained in section 3.1.3.

#### CNT Localization

After stamping the nanotubes we have to determine with high precision their coordinates on the chip. We call this procedure *localization*. CNT Localization is done immediately after the stamping process by placing them in the Electron Beam Microscope. We operate with an acceleration voltage of 2 kV. First we focus the microscope at a resolution of 5 nm by looking at the small crosses next to the stamping area, to avoid exposing the CNT to electrons, then we use the small gold crosses (see fig. 3.2(b)) to align precisely the position, and lastly we take a bunch of

800x800 nm pictures around the stamping spot. We repeat this procedure (including the refocusing and alignment process) for every one of the 4 stamping areas on every chip.

**Fine Lithography and evaporations**

After localization we use the images gathered to draw the contacting electrodes in a program (E-Line), that will then be patterned through Electron Beam Lithography.

After localization we cover the samples with PMMA (Same recipe as before), and we bake it. Then we perform an Electron Beam Lithography stage where we only pattern the 2 ferromagnetic Source/Drain electrodes, and not the gates. We aim at a width of the traces of approximately 50 nm on top of the nanotube. After the lithography we develop the PMMA with the same recipe as before (20 seconds in a 1:3 MIBK:IPA solution) and then we place the chip in the evaporator. We let it rest for at least 10 hours in the Load-Lock chamber at $10^{-5}$ mbar so that some of the surface PMMA, weakly coupled to the rest, can detach from the surface. Lastly we perform the evaporation of PdNi (10 nm thick) and a protective Ni layer (50 nm). We end this lithography by lifting in acetone.

After the Source/drain lithography we perform another lithography, following exactly the same procedure, to evaporate the superconducting gates. The only differences are in the width of the traces (100 nm), and the materials evaporated. We first evaporate three layers of $NiO_2$ 8 nm thick, by evaporating it and then oxidising (we fill the evaporator load lock with pure $O_2$ at a pressure of 1 mbar). After we have evaporated the three layers of Oxide, we evaporate the Al gate (thickness 70 nm) and then a protective Ni layer (30 nm). Lastly we lift.

After this last evaporation the sample is ready. We just need to split the chips in the two halves, containing each 2 CNTs and 1 cavity. Then we glue the half-chips in a custom made PCB board that we use to connect them through a microp-bonder.

# Bibliography


[1] R. P. Feynman. "There's plenty of room at the bottom". In: *Engineering and science* 23.5 (1960), pp. 22–36 (cit. on p. 1).

[2] C. S. Pierce. *Collected Papers*. Vol. 7. 1931 (cit. on p. 1).

[3] D. Loss and D. P. DiVincenzo. "Quantum computation with quantum dots". English. In: *Physical Review A* 57.1 (Jan. 1998), pp. 120–126. DOI: 10.1103/PhysRevA.57.120 (cit. on p. 2).

[4] A. Cottet and T. Kontos. "Spin Quantum Bit with Ferromagnetic Contacts for Circuit QED". English. In: *Physical Review Letters* 105.16 (Oct. 2010), p. 160502. DOI: 10.1103/PhysRevLett.105.160502 (cit. on pp. 2, 19, 55).

[5] A. Blais et al. "Cavity quantum electrodynamics for superconducting electrical circuits: An architecture for quantum computation". English. In: *Physical Review A* 69.6 (June 2004), p. 062320. DOI: 10.1103/PhysRevA.69.062320 (cit. on p. 3).

[6] A. Cottet. "Probing coherent Cooper pair splitting with cavity photons". English. In: *arXiv.org* 12 (June 2014), p. 125139. DOI: 10.1103/PhysRevB.90.125139. arXiv: 1406.4666v3 [cond-mat.mes-hall] (cit. on p. 3).

[7] J.-C. Charlier, X. Blase, and S. Roche. "Electronic and transport properties of nanotubes". English. In: *Reviews of Modern Physics* 79.2 (May 2007), pp. 677–732. DOI: 10.1103/RevModPhys.79.677 (cit. on p. 7).

[8] T. Hartsfield et al. "Single quantum dot controls a plasmonic cavity's scattering and anisotropy." English. In: *Proceedings of the National Academy of Sciences of the United States of America* 112.40 (Oct. 2015), pp. 12288–12292. DOI: 10.1073/pnas.1508642112 (cit. on p. 7).

[9] G.-W. Deng et al. "Charge Number Dependence of the Dephasing Rates of a Graphene Double Quantum Dot in a Circuit QED Architecture". English. In: *Physical Review Letters* 115.12 (Sept. 2015), p. 126804. DOI: 10.1103/PhysRevLett.115.126804 (cit. on p. 11).

[10] R. Ziegler, C. Bruder, and H. Schoeller. "Transport through double quantum dots". English. In: *Phys. Rev. B* 62.3 (July 2000), pp. 1961–1970. DOI: 10.1103/PhysRevB.62.1961 (cit. on pp. 11, 53).

[11] W. G. Van der Wiel et al. "Electron transport through double quantum dots". English. In: *Reviews of Modern Physics* 75.1 (Dec. 2002), pp. 1–22. DOI: 10.1103/RevModPhys.75.1 (cit. on p. 15).

[12] E. A. Laird et al. "Quantum transport in carbon nanotubes". English. In: *Reviews of Modern Physics* 87.3 (July 2015), pp. 703–764. DOI: 10.1103/RevModPhys.87.703 (cit. on p. 16).

[13] J. R. Petta et al. "Coherent Manipulation of Coupled Electron Spins in Semiconductor Quantum Dots". English. In: *Science* 309.5744 (Sept. 2005), pp. 2180–2184. DOI: 10.1126/science.1116955 (cit. on p. 16).

[14] J. Medford et al. "Quantum-Dot-Based Resonant Exchange Qubit". English. In: *Physical Review Letters* 111.5 (July 2013), p. 050501. DOI: 10.1103/PhysRevLett.111.050501 (cit. on p. 18).

[15] J. R. Hauptmann, J. Paaske, and P. E. Lindelof. "Electric-field-controlled spin reversal in a quantum dot with ferromagnetic contacts". In: *Nature Physics* 4.5 (Mar. 2008), pp. 373–376. DOI: 10.1038/nphys931 (cit. on p. 19).

[16] J. Viennot et al. "Coherent coupling of a single spin to microwave cavity photons". English. In: *Science* 349.6246 (July 2015), pp. 408–411. DOI: 10.1126/science.aaa3786 (cit. on pp. 19, 46, 65).

[17] D. F. Walls and G. J. Milburn. *Quantum optics*. Ed. by D. F. Walls and G. J. Milburn. Berlin, Heidelberg: Springer Berlin Heidelberg, 2007. ISBN: 978-3-540-28573-1. DOI: 10.1007/978-3-540-28574-8 (cit. on p. 23).

[18] M. R. Delbecq et al. "Coupling a Quantum Dot, Fermionic Leads, and a Microwave Cavity on a Chip". English. In: *Physical Review Letters* 107.25 (Dec. 2011), p. 256804. DOI: 10.1103/PhysRevLett.107.256804 (cit. on p. 28).

[19] A. A. Clerk et al. "Introduction to quantum noise, measurement, and amplification". English. In: *Reviews of Modern Physics* 82.2 (Apr. 2010), pp. 1155–1208. DOI: 10.1103/RevModPhys.82.1155 (cit. on pp. 28, 35).

[20] A. Cottet, T. Kontos, and B. Douçot. "Electron-photon coupling in Mesoscopic Quantum Electrodynamics". English. In: *arXiv.org* 20 (Jan. 2015), p. 205417. DOI: 10.1103/PhysRevB.91.205417. arXiv: 1501.00803v3 [cond-mat.mes-hall] (cit. on pp. 28, 31).

[21] T. Frey et al. "Dipole Coupling of a Double Quantum Dot to a Microwave Resonator". English. In: *Physical Review Letters* 108.4 (Jan. 2012), p. 046807. DOI: 10.1103/PhysRevLett.108.046807 (cit. on pp. 33, 60).

[22] J. Viennot. "Charge and spin dynamics in a hybrid circuit quantum electrodynamics architecture". English. In: (June 2014) (cit. on pp. 33, 47, 48).

[23] F. Pei et al. "Valley-spin blockade and spin resonance in carbon nanotubes". In: *Nature Nanotechnology* 7.10 (Oct. 2012), pp. 630–634. DOI: 10.1038/nnano.2012.160 (cit. on pp. 43, 44, 60).

[24] J. Viennot, J. Palomo, and T. Kontos. "Stamping single wall nanotubes for circuit quantum electrodynamics". English. In: *Applied Physics Letters* 104.11 (Mar. 2014), p. 113108. DOI: 10.1063/1.4868868 (cit. on pp. 44, 45).

[25] P.-Q. Jin et al. "Strong Coupling of Spin Qubits to a Transmission Line Resonator". English. In: *Physical Review Letters* 108.19 (May 2012), p. 190506. DOI: 10.1103/PhysRevLett.108.190506 (cit. on p. 51).

[26] G. Burkard and A. Imamoglu. "Ultra-long-distance interaction between spin qubits". English. In: *Phys. Rev. B* 74.4 (July 2006), p. 041307. DOI: 10.1103/PhysRevB.74.041307 (cit. on p. 51).

[27] J. Lisenfeld et al. "Observation of directly interacting coherent two-level systems in an amorphous material". In: *Nature Communications* 6 (Feb. 2015), p. 6182. DOI: 10.1038/ncomms7182 (cit. on p. 62).

[28] A. Cottet. "Microwave spectroscopy of a Cooper pair beam splitter". English. In: *Phys. Rev. B* 86.7 (Aug. 2012), p. 075107. DOI: 10.1103/PhysRevB.86.075107 (cit. on p. 66).

[29] J. Viennot et al. "Out-of-equilibrium charge dynamics in a hybrid circuit quantum electrodynamics architecture". English. In: *Phys. Rev. B* 89.16 (Apr. 2014), p. 165404. DOI: 10.1103/PhysRevB.89.165404 (cit. on p. 66).

[30] J. Stehlik et al. "Landau-Zener-Stückelberg interferometry of a single electron charge qubit". English. In: *Phys. Rev. B* 86.12 (Sept. 2012), p. 121303. DOI: 10.1103/PhysRevB.86.121303 (cit. on p. 73).

[31] R. T. Brierley et al. "Adiabatic State Preparation of Interacting Two-Level Systems". English. In: *Physical Review Letters* 109.4 (July 2012), p. 043002. DOI: 10.1103/PhysRevLett.109.043002 (cit. on p. 73).

[32] G. Pemmasani. *Dispy, Distributed and Parallel Computing for Python* (cit. on p. 75).

[33] H. Ribeiro, J. R. Petta, and G. Burkard. "Interplay of charge and spin coherence in Landau-Zener-Stückelberg-Majorana interferometry". English. In: *Phys. Rev. B* 87.23 (June 2013), p. 235318. DOI: 10.1103/PhysRevB.87.235318 (cit. on p. 75).

[34] J. Stehlik et al. "Fast Charge Sensing of a Cavity-Coupled Double Quantum Dot Using a Josephson Parametric Amplifier". English. In: *Physical Review Applied* 4.1 (July 2015), p. 014018. DOI: 10.1103/PhysRevApplied.4.014018 (cit. on p. 78).